5. ESCANABA TROUGH: REFERENCE SITE (SITE 1037)[1]

Shipboard Scientific Party[2]

HOLE 1037A

Position: 40°57.2967′N, 127°30.9093′W

Date occupied: 24 September 1996

Date departed: 25 September 1996

Time on hole: 9 hr, 30 min

Bottom felt (drill pipe measurement from rig floor, m): 3314.0

Distance between rig floor and sea level (m): 11.7

Water depth (drill pipe measurement from sea level, m): 3302.3

Total depth (from rig floor, m): 3323.5

Number of cores (including cores having no recovery): 1

Total core recovered (m): 9.79

Core recovery (%): 103.1

Oldest sediment cored:
Depth (mbsf): 9.5
Nature: clay
Age: Holocene

Comments: Missed mudline.

HOLE 1037B

Position: 40°57.2992′N, 127°30.9004′W

Date occupied: 25 September 1996

Date departed: 2 October 1996

Time on hole: 7 days, 8 hr, 45 min

Bottom felt (drill pipe measurement from rig floor, m): 3311.9

Distance between rig floor and sea level (m): 11.7

Water depth (drill pipe measurement from sea level, m): 3300.2

Total depth (from rig floor, m): 3857.9

Number of cores (including cores having no recovery): 62

Total core recovered (m): 426.95

Core recovery (%): 78.2

Oldest sediment cored:

Depth (mbsf): 533.9
Nature: calcareous claystone
Age: Pleistocene

Hard rock:
Depth (mbsf): 546.0
Nature: basalt

Basement:
Depth (mbsf): 517.4
Nature: basalt

Principal results: At Site 1037, a complete sedimentary sequence of the Escanaba Trough fill sediment was cored between 0 and 495.60 meters below seafloor (mbsf). Beneath this sequence, between 495.60 and 507.8 mbsf, metamorphosed claystone and siltstone was recovered. Basalt was recovered from 507.8 to 546 mbsf. The sedimentary succession is divided into eight lithologic units defined on the basis of sand/silt dominant vs. mud dominant turbidites and changes in composition and sedimentary structure.

Unit I is 3 cm of oxidized mud from the surface, underlain by hemipelagic sediment. Unit II consists of 10 turbidite beds up to 12.5 m thick, some of them containing wood fragments. Some microcrystalline sulfide is associated with the organic matter. Unit III comprises a 50.5-m package of massive sand, where grain-size variation is very subtle. Coring disturbance makes interpretation of the depositional environment uncertain, but it appears that instantaneous deposition caused by the deceleration of a density flow is necessary to account for the lack of grading and the very poor sorting. Unit IV is composed of six mud turbidite beds up to 8 m thick. Unit V is similar to Unit III and comprises 37 m of poorly sorted sand where three fining-upward and some parallel-laminated intervals have been recognized. The top of Unit VI is the first indurated muddy turbidite below the sand of Unit V. The upper 60 m consists of thick, very fine-grained turbidites. Unit VII is homogeneous calcareous silty claystone with rare graded beds. In the lower 60 m, the same type of sediment shows an incipient calcite cementation. No obvious hemipelagic beds are recognized. The turbiditic or hemipelagic nature of this unit remains to be determined. The top of Unit VIII is a 13-m-thick graded turbidite of fine-grained sandstone to claystone that marks the transition to dominant siltstone and minor fine-grained sandstone turbidite beds of various thickness. Carbonate cementation in this unit is moderate. Cores recovered between 495.6 and 507.8 mbsf are silicified calcareous claystone rubble with <20% recovery. These rocks have been thermally altered and occur just above the transition from Escanaba Trough sediment fill to igneous basement. The basalt recovered ranges from nearly aphyric chilled margins with minor hyaloclastite to medium-grained, intersertal to subophitic, highly plagioclase-clinopyroxene-olivine phyric, diabasic textured basalt. Coarser grained basalts began to deteriorate on the description table, and pieces that had been oriented intervals of core up to several centimeters long disaggregated to rubble as the core dried. Some basalts were only slightly altered, but the uppermost flows had veins and vugs filled with fibrous amphibole indicating limited interaction with a hot hydrothermal fluid (>250°C).

Based on foraminifer assemblages, sedimentation rates at this site appear to be exceptionally rapid. The base of the Holocene sequence was tentatively placed at the base of lithologic Unit II at 73.1 mbsf, suggesting a sedimentation rate of 731 cm/k.y. A tentative pick of the 125-k.y. horizon at 317 mbsf suggests a sedimentation rate of 212 cm/k.y. for upper Pleistocene sediments in the Escanaba Trough.

The relatively rapid sedimentation rate in the Escanaba Trough helps to preserve the chemical signatures in pore waters, and diffusive processes are likely to influence signals only over ~35 m. This permits interpretation of the pore-water concentration depth profiles in terms of sedimentary

[1]Fouquet, Y., Zierenberg, R.A., Miller, D.J., et al., 1998. *Proc. ODP, Init. Repts.*, 169: College Station, TX (Ocean Drilling Program).
[2]Shipboard Scientific Party is given in the list preceding the Table of Contents.

provenance and diagenetic features. At 360 mbsf, the concentration profile of several species (Na, K, Ca, Cl, B, H_4SiO_4, NH_4, and Na/Cl ratio) are interpreted as showing a sudden change in the principal source of sediment fill in the Escanaba Trough from the Columbia River above to the Klamath Mountains below. These two areas of sediment provenance have rather different mineral assemblages; sediments from the Columbia River are principally volcanic and are pyroxene rich, whereas sediments from the Klamath Mountains are amphibole rich. Diagenetic reaction in these sediments provide a source of Na, Ca, Li, and B to pore waters and a sink for K, alkalinity, and ammonia. A decrease in Mg and K concentration with depth is interpreted as being caused by clay mineral formation.

The organic matter in the sediments of this reference site is generally immature from the top to ~450 mbsf. There are a few horizons with more mature bitumen that are interpreted to be derived from recycled older sedimentary detritus carried in by turbidites; however, the low extract yields throughout the hole indicate that there are no petroleum zones. Below 450 mbsf, the organic matter is thermally altered, but low concentrations of bitumens reflect in situ maturation without migration/expulsion.

Porosity decreases from 70% near the seafloor to 40% at the base of the sedimentary section and 10% in the basalt and associated altered sediments below 500 mbsf. The Multisensor Track (MST) logs proved particularly useful in identifying and classifying sedimentary units. Fluctuations in magnetic susceptibility correspond to boundaries of turbidites or hemipelagic units identified based on grain-size distributions.

Hole 1037B was logged from 100 to 535 mbsf using the Triple Combo tool, composed of temperature (TLT), resistivity (DIT), density (HLDS), porosity (APS), and natural gamma ray (HNGS) probes and a second run, composed of sonic (SDT), and resistivity (DIT) probes. The gamma ray and resistivity logs correlate well with Pleistocene lithologic sequences identified from recovered core and also show distinctive fining-upward sequences within turbiditic sections. The density, velocity, and porosity logs were affected by irregular borehole conditions as the caliper from the HLDS showed that for the most part, the hole diameter is >16 in. Adara temperatures recorded maximum formation temperatures of 15°C at 85 mbsf that extrapolate to 84 °C at 500 mbsf.

INTRODUCTION

Geological Setting

The only previous drilling in Escanaba Trough was during Deep Sea Drilling Project (DSDP) Leg 5 at Site 35, ~35 km south of the Northern Escanaba Trough Study Area (NESCA; Fig. 9, "Introduction" chapter, this volume), and to the east of the spreading axis. Site 35 was drilled to 390 mbsf without reaching basement, but only 95 m of the interval was cored (Normark et al., 1994).

The turbidite sequence records the sedimentary history of glacial activity and sea-level variations during the Pleistocene. Leg 5 scientists recognized a major change in provenance between the sediments recovered from the lower and upper parts of this hole, defining a change in source from sediments derived from the Klamath Mountains to the Columbia River drainage, respectively (Vallier et al., 1973). A second area of investigation into the sedimentary history of Escanaba Trough involves the controversial "transparent" layer present in all seismic profiles across the trough (Morton and Fox, 1994; Davis and Becker, 1994). This layer occurs at ~100 m depth and is ~50 m thick. Davis and Becker (1994) have interpreted this zone as a homogenous sandy layer related to the Bretz floods that were caused by the catastrophic draining of ice-dammed Lake Missoula at ~13 ka. However, Normark et al. (1994) interpret this zone as a muddy interval formed during an interglacial sea-level highstand. Either interpretation has ramifications for the large-scale hydrology of the Escanaba Trough and can be tested by drilling. The first scenario implies that this unit could be an aquifer for the transport of hydrothermal fluid to sites of cross-stratal permeability, such as faults or volcanic highs. The second scenario suggests that this unit may be an aquiclude that seals the hydrothermal system.

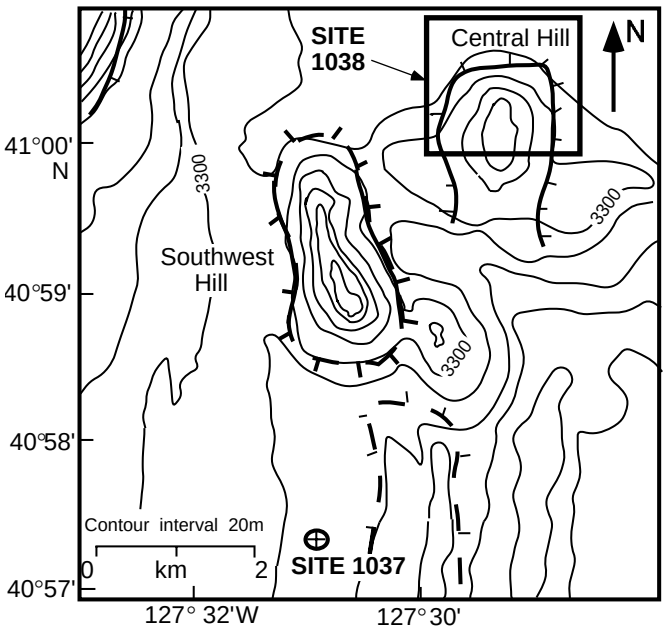

Figure 1. Bathymetric map showing the location of Site 1037 on the flat, turbidite-filled portion of Escanaba Trough and the location of Site 1038 on one of the uplifted sediment hills (Central Hill) that characterizes the volcanic centers in Escanaba Trough. The contour interval is 20 m.

Scientific Objectives

Site 1037 (Fig. 1) was drilled to establish the sedimentary sequence away from the NESCA igneous/hydrothermal center. The Escanaba Trough Reference Site was chosen to provide the necessary background information to evaluate the sedimentary and thermal history in an area away from a hydrothermal upflow zone. Determination of the nature of the igneous basement at a site away from the igneous intrusions that define the volcanic/hydrothermal centers is important to our understanding of the larger scale thermal and hydrologic structure of sediment-covered spreading centers. The reference hole was sited along seismic Line 5 (Fig. 11, "Introduction" chapter, this volume), which shows relatively little disturbance of the sediment and along which a heat flow profile was collected (Davis and Becker, 1994).

OPERATIONS SUMMARY

Operations at the Escanaba Trough Reference Site were planned to recover a section through the sediment package and into basement away from the influence of circulating high temperature hydrothermal fluid. The following is a brief description of coring and recovery information. For more details on operational parameters (drill string configurations, time expended on operations, drilling conditions, etc.), the reader is referred to the Operations Data Appendix on CD-ROM in the back pocket of this volume.

Hole 1037A

Hole 1037A was located with differential Global Positioning System (dGPS) coordinates at 40°57.30′N, 127°30.91′W. The seafloor was estimated at 3314.0 meters below rig floor (mbrf), based on drill string deployed. Advanced piston corer (APC) Core 169-1037A-1H (see Table 1) was taken from 0 to 9.5 m (3323.5 mbrf). The retrieval of a full core liner (9.79 m) with 103.1% recovery suggested that we had missed the mudline, so this hole was abandoned.

Table 1. Coring summary for Site 1037.

Core	Date (1996)	Time (UTC)	Depth (mbsf)	Length cored (m)	Length recovered (m)	Recovery (%)
169-1037A-						
1H	25 Sept.	1520	0.0–9.5	9.5	9.79	103.0
Coring totals:				9.5	9.79	103.0
169-1037B-						
1H	25 Sept.	1600	0.0–6.6	6.6	6.59	99.8
2H	25 Sept.	1640	6.6–16.1	9.5	9.80	103.0
3H	25 Sept.	1745	16.1–25.6	9.5	10.01	105.3
4H	25 Sept.	1820	25.6–35.1	9.5	9.84	103.0
5H	25 Sept.	1930	35.1–44.6	9.5	10.28	108.2
6H	25 Sept.	2020	44.6–54.1	9.5	10.15	106.8
7H	25 Sept.	2145	54.1–63.6	9.5	9.96	105.0
8H	25 Sept.	2335	63.6–73.1	9.5	10.05	105.8
9H	26 Sept.	0030	73.1–82.6	9.5	9.90	104.0
10H	26 Sept.	0135	82.6–92.1	9.5	9.03	95.0
11H	26 Sept.	0240	92.1–101.6	9.5	5.88	61.9
12H	26 Sept.	0340	101.6–111.1	9.5	8.76	92.2
13H	26 Sept.	0435	111.1–120.6	9.5	9.30	97.9
14H	26 Sept.	0514	120.6–130.1	9.5	9.68	102.0
15H	26 Sept.	0705	130.1–139.6	9.5	10.00	105.2
16H	26 Sept.	0800	139.6–149.1	9.5	9.19	96.7
17H	26 Sept.	0840	149.1–158.6	9.5	9.82	103.0
18H	26 Sept.	0945	158.6–168.1	9.5	9.65	101.0
19H	26 Sept.	1045	168.1–177.6	9.5	8.73	91.9
20X	26 Sept.	1230	177.6–182.5	4.9	5.13	104.0
21X	26 Sept.	1330	182.5–192.2	9.7	0.41	4.2
22X	26 Sept.	1430	192.2–201.8	9.6	3.08	32.1
23X	26 Sept.	1535	201.8–211.4	9.6	9.67	101.0
24X	26 Sept.	1700	211.4–221.0	9.6	0.26	2.7
25X	26 Sept.	1955	221.0–230.6	9.6	9.64	100.0
26X	26 Sept.	2130	230.6–240.2	9.6	9.76	101.0
27X	26 Sept.	2315	240.2–249.8	9.6	5.04	52.5
28X	27 Sept.	0055	249.8–259.4	9.6	9.47	98.6
29X	27 Sept.	0230	259.4–269.0	9.6	5.94	61.9
30X	27 Sept.	0625	269.0–278.5	9.5	8.42	88.6
31X	27 Sept.	0805	278.5–288.1	9.6	10.20	106.2
32X	27 Sept.	1000	288.1–297.7	9.6	9.93	103.0
33X	27 Sept.	1215	297.7–307.3	9.6	9.28	96.6
34X	27 Sept.	1400	307.3–316.9	9.6	10.28	107.1
35X	27 Sept.	1610	316.9–326.5	9.6	9.55	99.5
36X	27 Sept.	1750	326.5–336.1	9.6	5.08	52.9
37X	27 Sept.	1950	336.1–345.7	9.6	9.24	96.2
38X	27 Sept.	2210	345.7–355.4	9.7	9.42	97.1
39X	27 Sept.	0020	355.4–365.0	9.6	9.83	102.0
40X	28 Sept.	0210	365.0–374.7	9.7	8.77	90.4
41X	28 Sept.	0400	374.7–384.3	9.6	3.74	38.9
42X	28 Sept.	0620	384.3–393.9	9.6	5.33	55.5
43X	28 Sept.	0825	393.9–403.6	9.7	9.74	100.0
44X	28 Sept.	1000	403.6–413.2	9.6	3.83	39.9
45X	28 Sept.	1210	413.2–422.8	9.6	5.43	56.5
46X	28 Sept.	1430	422.8–432.4	9.6	5.38	56.0
47X	28 Sept.	1700	432.4–442.0	9.6	2.99	31.1
48X	28 Sept.	1945	442.0–451.6	9.6	9.84	102.0
49X	28 Sept.	2230	451.6–461.3	9.7	9.68	99.8
50X	29 Sept.	0125	461.3–470.9	9.6	9.92	103.0
51X	29 Sept.	0425	470.9–480.5	9.6	2.26	23.5
52X	29 Sept.	0940	480.5–490.1	9.6	9.11	94.9
53X	29 Sept.	1155	490.1–495.6	5.5	1.89	34.3
54X	29 Sept.	1445	495.6–499.7	4.1	0.29	7.1
55X	29 Sept.	1700	499.7–501.2	1.5	0.32	21.3
56R	30 Sept.	1635	501.2–507.8	6.6	1.38	20.9
57R	30 Sept.	1700	507.8–517.3	9.5	0.50	5.3
58R	30 Sept.	2110	517.3–526.8	9.5	2.00	21.0
59R	1 Oct.	0025	526.8–529.4	2.6	1.86	71.5
60R	1 Oct.	0425	529.4–533.9	4.5	1.98	44.0
61R	1 Oct.	0905	533.9–538.0	4.1	1.10	26.8
62R	1 Oct.	1500	538.0–546.0	8.0	3.36	42.0
Coring totals:				546.0	426.95	78.2

Note: An expanded version of this coring summary table that includes lengths and depths of sections, location of whole-round samples, and comments on sampling disturbance is included on CD-ROM in the back pocket of this volume.

Hole 1037B

A second attempt to recover the mudline was initiated at Hole 1037B, near the same dGPS location as Hole 1037A (40°57.30′N, 127°30.90′W). The seafloor was estimated at 3311.9 mbrf based on recovery. APC Cores 169-1037B-1H through 19H were taken from 0 to 177.6 m (3489.5 mbrf) with 99.4% recovery. Adara temperature tool measurements were taken on Cores 169-1037B-3H, 5H, 7H, and 9H. Extended core barrel (XCB) coring was started with Core 169-1037B-20X when APC recovery decreased. After XCB Core 169-1037B-55X, the XCB shoe was destroyed and showed evidence consistent with degradation of the drill bit. To continue deepening Hole 1037B with the rotary core barrel (RCB) system, we deployed a free-fall funnel, and made sure it had seated by checking with the Vibration-Isolated Television (VIT) camera. After a pipe trip to pick up the RCB bottom-hole assembly, we reentered Hole 1037B and started coring after washing a few meters of soft fill from the bottom of the hole. RCB Cores 169-1037B-56R through 62R were taken from 501.2 to 546.0 m (3857.9 mbrf) with 27.2% recovery. Overall recovery for Hole 1037B was 78.2% (Table 1). Once we had penetrated more than 40 m into basalt without recovering sediment, and the rate of penetration had slowed enough to compromise operation time at the NESCA massive sulfide deposit, coring operations ended. The hole was conditioned for logging, and we started logging with the Triple Combo tool. Erratic readings suggested that the DIT was not functioning properly, and poor hole conditions, indicated by the caliper, precluded running the Formation MicroScanner (FMS). A second run was made with a DIT/SDT combination, and operations at Hole 1037B ended.

LITHOSTRATIGRAPHY AND SEDIMENTOLOGY

One of the early DSDP legs (Leg 5, Site 35) cored to a depth of nearly 400 m in the sediment fill of the southern part of Escanaba Trough. The site was cored intermittently with only ~25% of the total hole depth sampled. Recovery was notably poor in the interval from 106 to 280 mbsf. In addition, sand recovery was generally poor within the cored sections because of rotary drilling (prepiston core technology), and sections with interbedded sands showed a high degree of coring disturbance. These limitations on the nature of the sediment fill provided by the DSDP cores made it difficult to confidently substantiate the interpretation of the turbidite intervals identified in the seismic reflection profiles (Davis and Becker, 1994). Fewer than half (only 28 of 69) of the recovered cores from Site 35 were described by the shipboard party, in part because of the high gas content. Normark et al. (1994) provided the first complete description and interpretation of this site.

During Leg 169, the only core at Hole 1037A overpenetrated and did not sample the surficial brown oxidized layer. Hole 1037B, therefore, was initiated at the same ship position, the mudline was sampled at 3312 mbrf, and a nearly complete sedimentary sequence (495.60 m) was recovered. Beneath the sedimentary sequence, between 495.60 and 507.8 m, some rubble of metamorphosed claystone, sandstone, and siltstone was recovered (Table 2). The base of the cored interval consists of gray to bluish gray, fine- to medium-grained basalt that was recovered between 507.8 and 546 mbsf (see “Igneous Petrology and Geochemistry” section, this chapter).

Lithologic Units

The sedimentary succession has been subdivided into eight lithologic units that were defined mainly on the basis of sand/silt-dominant vs. mud-dominant turbidites, but also on downhole changes in composition and sedimentary structures (Table 2). Because of poor recovery, the sediments sampled in the transition to basalt were not assigned a unique unit number. The log of magnetic susceptibility shows an almost perfect match with the unit divisions that were made predominantly on the basis of the visual core description (Fig. 2). High values of magnetic susceptibility, with few exceptions, coincide with graded turbidite layers, whereas low values correspond to clayey, likely hemipelagic sediments.

Unit I (Hemipelagic Clay: Holocene)

This unit consists of a 3-m-thick interval of dark yellowish brown (10YR 3/6) oxidized mud underlain by 6 cm of dark gray (N4) clay.

Table 2. Lithologic units recognized in the sedimentary succession, Hole 1037B.

Unit	Age	Lithology	Sedimentary structures
I	Holocene	Clay	None; greenish gray (5G 5/1)
II	Holocene to late Pleistocene	Graded beds of fine-grained sand to silt and clay and interbedded thin hemipelagic mudstone Clay/(silt + sand) = 1–2	Fining upward, poor sorting, faint lamination, basal bed contacts planar locally erosive, rare clay chips, disseminated millimetric blebs of altered organic matter, rare (nearly pristine) wood pieces; Bouma sequence Tab/e, Tb/e
III	late Pleistocene	Massive, fine- to medium-grained dark gray, poorly sorted sands Clay/(silt + sand) = 0	Fining upward absent or locally very poor, very poor sorting, local presence of fine-grained woody material; Bouma sequence Tab/e, Tb/e
IV	late Pleistocene	Graded beds of silt and fine- grained sands to clay and interbedded thin hemipelagic mudstone Clay/(silt + sand) = 4–10	Fining upward, parallel lamination, bedding contacts planar, glauconite(?); Bouma sequence Tb/e
V	late Pleistocene	Graded beds of fine- to medium- grained sands Clay/(silt + sand) = 0	Massive, local fining upward and parallel lamination, poor sorting
VI	late Pleistocene	Graded beds of silt(siltstone) fining upward to clay (claystone) and interbedded thin hemipelagic mudstone Clay/(silt + sand) = 2–10	Fining upward, rare parallel lamination; Bouma sequence Ta/e and Tb/e
VII	late Pleistocene	Silty claystone with very rare thin silty laminae and rare silty to clayey turbidite and hemipelagic mudstone Clay/(silt + sand) >80	Very rare parallel and wavy laminations and very minor fining upward beds
VIII	late Pleistocene	Graded beds of siltstone and fine-grained sandstone to claystone and interbedded thin hemipelagic mudstone Clay/(silt + sand) = 1–5	Fining upward, moderately cemented, parallel, wavy and cross lamination, slightly bioturbated; Bouma sequence Ta/e, Tb/e, rare Tbc/e
	late Pleistocene	Calcareous claystone rubble	None
	late Pleistocene	Calcareous, silicified claystone	None
	late Pleistocene	Noncalcareous silty claystone	Fining upward, parallel laminated, convoluted bedding, bioturbated

Below these surficial layers is a greenish gray (5G 5/1) unconsolidated clay dominated by planktonic foraminifers with radiolarians, diatoms, rare ostracodes, and benthic foraminifers (see "Biostratigraphy" section, this chapter), and containing minor pale green laminae. The lower limit of the unit (interval 169-1037B-1H-2, 18 cm; 1.68 mbsf) is placed at the top of the first turbidite of Unit II, where the clay becomes dark greenish gray (10YR 5/1).

Unit II (Interbedded Fine-Grained Turbidites and Hemipelagic Muds: Holocene to Late Pleistocene)

Unit II consists of 11 turbidite beds (Fig. 2) that can be described in detail, because the recovery in this interval was complete. The bed thicknesses range from 3.0 to 12.5 m. Each bed fines upward from fine- to very fine-grained sand to silt and clay, and Tab/e and Tb/e Bouma sequences are present locally. For example, interval 169-1037B-5H-1, 2 cm, to 169-1037B-5H-5, 5 cm, although incomplete, may be one such sequence. Bed contacts are generally planar, showing probable erosive bases in only two cases (interval 169-1037B-3H-4, 87 cm, and 5H-5, 5 cm). The only observed sedimentary structures are faint laminations localized in the basal or middle part of the turbidites. Lamination is locally highlighted by the presence of disseminated dark gray microcrystalline diagenetic iron sulfides. A rough estimate from the visual descriptions shows that the clay/(sand+silt) ratio of Unit II is between 1 and 2. The presence of thin hemipelagic layers at the top of turbidite beds is suggested by the presence of an abyssal assemblage in the core catcher of Core 169-1037B-5H (see "Biostratigraphy" section, this chapter).

One bed (see core photo in Section 3 [this volume] of interval 169-1037B-4H-6, 24 cm, to 4H-7, 58 cm) is made up of ~2 m of fine- to medium-grained, poorly sorted, ungraded sand that is sharply capped by gray (N5) clay (a hemipelagic interval?). Another contains three pieces of nearly pristine wood (see core photos in Section 3 [this volume] of Section 169-1037B-7H-2, 90 and 125 cm, and 7H-3, 120 cm). Blebs of organic matter (see core photos in Section 3 [this volume] of Section 169-1037B-4H-4, 4 cm) are common throughout the pelitic intervals.

Diagenetic modifications include common fine-grained calcite crystals that are finely disseminated in the sediment. One bed contains sparse blebs (1 to 5 mm in size) of organic matter, sulfide, and calcite crystals (see core photo in Section 3 of Section 169-1037B-6H-1, 44 cm and 132.5 cm). Microcrystalline iron sulfides are normally associated with the organic matter or concentrated in silty laminae.

Unit III (Sand-Rich Turbidites with Minor Hemipelagic Muds: Pleistocene)

Unit III comprises a 50.5-m package of massive, dark gray sands. Observation of possible sedimentary structures was prevented by the high degree of disturbance of the cores (generally soupy). Sands are very fine- to medium-grained and very poorly sorted. Small pieces of woody material are present throughout several of the sand packages. Fining-upward sequences may be present at the top of Core 169-1037B-10H, and in Section 169-1037B-12H-3, but size variation is very subtle and the core is disturbed. Only one bedding contact has been found in this unit (see core photo in Section 3 [this volume] of Section 169-1037B-9H-7, 62 cm). It is a sharp contact between silty clay and an overlying fining-upward turbidite with a fine-grained base. Interpretation of the transport and deposition processes of these sands is highly speculative because of the disturbance of the cores. Instantaneous deposition from a density flow would account for the lack of grading and the very poor sorting. Smear-slide observations indicate that sands of this interval are feldspatholithic to volcanolithic (lithic arkose to litharenite) and may be correlative with the sands found in samples from DSDP Site 35 recovered at the same depth and thought to be sourced from the Columbia River (Vallier, 1970; Vallier et al., 1973; Zuffa et al., in press)

Unit IV (Fine-Grained Sand to Mud Turbidites: Pleistocene)

This unit is composed of six mud turbidite beds (two of them have a thickness of >8 m) that have basal decimeter-scale intervals of finely laminated, dark gray fine sand and silt that fine upward to silty clay and clay. This unit shows a very distinct pattern on the magnetic susceptibility log (Fig. 2). Small blebs of black (2.5 YR) soft, acid-volatile iron sulfide are disseminated throughout the clayey intervals (e.g., Section 169-1037B-14H-2) and locally accentuate laminations

Table 2 (continued).

Unit	Age	Diagenetic features	Occurrence	Interval (mbsf)
I	Holocene	None	169-1037B-1H-1, 0 cm, to 169-1037B-1H-2, 18 cm	0–1.68
II	Holocene to late Pleistocene	Disseminated very fine-grained sulfides locally concentrated in thin bands corresponding to silty laminae	169-1037B-1H-2, 18 cm, to 169-1037B-8H-CC, 33 cm	1.68–73.10
III	late Pleistocene	None	169-1037B-9H-1, 0 cm, to 169-1037B-13H-CC, 15 cm	73.10–120.60
IV	late Pleistocene	Very fine-grained sulfides, disseminated or in black mottled laminations	Sections 169-1037B, 14H-1, 0 cm, to 169-1037B-16H-3, 25 cm	120.60–142.85
V	late Pleistocene	None	Sections 169-1037B-16H-3, 25 cm, to 169-1037B-19H-CC, 14 cm	142.85–177.60
VI	late Pleistocene	Upper part: very slightly indurated Lower part: incipient calcite cementation, some calcite concretions	Sections 169-1037B-20X-1, 0 cm, to 169-1037B-32X-5, 133 cm	177.60–297.70
VII	late Pleistocene	Incipient calcite cementation, widespread centimetric calcite concretions, very fine-grained Fe-monosulfides: disseminated or in blebs, high lithium content	Sections 169-1037B-32X-6, 0 cm, to 169-1037B-40X-2, 8 cm	297.70–366.58
VIII	late Pleistocene	Moderate calcite cementation, carbonate concretions, high strontium and calcium content, high lithium content in the lower part of the unit	Sections 169-1037B-40X-2, 0 cm, to 169-1037B-53X-2, 38 cm	366.58–495.60
	late Pleistocene	Well indurated, partly silicified	Section 169-1037B-54X-1, 0 cm, to 169-1037B-54X-1, 29 cm	495.60–499.70
	late Pleistocene	Well indurated, partly silicified	Section 169-1037B-55X-1, pieces	499.70–501.20
	late Pleistocene	Small (submillimetric) white blebs of quartz	Section 169-1037B-56R-1, 0 cm, to 169-1037B-56R-2, 138 cm	501.20–507.80

near the tops of the turbidite sequences (Fig. 3). The tops of these beds show distinct intervals of clay (hemipelagite beds) that lie above millimeter-scale grayish green (5G 4/2) or pale green (5G 6/2) laminae possibly containing glauconitic minerals.

Unit V (Sand-Rich Turbidites with Minor Hemipelagic Muds: Pleistocene)

This unit is lithologically similar to Unit III. It comprises ~37 m of massive dark gray, very fine- to medium-grained and very poorly sorted sands. The cores of this interval are relatively disturbed and locally soupy but, although these sands have about the same lithology as those described in Unit III, three fining-upward sequences and several parallel-laminated intervals (see core photo in Section 3 [this volume] of interval 169-1037B-16H-3, 33–82 cm) have been recognized by visual description. The tops of the fining-upward sequences (see core photo in Section 3 [this volume] of interval 169-1037B-16H, 24 cm, to 16H-CC, 20 cm) are characterized by sharp contacts with the massive, fine-grained sand bases of the overlying turbidites and by thin, light colored, silty clay, hemipelagic intervals (see core photo in Section 3 [this volume] of interval 169-1037B-16H-3, 24–26 cm) overlying parallel laminated silt and silty clay (Fig. 3).

Unit VI (Silt to Clay Turbidites and Hemipelagites with Minor Carbonate Alteration: Pleistocene)

The top of Unit VI is defined as the first slightly indurated, muddy turbidite below the sands of Unit V. The unit extends downhole for ~120 m. The upper 60 m, characterized by relatively poor sporadic recovery, is slightly disturbed and generally consists of thick, very fine-grained turbidite beds fining upward from silt to clay with Ta/e and Tb/e Bouma sequences. This lithologic pattern continues in the lower 60 m, but silt and clay show an incipient calcite cementation that is probably the cause of the higher disturbance of this cored interval. Cementation processes are locally represented by white, calcite-rich patches in the silty clay (e.g., interval 169-1037B-22X-1, 63–103 cm). The interval 169-1037B-22X-2, 60–135 cm, is very rich in organic matter and shows reverse grading with the coarsest particles (up to 3 mm) at the top of the bed. The average clay/(silt+sand) ratio of this unit lies between 10 and 20. The presence of thin hemipelagic layers is indicated by a subtle change in the color of the silty clay (e.g., interval 169-1037B-22X-2, 55–60 cm), and has been confirmed by paleontological analyses. The sedimentation rate in this interval seems to be high and may be a result of huge muddy turbiditic resedimentation processes.

Unit VII (Calcareous Silty Claystone with Minor Silty Turbidites: Late Pleistocene)

Rocks in this unit are dark, moderately indurated, calcareous silty claystones that are strongly disturbed by drilling (all cores are "biscuited"). Irregularly shaped carbonate nodules, 1–5 cm in diameter, are present locally (see core photo in Section 3 [this volume] of intervals 169-1037B-37X-4, 5–20 cm, and 37X-5, 123–125 cm) as are round blebs (1–10 mm) of acid volatile iron monosulfide. Authigenic dolomite is present in a laminae in interval 169-1037B-34X-8, 29–30 cm, and may be present elsewhere. A nearly pure thin bed of calcimicrite was found in interval 169-1037B-33X-3, 21–23 cm. Graded beds are less common than in the overlying unit; some graded beds may be undetectable by visual inspection because of the fine grain size. Some thin (1 to 10 mm), black bands of iron sulfide seem to be concentrated in clayey siltstone laminae (see core photo in Section 3 [this volume] of intervals 169-1037B-37X-4, 0–20 cm, and 37X-5, 65–85 cm) and could represent the base of resedimented beds. However, the dominantly homogeneous silty claystone lithology of this unit and the strong core disturbance prevent identification of other possible sedimentary structures; consequently, the prevalent turbiditic or hemipelagic nature of this unit remains to be determined, and there are no data with which to infer the time span recorded by this interval of the sedimentary succession. This unit is coincident with an interval of low magnetic susceptibility (Fig. 2) that distinguishes it from Units VI and VIII. Localized spikes in the magnetic susceptibility profile are likely related to the presence of the blackish bands of Fe monosulfide (greigite?) that is disseminated throughout the fine-grained intervals and occurs locally in silt laminae (See "Physical Properties" section, this chapter).

Unit VII is also characterized by a distinct peak in the pore-water lithium content that increases from ~100 µM at the base of the unit to 375 µM in the middle and decreases to 50 µM at the transition to the underlying Unit VIII. This implies the presence (or dissolution) of a

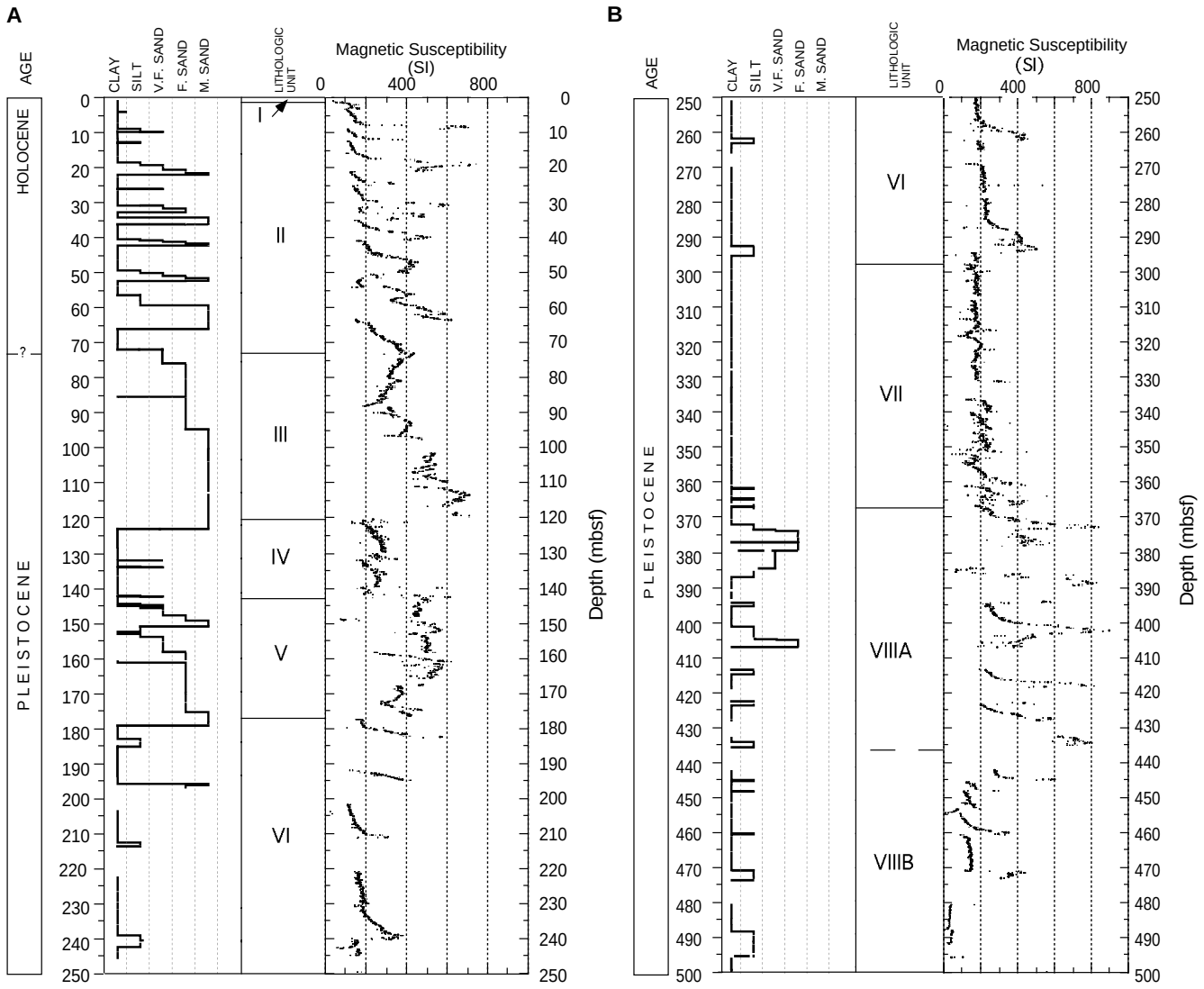

Figure 2. (**A**) Summary lithologic column and (**B**) profile of MST measurements of magnetic susceptibility for the sedimentary succession recovered in Hole 1037B.

lithium-bearing phase (possibly lepidolite) within the sediment of this sequence (see "Inorganic Geochemistry" section, this chapter).

Unit VIII (Calcareous Fine-Grained Sand to Silt Turbidites: Pleistocene)

The top of Unit VIII is a thick (at least 7 m) graded turbidite bed of fine sandstone to silty claystone (clay/[silt+sand]~1). This bed underlies the more homogenous pelitic deposits of Unit VII and marks the transition to sediments that are dominated by dark gray (N4) to dark greenish gray (5GY4/1) siltstone and minor fine-grained sandstone turbiditic beds of various thickness with Tb/e, Ta/e, and rare Tbc/e Bouma sequences. The clay/(silt+sand) ratio in this unit varies from 1 to 5. Core recovery was not complete, and the drilling disturbance of this moderately indurated unit is strong (see core photos in Section 3 [this volume] of Cores 169-1037B-48X through 52X). Unit VIII shows more parallel and wavy lamination than the overlying units. Rare cross-lamination and bioturbation is also present. Carbonate cementation is moderate, and 1- to 5-cm diagenetic concretions are widespread from the top of the unit through Section 169-1037-47X-CC. $CaCO_3$ content averages ~6%.

Preliminary smear-slide observations made aboard ship indicate that sands of this interval are quartzofeldspathic (arkosic) and may be correlative with the Escanaba sands thought to be derived from the Klamath River found in a few samples from DSDP Site 35 recovered at 375 and 385 mbsf (Zuffa et al., in press). Strontium and calcium contents in pore waters are elevated with respect to other units and, surprisingly, mark the independently defined lithostratigraphic boundaries of this unit (see "Inorganic Geochemistry" section, this chapter).

Using the distribution of the lithium content of pore fluids, the magnetic susceptibility, and the natural gamma-ray log (see "Physical Properties" section, this chapter), this unit can be further subdivided into Subunits VIIIA and VIIIB. This subdivision, although not as significant a change in sedimentary characteristics as the former unit divisions, is, however, compatible with the lithologic and sedimentary stratigraphic column (Fig. 2).

Transition from Sediment to Basalt

Cores 169-1037B-54X, 55X, 56R, and 57R extend the sedimentary succession to the depth of 507.8 m, but recovery was very poor

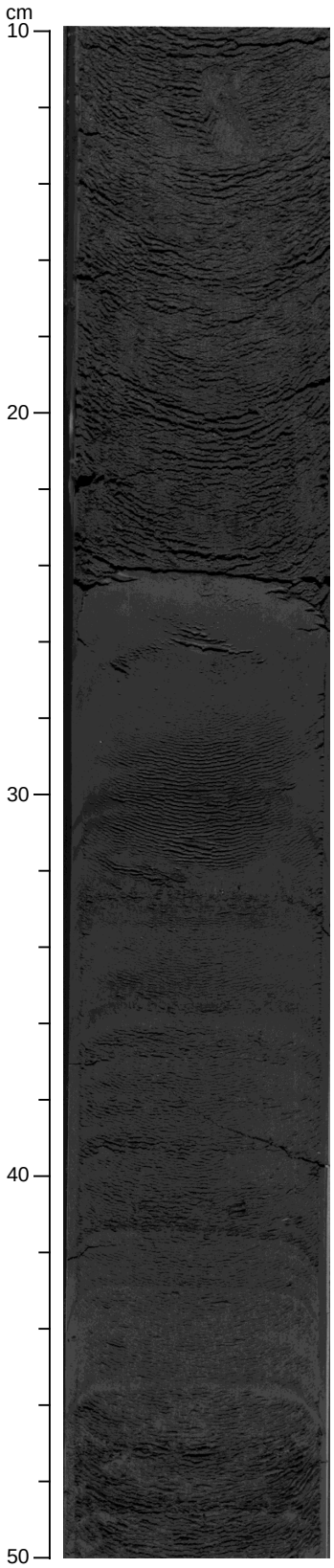

Figure 3. The base and top of turbidites in Unit V. Note the lighter colored silty clay below the sharp contact, the parallel silt and silty clay laminations in the top of the lower turbidites, and the massive base of the upper turbidite. The light-colored silty clay interval at 25 cm is interpreted as a hemipelagite (interval 169-1037B-16H-3, 10–50 cm.)

in those units (Table 2). Section 169-1037B-54X-1 only recovered 29 cm of well-indurated, partly silicified calcareous claystone rubble. Section 169-1037B-55X-1 only recovered some pieces of calcareous silicified claystone. Recovery in interval 169-1037B-56R-1, 0 cm, to 1037B-56R-2, 138 cm, was much better. The interval consists of non-calcareous silty claystone very rich in sedimentary structures such as fining-upward intervals, parallel and cross-lamination, convolute lamination, and bioturbation. Core 169-1037B-57R recovered several pieces of brown (10YR 5/3) silicified, parallel-laminated siltstone and sandstone just above the first igneous rock recovered (see "Igneous Petrology and Geochemistry" section, this chapter). The brown color in the siltstone and sandstone is imparted by recrystallized, euhedral brown biotite. Euhedral plagioclase feldspar in the sandstone is also suggestive of authigenic overgrowth or hydrothermal recrystallization of detrital plagioclase.

BIOSTRATIGRAPHY

Site 1037 is composed almost entirely of mud or fine sand turbidites and so presents special problems for biostratigraphy. Hemipelagic sediments with abundant planktonic foraminifers and abyssal benthic foraminifers at Hole 1037B occur only in lithologic Unit I, a hemipelagite in the top 1.68 m from the hole (see Table 3 on the back-pocket foldout, this volume; Sample 169-1037B-1H-2, 6–8 cm; 1.57 mbsf), and beneath the bases of selected turbidites, which, in shipboard study, were discovered in five samples: 169-1037B-3H-4, 90–92 cm (21.51 mbsf); 5H-5, 6–8 cm (41.17 mbsf); 16H-1, 54–56 cm (140.15 mbsf); 34X-CC (336.09 mbsf); and 48X-5, 22–24 cm (448.23 mbsf). Additional possible hemipelagites have been identified for shore-based study. Several other samples from sandy turbiditic sediments contain well-preserved and common planktonic foraminifers, but most turbidite samples are barren or contain <10 specimens in 20 cm^3 of bulk sediment (Table 3). The samples from sandy turbidites generally contain a mixed assemblage of neritic, bathyal, and abyssal benthic foraminifers, and the samples from homogeneous mud intervals of turbidites generally contain thin-walled, neritic benthic foraminifers often with a trace of shallow-water diatoms such as *Isthmia* and *Arachnoidiscus.*

Heating at the bottom of the sequence caused some interesting alterations of the foraminifer assemblage. Pine pollen changed from pale yellow to pale orange at ~326 mbsf (Section 169-1037B-35X-CC), and the color deepens with increasing depth in the hole. Foraminifers also change from white to a golden brown beginning at ~375 mbsf (Section 169-1037B-40X-CC). An assemblage of discolored foraminifers that also have been flattened in shape is found at ~450 mbsf (Sample 169-1037B-48X-5, 22–24 cm).

Coiling direction zones CD1 to CD4 (see "Explanatory Notes" chapter, this volume, for definitions of these informal zones) are tentatively recognized in the Holocene to late Pleistocene sequence. A planktonic foraminifer assemblage characteristic of the subarctic transitional watermass is found in three hemipelagites (Samples 169-1037B-1H-2, 6–8 cm; 3H-4, 90–92 cm; and 5H-5, 6–8 cm) in the upper 41 mbsf. The samples are assigned to the Holocene coiling direction zone CD1 (Fig. 4). The next deepest samples with common planktonic foraminifers come from the turbiditic sands of lithologic Unit III. These contain a trace of dextral *Neogloboquadrina pachyderma,* and may belong either to the base of the Holocene or the latest Pleistocene, perhaps the termination of the last glacial maximum. Tentatively, the base of the Holocene is placed above the turbiditic samples at the base of lithologic Unit II at 73.1 mbsf, pending further study.

Subarctic assemblages of planktonic foraminifers are found in both hemipelagic and turbiditic samples throughout lithologic Units III through VI (Table 3; Fig. 4), and the interval is tentatively assigned to the latest Pleistocene coiling direction zone CD2, which we

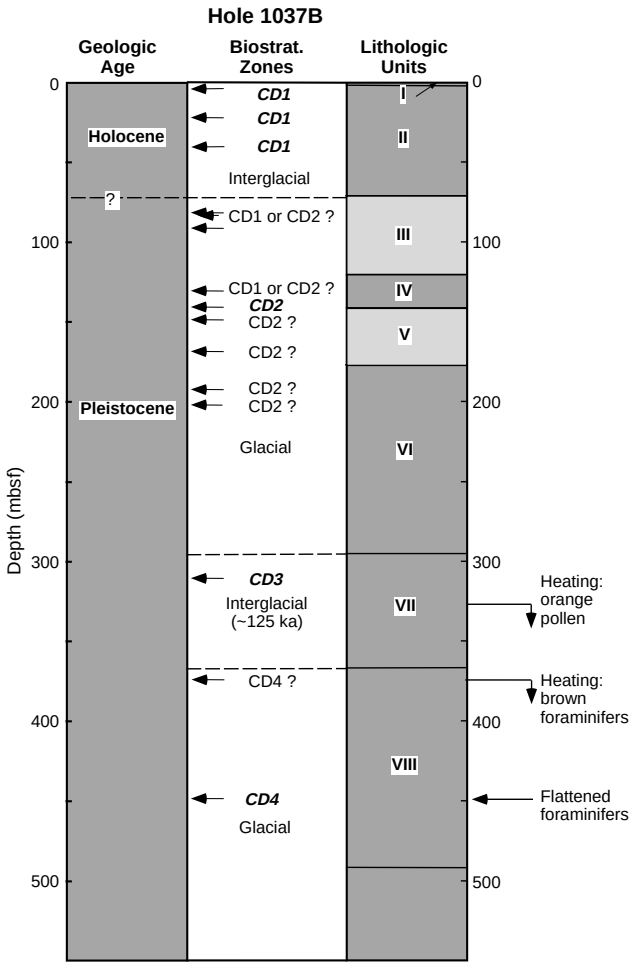

Figure 4. Zonal assignments of foraminifer-bearing samples. The samples marked in bold italics are considered most reliable because they are from hemipelagites and contain abyssal, in situ assemblages of benthic foraminifers.

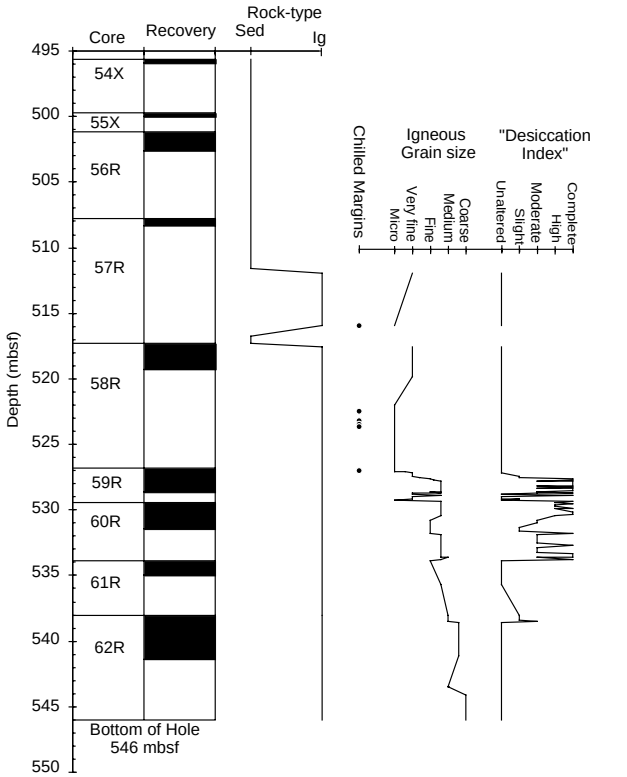

Figure 5. Summary diagram showing the location, recovery, and grain size of igneous rocks recovered from the Escanaba Trough Reference Site, Hole 1037B. The downhole log of the "Desiccation Index" shows the occurrence and qualitative estimate of the severity of exfoliative desiccation in these cores.

hypothesize corresponds to oxygen isotope Stages 2 through 5d. One transitional assemblage is found in a hemipelagite in lithologic Unit VII and is tentatively assigned to coiling direction zone CD3, which we hypothesize corresponds to oxygen isotope Stage 5e (~125 ka). Two samples with abundant subarctic planktonic foraminifers were found in lithologic Unit VIII, and the interval is tentatively assigned to coiling direction zone CD4, which we hypothesize corresponds to oxygen isotope Stage 6. The correspondence to oxygen isotope stages will be verified by isotopic study of sequences from Middle Valley and sites drilled during Leg 167.

Sedimentation at Site 1037 is exceptionally fast. If the base of the Holocene (~10 ka) is placed at the base of lithologic Unit II at 73.1 mbsf, and if the 125 ka. horizon is placed at 316.89 mbsf at Section 169-1037B-34X-CC, then the sedimentation rates are 731 cm/k.y. in the Holocene interval and 212 cm/k.y. between the base of the Holocene and the 125-ka horizon.

The tentative biostratigraphic assignments will be tested using radiometric dating in addition to further biostratigraphic analysis of other hemipelagic intervals recognized in the sequence. ^{14}C analysis is possible on the foraminifer carbonate of selected samples and on wood pieces found in several sandy turbidites. Other material may be suitable for dating. Interestingly, refractory organic debris from vascular plants is the most common constituent in the sand-sized fraction of many mud turbidites, and biotite is also abundant.

IGNEOUS PETROLOGY AND GEOCHEMISTRY

The occurrence and nature of igneous rocks recovered from the Escanaba Trough Reference Site are summarized in Figure 5. The first igneous rocks were encountered in Core 169-1037B-57R (~508 mbsf). Two pieces (~24 cm) of slightly altered, microcrystalline to fine-grained, plagioclase-clinopyroxene-phyric basalt were recovered in the lower portion this core (interval 169-1037B-57R-1, 32–57 cm). Upper and lower finer grained, darker chilled margins are present, whereas the interior is coarser with abundant, acicular white plagioclase phenocrysts and black crystals of clinopyroxene, both ~1 mm in size. The basalt is moderately vesicular (≈5%), with subrounded amygdules partly filled with zeolites or/and clay minerals and rare grains of euhedral pyrite. Immediately overlying and underlying these pieces are small unoriented pieces of sedimentary rock. The sedimentary rocks (intervals 169-1037B-57R-1, 0–31 cm, and 57–62 cm; 507.80–508.11 and 508.37–508.42 mbsf) comprise well-indurated pieces of siltstone and sandstone. These sedimentary rocks have a characteristic brown color (10YR-5/3) resulting from a high content of biotite and iron-oxides/hydroxides. The biotite is partly euhedral, feldspar shows growth zonation, and quartz is highly recrystallized. The upper 6 cm of interval 169-1037B-58R-1, 0–6 cm (517.30–517.36 mbsf), consists of pale greenish sandstone with euhedral epidote, biotite, and needles of amphibole, in addition to recrystallized quartz and feldspar.

Only igneous rocks were recovered from interval 169-1037B-58R-1, 6 cm (517.36 mbsf), to the bottom of the hole at 546 mbsf, indicating that the basaltic basement in this region has probably been sampled. Recovery in the igneous section averages ~28%, very similar to other penetrations of the upper oceanic crust in the eastern Pa-

Table 4. X-ray diffraction mineral identifications from the Escanaba Trough Reference Site, Hole 1037B.

Core, section, interval (cm)	Description	XRD mineral identifications
169-1037B-		
36X-1, 140–150	PW sample - clays	Quartz, plagioclase, chlorite > smectite mixed layer clay, mica, calcite
58R-1, 46–49	Clay on fracture in basalt	Mg-saponite >> chlorite mixed layer clay
58R-2, 79–82	Fibrous actinolite (?)	Mg-hornblende, actinolite
59R-1, 130	Highly altered, desiccated basalt	Plagioclase, augite + Mg-smectite > chlorite mixed layer clay
60R-1, 96–99	Clay, chlorite, prehnite (?) in vesicles	Calcite, Mg-smectite >> chlorite mixed layer clay, (plagioclase, augite)
62R-2, 58–78	White zeolite in vertical vein	Albite, calcite, Mg-smectite

Note: PW = pore water.

cific Ocean (e.g., Holes 504B, 896A; Alt, et al., 1996), though a number of spectacular, unbroken pieces of continuous drillcore, some greater than a meter in length, were recovered. The rocks comprise microcrystalline to medium- to coarse-grained, sparsely to moderately plagioclase ± clinopyroxene-phyric basalts. There is a general increase from microcrystalline to very fine-grained rocks at the top of the igneous section to medium- to coarse-grained rocks toward the bottom of the core. Vertical and subhorizontal chilled contacts, commonly with associated brecciation, are present in Sections 169-1037B-57R-1 and 58R-2. Medium- and coarse-grained basalts have well-developed subophitic to diabasic textures, but are not completely holocrystalline, and a minor interstitial mesostasis is present.

Macroscopic and textural evidence suggest that the main body of the igneous material recovered in Hole 1037B is a single, thick massive flow that erupted on to the ocean floor representing the upper part of the igneous basement. However, insufficient penetration into igneous material and the absence of intersection with an underlying igneous unit preclude any confirmation of whether the igneous basement was reached. The two pieces of basalt in Core 169-1037B-57R may be a thin sill intruded at a shallow level into sediments, although these pieces are separated from the lower igneous flow by only two small, nonoriented pieces of altered sediment. Minor bit-heave or partial collapse of the borehole wall during drilling may have resulted in a false juxtaposition of these pieces.

In hand specimen, the basalts appear relatively unaltered, with primary plagioclase phenocrysts in many pieces. Clinopyroxene phenocrysts are variably altered and partly pseudomorphically replaced by hydrothermal minerals (e.g., stilpnomelane(?)/biotite(?) ± chlorite and/or amphibole). The mesostasis commonly appears greenish gray to greenish, most probably reflecting the replacement of interstitial glass by chlorite and/or clay minerals. Faint brownish red discolorations are present in Cores 169-1037B-58R and 59R, indicating a slight oxidative alteration of the groundmass. The basalts are slightly to moderately vesicular (1%–10%), with subrounded vesicles filled with clay minerals (Mg-smectite), chlorite, and calcite (Table 4). Large elongate vugs and vesicles, commonly connected by thin veins, are present in microcrystalline basalt in Cores 169-1037B-58R and 59R. The veins are partially to completely filled with fine, interwoven whiskery needles of Mg-hornblende up to 2 mm long (optical and X-ray diffraction [XRD] confirmation; Table 4). The occurrence of Mg-hornblende is unusual in basalts from the upper ocean crust and requires precipitation from a high temperature hydrothermal fluid (>350°C). The basalts surrounding these vesicles and vugs do not appear more highly altered in hand specimen.

Veins filled with a variety of mineral assemblages are sparsely present throughout the igneous section. The most common vein-filling minerals are chlorite, Mg-smectite (mixed-layer clays), calcite, actinolite/Mg-hornblende, and albite. Veins are generally thin (<1 mm), although they can be up to 6 mm wide. A 2- to 3-mm-wide subvertical vein of white radiating aggregates of albite intergrown with calcite and Mg-smectite/chlorite (Table 4) bisects the core in Sections 169-1037B-62R-1 and 62R-2.

An unusual alteration phenomena was observed within the basement in Cores 169-1037B-59R and 60R (~526.8–533.9 mbsf) and weakly present at the top of Section 169-1037B-62R-1 (see Fig. 5). There was a high rate of recovery of coherent pieces of basalt from these intervals (~54%), but after splitting and drying on the description tables, these rocks rapidly disintegrated into flakes along preexisting fractures, around the outer curve of the core, and parallel to the cut surface. Within 1 hr, most pieces from this interval had degraded to unconsolidated flakes (Fig. 6). The appearance of these samples is strongly reminiscent of spherically exfoliated gabbros common in tropical climates (e.g., weathered gabbros of the Troodos ophiolite). The term "exfoliative desiccation" was coined to describe the occurrences of this alteration process on the hard rock visual core descriptions. The occurrence and a qualitative estimate of the severity of exfoliative desiccation is shown in a separate column in Figure 5. Fine- to medium-grained basalts are more susceptible to this style of alteration than finer grained pieces of basalt. XRD and smear-slide investigations confirm the presence of abundant Mg-smectite/chlorite mixed layer clay and albite within the exfoliated flakes, suggesting that these basalts were altered by moderately hot (≈150°–200°C) hydrothermal fluids. Numerous, subvertical thin (<0.5 mm) fractures lined with chlorite, commonly in conjugate sets, are present throughout this altered interval. Vein margins display a resinous or polished luster when split, but slickensides or other indicators of shearing or displacement are absent (see "Structural Geology" section, this chapter). Although evidence for a discrete fault or fault zone is not present within these sections, the numerous, chlorite-lined fractures may have provided channels for the through-flow of hydrothermal fluids that caused extensive alteration of the surrounding wall rock.

Textures and the extent of alteration are more easily assessed in thin section. Grain size of the basalts ranges from microcrystalline to coarse-grained, with a general increase with depth. The basalts are sparsely to moderately plagioclase ± olivine-phyric, although many rocks have seriate textures or are nearly holocrystalline. Plagioclase, as both phenocrysts and within the groundmass, is generally unaltered except for the minor development of brown clays along fractures and crystal rims. Fresh phenocrysts of olivine are present in many samples, although all grains are partially altered. Olivine is generally altered to talc, with rims of secondary magnetite. Other secondary minerals after olivine include amphibole, clay minerals, minor calcite, and possibly amorphous silica(?). An unusual, strongly colored micaceous mineral, associated with talc and magnetite, replaces the cores of completely altered, prismatic olivine phenocrysts in some samples, especially in Cores 169-1037B-57R through 60R. This mineral is strongly pleochroic (green to yellow-brown), uniaxial negative, with second to third order birefringence, has two orthogonal cleavages, and is tentatively identified as stilpnomelane. Rocks in these cores commonly have acicular actinolitic-hornblende replacing clinopyroxene and mesostasis, as well as filling voids and crosscutting veins. The presence of a high-temperature, K-bearing phase such as stilpnomelane is unusual in ocean floor basalts as K is normally quantitatively removed from the rock by fluid-rock interaction at el-

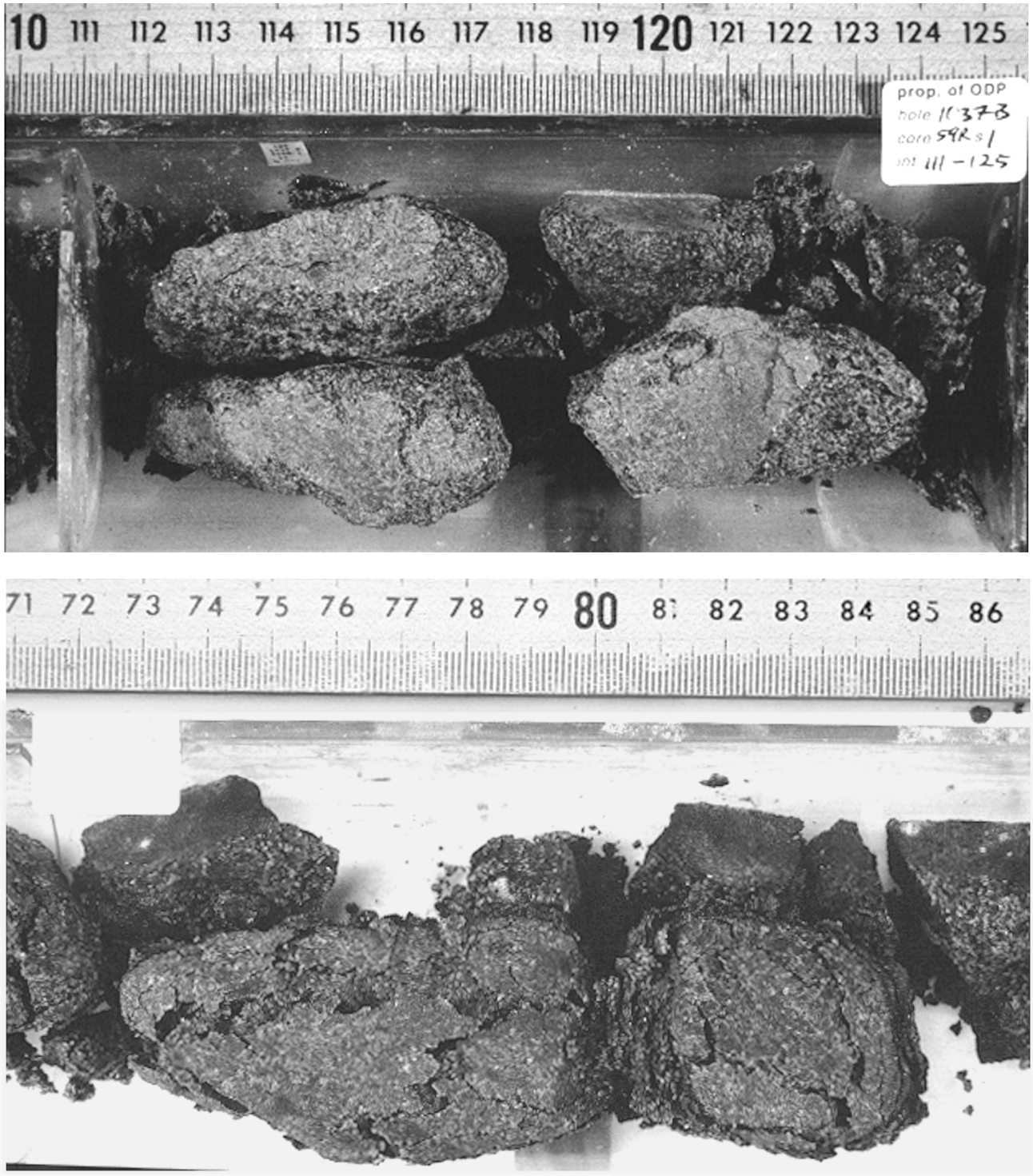

Figure 6. Basalts from Hole 1037B showing different intensities of exfoliative desiccation.

evated temperatures (>200°C; e.g., Alt et al., 1996). This indicates that a later hydrothermal event has overprinted low-temperature seafloor processes that previously enriched K in these basalts.

Clinopyroxene is partly to completely altered to amphiboles and clay minerals. Magnetite is not pervasively altered, and secondary titanite was not observed. The mesostasis in all slides is completely altered to clay minerals (± chlorite mixed-layers?) and actinolitic hornblende.

A strong increase in groundmass grain size is shown in Figure 5 (see also Fig. 7A–7D). Basalts in Sections 169-1037B-61R-1 through 62R-2 are medium grained, with well-developed (sub-) ophitic to diabasic textures. The deepest basalts recovered (Section 169-1037B-62R-3) however, are significantly coarser grained, nearly holocrystalline, and microgabbroic in texture. Clinopyroxene forms the structural framework in these rocks, with plagioclase as isolated crystals within larger augite grains.

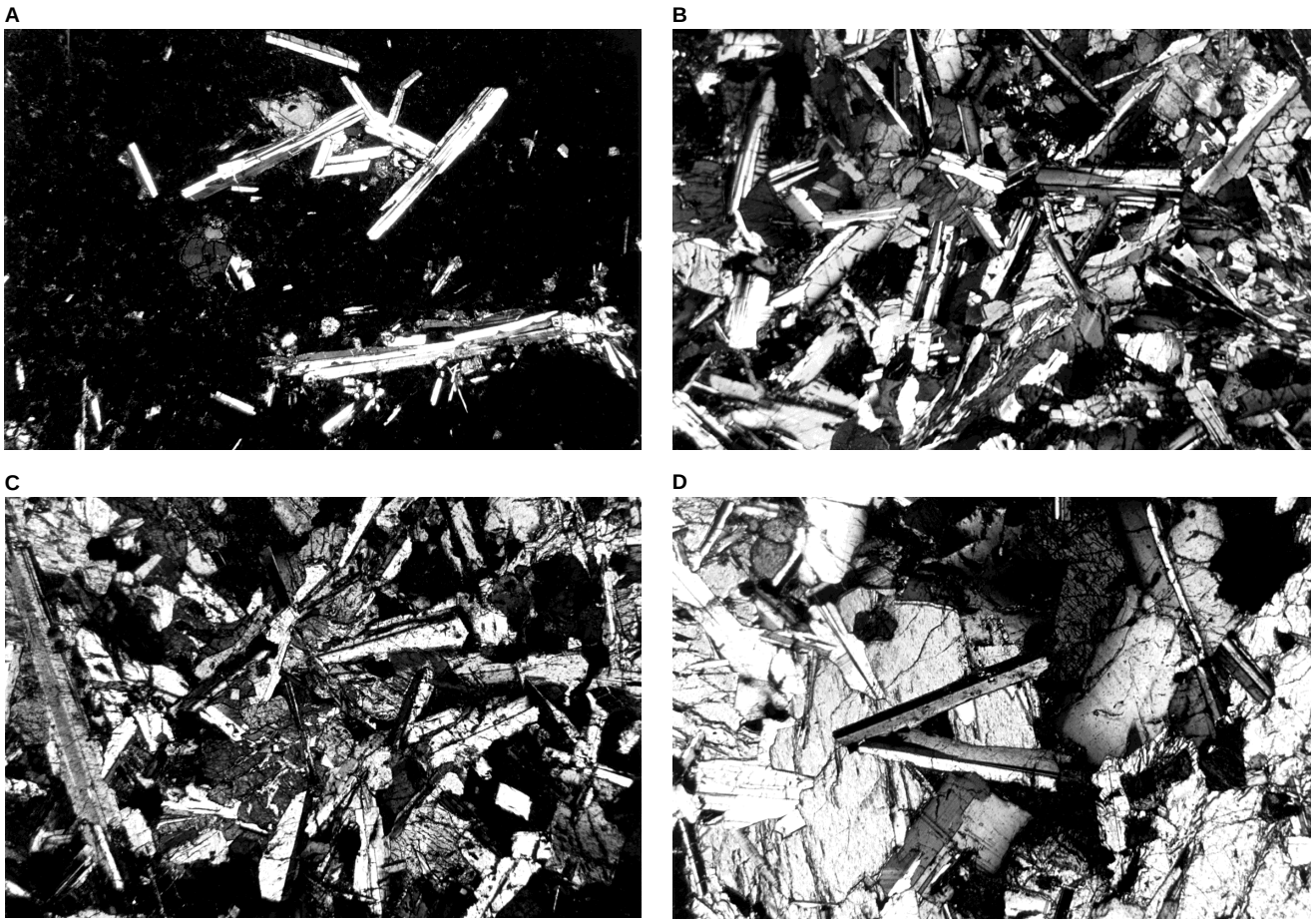

Figure 7. Four photomicrographs showing the dramatic increase in grain size, and change in texture downhole within the basalts recovered in Hole 1037B; field of view in all = 4.6 mm. **A.** Sample 169-1037B-61R-1, 65–70 cm, shows fresh glomerocrystic plagioclase and olivine in microcrystalline groundmass (2.5×, crossed polars). **B.** Sample 169-1037B-61R-1, 104–112 cm, shows fine-grained basalts, intersertal to subophitic textures (2.5×, crossed polars). **C.** Sample 169-1037B-62R-1, 126–129 cm, shows ophitic clinopyroxene in medium-grained diabasic basalt (2.5×, crossed polars). **D.** Sample 169-1037B-62R-3, 82–86 cm, shows coarse-grained clinopyroxene with isolated laths of coarse-grained plagioclase in a nearly holocrystalline microgabbroic basalt.

Geochemistry of Basalts from the Escanaba Trough Reference Site

Seven basalts from Hole 1037B were selected for geochemical analysis by X-ray fluorescence. Total sulfur contents were determined on splits of these samples using the shipboard carbon-nitrogen-sulfur analyzer. The samples selected are rocks that appeared to be the least altered in hand specimen. No samples of highly desiccated basalt were analyzed. These analyses are complemented by a single analysis of basalt from Hole 1038G, located at Central Hill, ~5 km to the north of Site 1037 (see Fig. 1). Major element oxide contents and trace element concentrations are tabulated in Table 5.

Recent studies of fresh basaltic glasses collected by dredging and submersible dives provide a reference set for comparison with these new analyses (Davis and Clague, 1987; Davis et al., 1994). The glass samples from the Escanaba Trough range from relatively primitive to moderately fractionated, with the expected increases in incompatible elements with fractionation (Davis et al., 1994). The large scatter in glass data, mineral compositions, and textural evidence suggests that variations in the compositions of Escanaba magmas are the result of complex petrogenetic processes involving magma mixing, heterogeneous source compositions, and different degrees of partial melting (Davis et al., 1994).

The basalts recovered during Leg 169 from the Escanaba Trough have low loss on ignition (LOI; <1.20 wt%) and generally have major element oxide and trace element concentrations within the ranges of ocean basalts. There are no regular trends of elemental concentrations with depth. Potassium and rubidium contents are elevated compared to mid-ocean-ridge basalt (MORB; up to 0.87 wt% and 31 ppm, respectively), indicating that some alkali enrichment has occurred, most probably caused by the formation of low temperature, K- and Rb-rich phases such as celadonitic clays or mixed layer smectites.

Davis et al. (1994) note the presence of fresh basaltic glasses with high K_2O contents indicative of E-MORB. The relative abundance of Nb, Zr, and Y in the Leg 169 samples are compared in Figure 8. These trace elements are commonly immobile during hydrothermal alteration and are diagnostic of igneous provenance. All samples from the Escanaba Trough analyzed during Leg 169 plot as a tight cluster, firmly within the N-MORB field of this classification (following Meschede, 1986). There is no evidence from the data available that lavas with E-MORB affinities were recovered during Leg 169.

Magmatic fractionation within the Hole 1037B basalts and other magmas recovered from the Escanaba Trough are compared in Figure 9, which plots the TiO_2 content against Mg# (where Mg# = 100* (Mg^{2+}/[Mg^{2+}+Fe^{2+}]), for FeO = 0.9*FeO^{Total}). Data from Davis and Clague (1987) and Davis et al. (1994) are shown for comparison. Basaltic glasses from the Escanaba Trough display a strong trend of increasing TiO_2 content with decreasing Mg#, indicative of magmatic

Table 5. Whole-rock geochemical analyses of basalts from the Escanaba Trough, Holes 1037B and 1038G.

Hole:	1037B	1037B	1037B	1037B	1037B	1037B	1037B	1038G
Core, section:	57R-1	58R-1	58R-2	60R-1	61R-1	62R-1	62R-3	16X-1
Interval (cm):	48–51	64–68	65–70	118–122	104–112	124–129	81–86	0–6
Piece:	8C	6	9B	11C	2	5B	6	1A
Depth (mbsf):	508.28	517.91	519.33	530.58	534.94	539.24	541.53	144.50
Major element (oxide wt%):								
SiO_2	49.80	49.80	49.60	50.10	49.80	49.40	49.60	49.80
TiO_2	2.17	2.13	2.04	2.14	2.18	2.12	1.61	1.74
Al_2O_3	14.48	14.52	14.64	14.65	14.24	14.37	15.44	14.96
Fe_2O_3	12.72	11.97	11.65	12.56	12.40	12.26	10.91	11.15
MnO	0.20	0.19	0.17	0.20	0.21	0.20	0.18	0.18
MgO	7.63	8.26	8.56	7.61	6.90	7.00	8.59	7.70
CaO	10.81	10.51	10.28	11.06	11.17	11.34	11.67	11.53
Na_2O	1.86	2.36	2.39	1.88	2.05	1.91	1.83	1.50
K_2O	0.39	0.57	0.87	0.32	0.23	0.31	0.17	0.73
P_2O_5	0.19	0.18	0.17	0.18	0.19	0.18	0.12	0.15
Total	100.26	100.49	100.37	100.70	99.37	99.10	100.12	99.44
LOI	0.47	1.07	0.62	0.52	–0.19	0.55*	0.30	1.13
S(total)	0.00	0.00	0.00	0.00	0.00	0.00	0.04	0.00
Trace elements (ppm):								
Nb	7	6	7	6	6	6	4	6
Zr	154	146	141	145	148	141	93	120
Y	42	42	40	42	44	42	31	34
Sr	117	126	126	128	129	131	129	144
Rb	11	16	24	9	5	10	4	31
Zn	96	55	49	78	86	71	70	58
Cu	59	20	17	61	58	18	58	74
Ni	103	124	138	105	78	87	122	101
Cr	244	224	256	191	222	232	340	237
V	377	350	354	334	355	365	280	318
Ce	29	15	17	22	30	21	21	22
Ba	20	51	42	25	24	42	17	65

Notes: * = minimum value (crucible broke during measurement). LOI = loss on ignition.

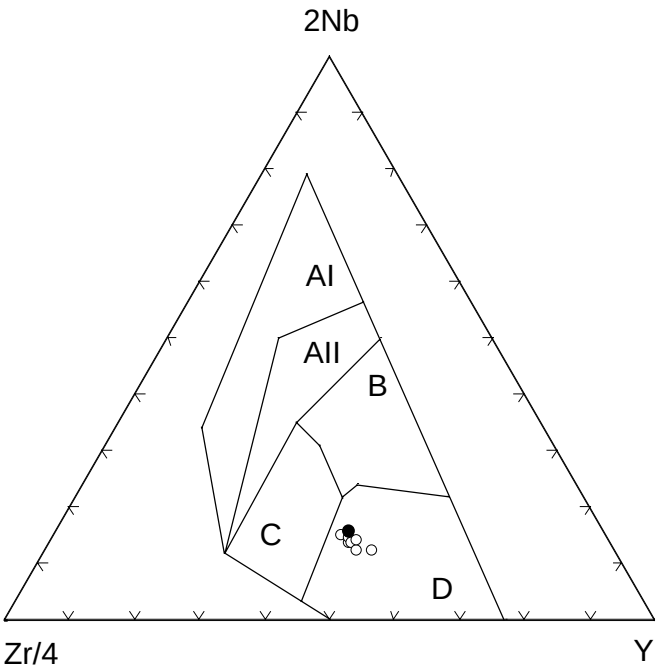

Where:

AI - within-plate alkali basalts
AII - within-plate alkali basalts and within-plate tholeiites
B - E-type MORB
C - within-plate tholeiites and volcanic-arc basalts
D - N-type MORB and volcanic-arc basalts

Figure 8. Nb-Zr-Y immobile element ternary diagram for classifying basalts showing Leg 169 basalt data from the Escanaba Trough (after Meschede, 1986). Open circles = 1037B basalts, and solid circle = 1038G basalt.

fractionation, which generally agrees with glass data from the northern Gorda Ridge (Davis and Clague, 1987). The single analysis of basalt from Central Hill (Sample 169-1038G-16X-1, 0–6 cm) plots close to the glass data, but samples from Hole 1037B show an unusual concave downward trend. Comparisons of the glass data with variations in FeO^{Total} and MgO contents vs. TiO_2 suggest that significant quantities of Mg have been added to some of the basalts from Hole 1037B, but both the low LOI, and the petrographically unaltered condition of the primary opaque phase (Ti magnetite) do not indicate significant metasomatic changes in these basalts (e.g., no large volume/mass loss/gain). The two samples that fall farthest from the glass trend on Figure 9 are both from Core 169-1037B-58R. Petrographic observation of actinolitic hornblende and stilpnomelane-filled voids and fractures, as well as replaced altered phenocrysts and groundmass within these samples, indicates interaction with high-temperature (>250°C), hydrothermal fluids. If these two samples are discounted because of significant alteration, then the Escanaba basalts fall more or less along the same fractionation trend as the Davis et al. (1994) glass data, although most samples are more fractionated than have been previously documented from this section of spreading ridge.

STRUCTURAL GEOLOGY

Hole 1037B

Hole 1037B was drilled to obtain an unaltered and undeformed section of oceanic crust to compare with the structurally controlled, hydrothermally altered Central Hill hydrothermal site. The objectives of this hole were met with a degree of success unparalleled in ocean drilling. The sedimentary sequence of Hole 1037B is devoid of deformation structure and hydrothermal veins, and sedimentary beds dip within 2° to 3° of horizontal. No evidence of faulting or tectonic tilting has been observed within the reference hole.

The only hydrothermal veins occur within basalt starting in Section 169-1037B-58R-1 (Table 6). Sections 169-1037B-58R-1, 58R-2, and 59R-1, are characterized by <1-mm-wide subhorizontal to subvertical Mg-hornblende veins. Euhedral Mg-hornblende crystals line

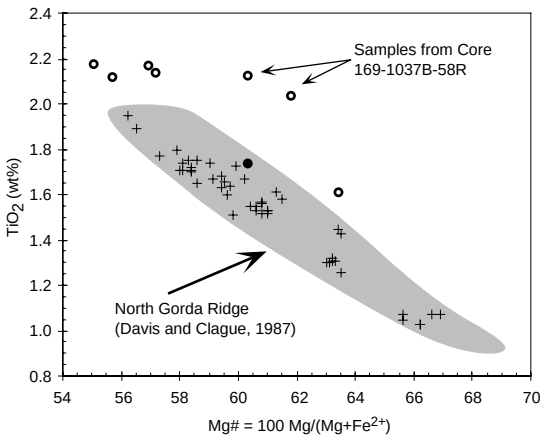

Figure 9. TiO_2 vs. Mg# (where Mg# = 100* (Mg^{2+}/[Mg^{2+}+Fe^{2+}]), for FeO = 0.9*FeO^{Total}) showing magmatic fractionation within the Hole 1037B basalts and other magmas recovered from the Escanaba Trough. Open circles = 1037B basalts, solid circle = 1038G basalt, and + = glass analyses of Davis et al. (1994).

and grow into vugs and extension fractures and indicate that high temperature fluids flowed through the extension fractures. Some Mg-hornblende veins exhibit 4-mm-wide whitish, probably silicified alteration halos (Fig. 10; interval 169-1037B-58R-2, 71–77 cm).

Beginning in Section 169-1037B-62R-1, the vein composition, identified by XRD, is commonly albite, smectite, and Mg-hornblende/actinolite. A near vertical, 2- to 3-mm-wide albite, calcite, and Mg-smectite vein extends through Section 169-1037B-62R-2 and continues in the following core. No crosscutting relationships were observed between the actinolite and calcite/albite veins within this section. However, in Section 169-1037B-58R-1, we observed calcite filling in an actinolite-lined vein. This observation is consistent with decreasing temperature with time.

Basalt in Cores 169-1037B-59R and 60R exhibit a curious alteration where seemingly solid basalt, after being cut, disintegrates upon drying. The rock does not exhibit any evidence of faulting, but it does appear that the basalt has been extensively hydrothermally altered. The primary fluid pathways appear to be several narrow (<1 mm) actinolite and chlorite veins. A conjugate set of fractures filled with actinolite occurs within interval 169-1037B-59R-1, 40–60 cm, and several other subvertical, <1-mm-wide chlorite veins occur throughout the core.

The lack of hydrothermal veining and sediment induration within the sedimentary sequence indicates that high temperature hydrothermal fluids did not circulate within the sediments. The relatively fresh appearance of the diabase and the narrow alteration halos associated with the actinolite veins indicate that fluid flow was primarily restricted to narrow fractures. The presence of the highly altered disintegrating basalt may indicate that a nearby fault fractured the basalt in these cores, allowing for the subsequent penetration of hydrothermal fluids. However, direct evidence for a nearby fault does not occur within the core.

INORGANIC GEOCHEMISTRY

Pore-water samples were collected from Site 1037 to provide the background information to evaluate the chemical composition of pore waters away from the hydrothermal upflow zone drilled at Site 1038 (Fig. 1). Two pore-water samples were collected from Hole 1037A, which was abandoned after the first core as it did not recover the mudline. Forty-nine samples were collected (usually at ~10-m intervals) from Hole 1037B, which was drilled to a depth of 546 mbsf and ~38 m into igneous basement. No samples were obtained from the first core at Hole 1037B; the two samples from Hole 1037A are

Table 6. Summary of structural features, Hole 1037B.

		Feature		Position		Veins			Apparent dips		Calculated			
Core, section	Depth (mbsf)	Oriented	Identifier	Top (cm)	Bottom (cm)	Mineralogy	Width (mm)	Wall rock	App dip/ dir1	App dip/ dir2	Strike	Dip	Dip direction	Comments
169-1037B-														
58R-1, (Piece 3)	517.49	Y	V1	19	27	Act	1	BAS	66/270	22/000	190	66	W	
58R-1 (Piece 3)	517.54	Y	V2	24	26	Cc	1	BAS	06/090	06/180	045	08	E	Calcite veins cut actinolite veins
58R-1 (Piece 3)	517.55	Y	V1a	25	35	Chl	1	BAS	67/270	59/000	215	71	W	
58R-1 (Piece 3)	517.63	Y	V1b	33	33	ChlAct	1	BAS	09/270	06/180	146	11	W	
58R-1 (Piece 4)	517.77	Y	V	47	52	Cc	1	BAS	38/090	29/180	035	44	E	
58R-1 (Piece 7)	518.04	Y	V	74	78	ClyChl	4	BAS	67/270	21/180	171	67	W	
58R-1 (Piece 8)	518.24	Y	V	94	96	Act	1	BAS	19/090	12/000	328	22	E	
58R-1 (Piece 9)	518.52	N	V	122	126	Act	1	BAS						Fine web of actinolite veins <1mm
58R-2 (Piece 1)	518.73	Y	V1	3	3	Act	2	BAS	34/270	02/180	177	34	W	Euhedral actinolite growing into fracture
58R-2 (Piece 1)	518.72	Y	V2	2	9	CcAct	2	BAS			190	90		Calcite infills around actinolite crystals
58R-2 (Piece 3)	518.91	N	V	21	24	Mg	1	BAS						
58R-2 (Piece 5)	519.04	N	V	34	34	Act	1	BAS						Web of actinolite veins
58R-2 (Piece 8)	519.24	Y	V	54	57	Act	3	BAS	62/270	13/180	173	62	W	
58R-2 (Piece 9B)	519.44	Y	V	74	74	Act	4	BAS	06/270	13/180	114	14	W	
59R-1 (Piece 2)	526.90	Y	V	10	10	Act	1	BAS	12/270	31/180	109	33	W	4-mm alteration halos
59R-1 (Piece 2)	526.93	Y	V	13	13	Act	1	BAS						4-mm alteration halos
59R-1 (Piece 4)	527.03	Y	V	23	23	Act	0.5	BAS	05/270	34/000	263	34	W	
59R-1 (Piece 7)	527.20	Y	V1a	40	50	Act	0.5	BAS	62/090	52/000	326	66	E	
59R-1 (Piece 7)	527.25	Y	V1b	45	54	Act	0.5	BAS						
59R-1 (Piece 7)	527.23	Y	J	43	53				68/270	71/180	130	75	W	
61R-1	534.00	N	V	10	17	Chl	0.1	BAS				64	E	Apparent dip of joint
62R-1 (Piece 5)	538.43	Y	V	43	50	Zeo	2	BAS	54/090	56/000	313	64	E	
62R-1 (Piece 5)	539.05	Y	V	105	114	Zeo	1	BAS						Diffuse zeolite vein with no orientation
62R-2 (Piece 1)	539.74	Y	V	35	135	Zeo	3	BAS			180	90		
62R-3 (Piece 1)	540.84	Y	V	12	37	Zeo	3	BAS			180	90		

Note: Y = oriented, N= not oriented, V= vein, J = joint, Act = actinolite, Cc = calcite, Chl = chlorite, ChlAct = chlorite-actinolite, ClyChl = clay-chlorite, Mg = magnesiohornblende, Zeo = zeolite, BAS = basalt, E = east, and W = west.

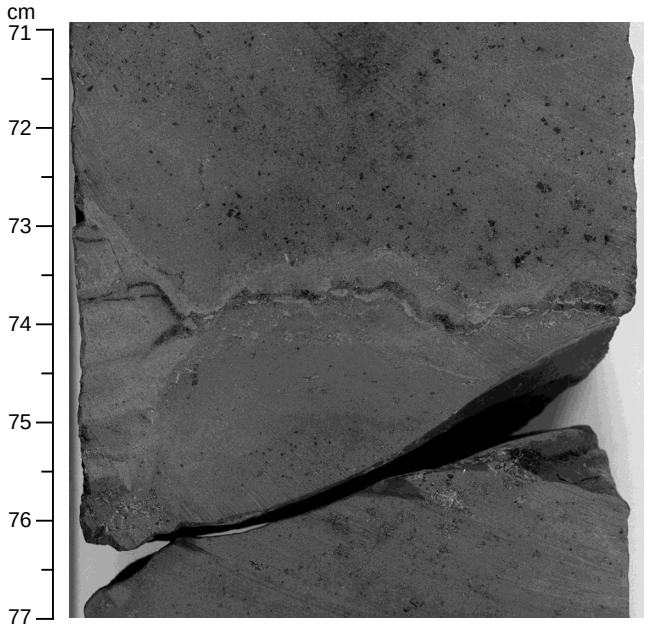

Figure 10. Interval 169-1037B-58R-2, 71–77 cm. Euhedral crystals of actinolite line and grow into probable thermal contraction cracks; 4-mm-wide alteration halos line the veins.

considered to equate with this first core, and the results of analyses are discussed as such. No pore-water samples were obtained between 80 and 120 mbsf, as a sand layer was encountered and extensive core disturbance precluded meaningful pore-fluid analysis.

Adara temperature measurements obtained in the upper sediment section (see "Downhole Measurements" section, this chapter) suggest a geothermal gradient that implies a temperature of ~84°C at the base of the sediment section (~508 mbsf). This is close to the temperature estimated for the basement/sediment interface after heat-flow measurements (Davis and Becker, 1994).

The age of the sediments at the base of the sediment column may be younger than 200 ka (see "Biostratigraphy" section, this chapter), which would imply an overall sedimentation rate of >2.5 m/k.y. Normark et al. (1994) have suggested that Pleistocene sedimentation rates in this region may be as high as 8 m/k.y.

All pore-water samples were squeezed from whole-round sections of core, and shipboard chemical analyses were performed according to the methods given by Gieskes et al. (1991). A few samples show minor contamination with seawater based on their SO_4 content; this is discussed further below.

Results

Results of the chemical analyses of pore fluids from Site 1037 are given in Table 7 and are plotted as a profile vs. depth in Figure 11 to facilitate discussion.

Alkali Elements

Concentrations of Na appear to fall in the unsampled sand layer, then increase steadily between 150 and 360 mbsf. There is a marked change in the Na depth profile at 360 mbsf, where the Na concentration of pore waters falls sharply. Below 400 mbsf, concentrations of Na increase slowly, then fall sharply as basement is approached. The Na/Cl value of the pore waters shows a concentration depth profile similar to Na, although the gradients are more pronounced, particularly in the interval between 360 mbsf and basement.

The K content of the pore fluids is similar to seawater (~10 mM), between 0 and 250 mbsf, then falls to ~2 mM at 360 mbsf. Below this depth, the K concentration remains at ~2 mM, then sharply increases below 500 mbsf in the approach to basement.

Concentrations of Li in the pore fluids are slightly lower (~10 µM) than seawater (27 µM) in the upper ~200 m of the sediment column. Below this depth, the concentration depth profile of Li is dominated by two peaks, centered at 330 and 430 mbsf, recording Li contents up to ~360 µM and ~300 µM, respectively. The rapid sedimentation rate in the Escanaba Trough means that diffusive processes are limited, thereby aiding the preservation of the peaks.

Alkali Earth Elements

Concentrations of Ca in the pore fluids are similar to seawater in the upper 200 m of the core, showing a slight reduction in the vicinity of the sand layer. Below 200 mbsf, Ca increases slowly, then increases sharply at ~360 mbsf, attaining a maximum at 420 mbsf. Below this depth, the Ca content of the pore fluids falls, then increases slightly below 480 mbsf.

The concentration depth profile of Mg shows a gradual reduction in the Mg content of the pore fluids with depth. The decline in the Mg content is more marked in the vicinity of the sand layer. Concentrations of Mg increase slightly as basement is approached.

The Sr content of the pore waters is similar to seawater in the upper ~300 m of sediment, then increases to a maximum at ~460 mbsf before declining sharply on the approach to basement.

Chloride

Between ~160 and 350 mbsf, the Cl content of the pore fluids is roughly constant (~569 mM), but decreases sharply towards seawater values (558 mM) in the vicinity of the sand layer. Below 350 mbsf, there is an increase in Cl to a maximum of 580 mM at 415 mbsf. Below this depth, the concentration of Cl falls sharply to ~554 mM before increasing on approach to basement.

Nutrient Elements

In this section, we consider the SO_4, alkalinity (HCO_3), and NH_4 contents of pore fluids. The concentration depth profile of SO_4 declines sharply below the seawater/sediment interface, reaching effectively zero at ~100 mbsf. Below this depth, a few samples have nonzero SO_4 concentrations; we believe this is a result of minor contamination of the sample with seawater introduced during drilling. One sample just above basement shows greater contamination, attaining an SO_4 concentration of 10 mM.

Pore-fluid alkalinity increases with depth between the surface and the sand layer (~80 mbsf). Alkalinity falls sharply within the sand layer, then increases until 160 mbsf. Below 160 mbsf, there is a gradual fall in alkalinity values. Alkalinity measurements were not performed on samples close to basement because of limited sample quantities.

The concentration depth profile for NH_4 is rather similar to, though more pronounced than, the alkalinity profile. There is an increase in NH_4 with depth between the seawater/sediment interface and the sand layer, with a fall in NH_4 concentrations within the sand layer. NH_4 increases erratically below the sand layer, attaining a maximum at ~320 mbsf. Below this depth, there is a sharp decline in the NH_4 content of the pore fluids to ~400 mbsf. Below 400 mbsf, the concentration of NH_4 is roughly constant (~1.5 mM).

Boron and Silica

Concentrations of B are slightly greater than seawater in the upper 120 m of the sediment column. Between 120 and 360 mbsf, the B

Table 7. Chemical composition of pore fluids from Site 1037.

Core, section, interval (cm)	Depth (mbsf)	Cl (mM)	Salinity	pH	Alkalinity (mM)	SO_4 (mM)	NH_4 (mM)	Ca (mM)	Mg (mM)	Sr (µM)	Li (µM)	K (mM)	Na (mM)	Na/Cl	B (µM)	H_4SiO_4 (µM)
169-1037A-																
1H-2, 140–150	6.0	558	35	7.5	4.54	32.4	0.25	9.9	49.8	80	15	11.7	496	0.89	547	593
1H-4, 140–150	9.0	556	35	7.4	4.63	24.9	0.44	10.5	50.4	82	11	11.3	477	0.86	495	510
169-1037B-																
2H-2, 140–150	9.6	556	35	7.4	5.06	25.8	0.54	10.5	49.7	82	10	11.1	481	0.86	443	537
2H-4, 149–150	12.6	555	35	7.1	5.87	25.3	0.82	10.5	50.1	83	10	10.6	478	0.86	455	603
3H-2, 140–150	19.1	556	35	7.5	7.84	24.6	1.34	11.4	50.6	83	11	9.7	478	0.86	483	556
3H-4, 140–150	22.1	555	37	7.3	7.81	23.5	1.57	11.0	50.2	87	10	9.4	476	0.86	499	712
4H-3, 140–150	30.1	556	38	7.6	12.59	22.7	2.37	11.6	49.9	93	10	9.3	479	0.86	511	682
5H-3, 140–150	39.6	555	35	7.3	16.56	20.0	2.85	11.9	50.5	97	10	9.5	475	0.86	539	676
6H-3, 140–150	49.1	558	35	7.6	21.71	18.5	3.01	9.5	51.5	87	10	10.3	480	0.86	606	637
7H-2, 140–150	58.6	559	35	7.4	30.55	14.5	3.23	7.3	51.0	68	10	10.2	488	0.87	590	693
8H-3, 140–150	68.1	558	35	7.6	37.50	7.0	3.07	6.9	47.7	82	9	9.6	488	0.87	555	797
9H-3, 140–150	77.6	557	34	7.4	42.51	2.3	3.11	6.8	46.4	104	10	10.4	484	0.87	539	616
14H-3, 140–150	125.0	562	34	7.6	19.86	0.0	1.35	5.8	41.8	110	10	8.1	476	0.85	539	752
15H-3, 140–150	134.6	564	36	7.3	20.56	0.4	2.06	9.4	41.7	109	11	7.9	472	0.84	471	784
16H-3, 140–150	143.1	564	36	7.3	23.15	0.2	2.75	9.2	44.6	111	20	8.2	468	0.83	386	644
17H-3, 140–150	153.6	566	36	7.2	27.87	0.4	3.45	8.7	46.2	108	11	8.3	473	0.84	437	729
18H-3, 140–150	163.1	567	38	7.4	33.30	0.4	3.51	7.3	48.5	93	13	7.7	479	0.85	354	708
20X-3, 140–150	172.6	568	37	7.6	32.62	0.5	3.47	6.6	45.1	86	14	7.9	487	0.86	428	788
22X-2, 140–150	196.7	568	40	7.4	30.82	0.0	3.55	5.9	45.6	91	18	8.1	484	0.85	444	835
23X-3, 140–150	206.3	568	37	7.3	27.77	2.9	4.02	6.7	40.3	93	26	8.6	496	0.87	390	1010
25X-3, 140–150	225.5	567	37	7.5	24.35	1.5	5.10	9.3	38.4	107	37	7.8	486	0.86	467	879
26X-3, 140–150	235.1	570	34	7.5	25.67	0.4	5.54	10.3	37.5	110	39	8.9	487	0.85	470	912
27X-2, 140–150	243.2	571		7.4	23.07	0.8	5.55	10.4	35.1	114	57	8.9	489	0.86	473	972
28X-3, 140–150	254.3	568	38	7.5	23.40	0.3	5.66	12.4	32.1	120	64	9.0	490	0.86	441	866
29X-3, 140–150	264.0	569	38	7.4	21.85	1.4	5.35	13.1	30.7	123	67	6.8	496	0.87	435	502
30X-3, 140–150	273.5	569	36	7.6	21.28	0.0	5.03	13.1	29.5	125	77	5.4	495	0.87	351	468
31X-3, 140–150	283.0	570	37	7.5	16.83	1.1	5.15	14.1	27.5	120	86	4.7	496	0.87	393	408
32X-3, 140–150	292.6	570	36	7.4	16.88	0.8	5.42	14.6	27.9	121	97	5.0	493	0.87	395	672
33X-3, 140–150	302.2	567	38	7.5	14.34	1.8	5.35	13.7	28.9	131	151	4.9	489	0.86	403	412
34X-4, 140–150	311.8	570	36	7.5	15.34	1.9	5.77	14.4	26.4	143	256	5.2	497	0.87	483	474
35X-4, 140–150	321.4	567	35	7.4	15.69	5.1	6.41	14.7	24.4	157	354	4.5	505	0.89	466	410
36X-1, 140–150	328.0	566	33	7.7	13.81	1.0	6.14	12.6	22.2	165	358	4.0	501	0.89	462	359
37X-4, 140–150	342.1	570	33	7.6	10.81	1.3	4.53	12.2	21.8	192	297	2.3	508	0.89	462	258
38X-4, 140–150	351.7	576	32		6.00	1.5	4.13	14.2	17.3	212	220	2.4	515	0.89	462	171
39X-3, 140–150	360.0	573	33	7.7	4.51	0.4	3.19	19.4	14.2	245	161	1.4	505	0.88	575	208
40X-3, 140–150	369.5	573	33	7.6	4.05	0.0	2.69	22.0	15.4	279	125	1.3	498	0.87	546	173
41X-1, 140–150	376.2	572	33	7.8	4.04	2.8	2.72	21.7	17.0	228	113	1.7	499	0.87	744	379
42X-2, 140–150	387.3	580	36	7.7		0.0	1.90	26.6	14.7	304	124	1.7	496	0.86	563	167
43X-3, 140–150	398.4	577	33	7.5		1.3	1.75	27.3	15.1	339	122	1.5	494	0.86	638	188
44X-2, 140–150	406.6	578	36	7.8	3.47	1.5	2.12	26.7	15.1	350	120	1.4	497	0.86	920	344
45X-3, 140–150	417.7	581	34	7.9	2.21	2.8	1.78	29.1	12.4	431	117	2.0	502	0.86	759	133
46X-3, 140–150	427.3	573	34	7.9	1.78	0.0	1.44	25.1	7.8	530	102	1.8	506	0.88	671	169
47X-1, 140–150	433.9	567	32	7.9	2.01	0.0	1.69	27.8	8.2	582	106	1.7	496	0.88	721	139
48X-3, 140–150	446.5	558	32	7.7	4.23	3.1	1.24	19.6	6.7	599	119	1.9	512	0.92	721	186
49X-3, 140–150	456.1	558	32			0.3	1.19	17.1	4.5	674	166	2.1	513	0.92	944	184
50X-3, 140–150	465.8	554	32			2.0	1.00	15.0	7.1	640	221	3.5	509	0.92	1076	193
51X-1, 140–150	472.4	557				0.7	1.26	15.1	4.3	692	301	5.0	515	0.92	1408	191
52X-3, 140–150	485.0	565	34			1.5	1.43	14.5	5.7	593	304	4.2	524	0.93	1240	161
53X-1, 140–150	491.6	570	37	7.7		0.0	1.89	18.5	6.7	489	238	4.8	516	0.90	1434	214
55X-CC, 15–20	501.0	559				9.8	1.78	24.8	12.4	210	185	26.3	476	0.85	981	611
56R-1, 30–37	501.5	568				2.6	1.74	21.3	13.5	205	108	25.3	478	0.84	624	98
Seawater:	0.0	558	35	7.5	2.45	28.0	0.00	10.6	54.0	87	27	10.4	477	0.85	420	170

content is roughly constant at ~400 µM, then below 360 mbsf, concentrations of B increase sharply to >1000 µM. On approach to basement, B concentrations rapidly fall.

Although there are a number of inherent difficulties in the interpretation of H_4SiO_4 in squeezed pore-water samples, there are salient features in the profile obtained worth reporting. H_4SiO_4 increases sharply below the sediment/seawater interface to a depth of ~250 mbsf, where the H_4SiO_4 content of the pore fluids declines. Below ~360 mbsf, H_4SiO_4 is relatively constant (~200 µM). One sample above basement shows a rather higher H_4SiO_4 content; as discussed above, the integrity of this sample is questionable, and no further commentary on this data point is appropriate.

Discussion

The relatively rapid sedimentation rate in the Escanaba Trough means that chemical signatures in pore waters in this area are exceptionally well preserved; diffusive processes are likely to influence signals over only a few tens of meters (Gieskes, 1975). This permits interpretation of the pore-water concentration depth profiles in terms of sedimentary provenance and diagenetic features.

Influence of Sedimentary Sources on Pore-Water Profiles

The concentration depth profiles of several species (Na, K, Ca, Cl, B, H_4SiO_4, NH_4, and possibly Sr) show a sudden change at ~360 mbsf near the boundary between lithologic Units VII and VIII. This depth corresponds to an inferred change in the principal source of sediment fill in the Escanaba Trough from the Columbia River to the Klamath Mountains (see "Lithostratigraphy" section, this chapter). These two sediment provenances have rather different mineral assemblages; sediments from the Columbia River include material derived from volcanic rocks and are pyroxene rich, whereas sediments from the Klamath Mountains are amphibole rich (e.g., Vallier et al., 1973; Zuffa et al., in press). Figure 11 suggests that sediments from the Klamath region are a source of Na, Ca, Li, and B to the pore waters and a sink for K, alkalinity, and NH_4.

Diagenetic Alteration of Sediments

The coincident alkalinity maximum and SO_4 minimum at ~90 mbsf is principally because of sulfate reduction in the upper part of the sediment column. Calcite cementation is observed between 250

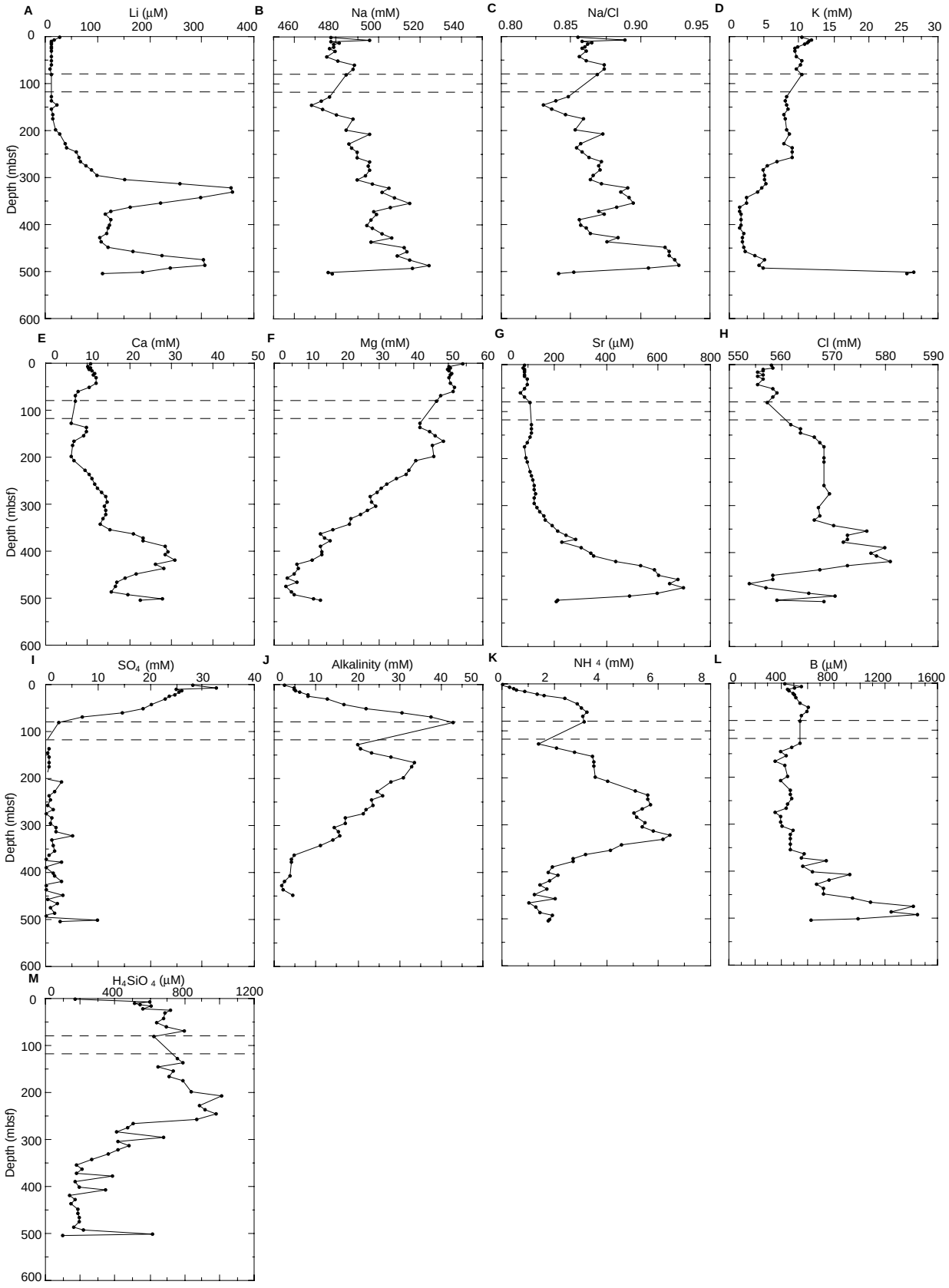

Figure 11. Concentration in pore waters plotted as a function of depth of (**A**) Li, (**B**) Na, (**C**) Na/Cl, (**D**) K, (**E**) Ca, (**F**) Mg, (**G**) Sr, (**H**) Cl, (**I**) SO_4, (**J**) alkalinity, (**K**) NH_4, (**L**) B, and (**M**) H_4SiO_4. The dashed lines denote the unsampled sand layer.

and 500 mbsf and may be related to the small increase in the Ca concentration of pore waters (and a corresponding reduction in alkalinity) between 200 and 360 mbsf.

Chemical Alteration of Sediments

The reduction in the concentration of Mg in the pore fluids with depth is more or less continuous below ~250 mbsf. In view of limited diffusion at this site, this implies removal of Mg, probably a result of uptake onto clay mineral phases throughout the sediment column. The gradient in the Mg profile is steeper at depth in the sediment column; therefore, this suggests that uptake of Mg is thermally enhanced. Smectite has been identified in a glycolated XRD sample from 328 mbsf (Section 169-1037B-36X-1); formation of smectite is a well-established sink for Mg in pore fluids (e.g., Kastner and Gieskes, 1976). Similarly, the almost continuous reduction in the K content of the pore fluids with depth is likely because of alteration of clay mineral phases, possibly including the formation of K-feldspar (Kastner, 1976). Uptake of K is clearly enhanced in the sediments below ~350 mbsf that are interpreted to have been derived from the Klamath Mountains.

The distinct maxima in the Sr profile may be related to its release from authigenic silicate minerals present in the Klamath sediments. Sr release from silicate phases has been suggested to explain similar peaks in pore-water Sr profiles from the New Hebrides forearc and intra-arc Auba Basin by Martin (1994).

Similarly, the two distinct maxima in the Li profile may be related to release from silicate phases. The uppermost Li-rich peak (298–367 mbsf) is associated with a distinct lithologic unit (Unit VII; see "Lithostratigraphy and Sedimentology" section, this chapter). An XRD analysis of the squeezed sediment cake associated with the pore-fluid sample from Section 169-1037B-36X-1 (328 mbsf) tentatively suggests that the sediment in this layer contains lepidolite, which is a mica-containing Li. It is possible that chemical alteration of this mineral, combined with limited diffusion, is sufficient to produce the distinct maximum. A similar mechanism may produce the Li maximum lower in the core. Experimental studies have suggested that release of Li from sediments occurs at a temperature as low as 62°C (Chan et al., 1994) that is consistent with the estimated temperature at the base of this hole (~84°C; see "Downhole Measurements" section, this chapter). Above 200 mbsf, Li concentrations are lower than seawater, consistent with continuous uptake of Li into authigenic silicate phases at low temperature.

Interaction with Sediment/Igneous Basement Complex

Several of the concentration depth profiles at Site 1037 show marked changes in gradient toward basement. Concentrations of K and Ca both increase toward the base of the hole, whereas concentrations of H_4SiO_4, Sr, B, Li, Na, and the Na/Cl values decrease. In this connection, it should be noted that a distinct sedimentary unit occurs immediately above the first occurrence of igneous material. This unit is ~9 m thick, and principally comprises calcareous, partly silicified claystones (see "Lithostratigraphy and Sedimentology" section, this chapter). Because removal of Li (and B) into basalt at low temperature is usually accompanied by removal of K, it is possible that chemical alteration of the calcareous sediments immediately above the igneous material is controlling the changes in the pore-water profiles at the base of the hole. These sediments appear to be a source of K and Ca, but take up H_4SiO_4, Sr, B, Li, and Na. Uptake of Na is not accompanied by a loss of Cl, and the Na/Cl ratio of the pore fluids decreases. In part, these results may have been caused by hydrothermal interactions in the sediments below ~450 mbsf (see "Igneous Petrology and Geochemistry" section, this chapter) followed by retrograde reactions. This is also reflected in the organic geochemistry below 450 mbsf (see "Organic Geochemistry" section, this chapter).

Conclusions

The rapid sedimentation rate in the Escanaba Trough means that the chemical signature of pore fluids from Site 1037 is exceptionally well preserved. A key feature of the pore-water concentration depth profiles is the marked change in the concentrations of Na, K, Ca, Cl, B, H_4SiO_4, NH_4, and the Na/Cl value that occurs at ~360 mbsf. This change coincides with an inferred shift in the principal source of sediment fill at Escanaba from the Columbia River to the Klamath Mountains. A further key feature of the pore-fluid data is a sudden change in the concentrations of K, Ca, H_4SiO_4, Sr, B, Li, Na, and the Na/Cl value as basement is approached. We argue that this signature is derived from the narrow layer of calcareous claystones immediately above the igneous material rather than direct interaction with basalt.

Interesting perturbations in pore-water profiles also occur for individual elements; these are largely related to the chemical alteration of the sediments. The concentration depth profile of Li is dominated by two sharp peaks at 330 and 430 mbsf. These appear to be related to alteration of a Li-bearing silicate phase. Alteration of authigenic silicate phases may also be important in controlling the Sr concentration of the pore fluids. Mg is removed throughout the sediment column below ~250 mbsf, probably into clay mineral phases. XRD data suggest that smectite formation is an important mechanism for Mg removal from pore fluids at Site 1037.

ORGANIC GEOCHEMISTRY

Shipboard gas analyses were carried out on headspace gas from Site 1037 sediments. Solvent extracts of bitumen from sediments were analyzed for fluorescence and by gas chromatography (GC) to assess the sources of the organic matter and its maturity. Routine elemental analyses were performed on sediments for total C, N, and S, and carbonate C. Instrumentation, operating conditions, and procedures are summarized in the "Explanatory Notes" chapter (this volume).

Volatile Gases

The headspace gas composition monitored for downcore sediment samples from Site 1037 is given in Table 8. The methane concentrations vary from 2 to 45,000 ppm, with a broad maximum from 190 to 340 mbsf. Below 420 mbsf, methane increases with depth because of increased temperature (Fig. 12). It should be pointed out that these sediments have relatively low contents of gas and volatiles (mainly CH_4) compared to gas formed from the more aliphatic marine organic matter in Guaymas Basin, Gulf of California (Simoneit et al., 1988; Kvenvolden and Simoneit, 1990). This is because of the dominant terrigenous composition of the sedimentary organic matter that is composed of *n*-alkanes with C_{max} at C_{29} or C_{31} derived from vegetation waxes, wood fragments, and pollen from terrestrial plants. The hydrocarbon composition of gas voids sampled by vacutainers is almost pure methane (Table 8) because of its faster effusion from the indurated sediments compared to ethane and higher hydrocarbons. The vacutainer data are not plotted in the depth profile. Ethane and higher hydrocarbons appear below 200 mbsf and increase significantly below 440 mbsf (Fig. 12B). The C_1–C_3 hydrocarbon profile is comparable to the trends described for Middle Valley Site 858 (Shipboard Scientific Party, 1992). The C_1/C_2 ratios are high and erratic from 200 to 330 mbsf, consistent with biogenic CH_4 formation in shallower sections, and then decrease to <100 below 330 mbsf, indicating thermogenic CH_4 generation because of increased temperatures. Thermogenic methane generation in conventional basins typically occurs over a temperature range of 120° to 160°C (Tissot and Welte, 1984). C_1/C_2 ratios for biogenic CH_4 are generally taken as

Table 8. Composition of gas in headspace or void samples derived from sediments at Site 1037.

Core, section, interval (cm)	Sample Type	Depth (mbsf)	CH_4 (ppm)	C_2 (ppm)	C_2H_4 (ppm)	C_3 (ppm)	Total C_4 (ppm)	Total C_5 (ppm)	Total C_6 (ppm)	CO_2 (ppm)	C_1/C_2
169-1037A-											
1H-4, 135–140	HS	5.88	2								
169-1037B-											
1H-4, 0–3	HS	4.52	2								
2H-4, 0–5	HS	11.12	2								
3H-5, 0–5	HS	22.12	2							580	
4H-3, 135–140	HS	29.98	2								
5H-3, 135–140	HS	39.48	2								
6H-3, 135–140	HS	48.98	2							1,960	
7H-2, 135–140	HS	56.98	3								
8H-3, 135–140	HS	67.98	2							1,978	
9H-3, 135–140	HS	77.48	2							1,157	
14H-3, 135–140	HS	124.98	195							1,222	
15H-3, 135–140	HS	134.48	403							3,634	
16H-4, 0–5	HS	144.42	294							2,023	
17H-4, 135–140	HS	154.98	2,262							23,755	
18H-3, 135–140	HS	162.98	1,285							18,445	
20X-3, 0–5	HS	180.62	1,295							4,282	
22X-1, 145–150	HS	194.18	10,223							21,090	
23X-5, 0–5	HS	207.82	31,950	1						13,300	31,950
25X-3, 135–140	HS	228.98	23,200	7						6,865	3,314
26X-3, 135–140	HS	236.38	15,700							9,533	
26X-3, 140–150	HS	236.45	30,120	1						11,520	30,120
27X-2, 135–140	HS	243.08	16,750	1						17,400	16,750
27X-2, 140–150	HS	243.15	16,400	1	1					7,700	16,400
28X-6, 0–5	HS	257.33	16,610	1	1					24,480	16,610
29X-3, 135–140	HS	263.78	26,394	2						22,310	14,854
30X-4, 0–5	HS	273.53	18,145	1						17,400	18,145
31X-6, 0–5	HS	286.03	9,554							12,600	
32X-2, 75	V	290.35	71,9600	180		165				5,850	3,998
32X-5, 0–5	HS	295.63	13,800	1						15,640	13,800
33X-3, 75	V	301.45	810,200							176	
33X-4, 0–5	HS	302.22	4,432	1						10,226	4,432
34X-3, 75	V	311.05	990,000	300		270				8,524	3,300
34X-5, 0–5	HS	313.33	19,970	1						2,970	19,970
35X-4, 0–5	HS	321.43	4,150							5,558	
36X-2, 0–5	HS	328.03	10,040	10						10,194	1,004
37X-3, 75	V	339.85	790,000	216		203				2,750	3,657
37X-5, 0–5	HS	342.13	6,370	5		1				3,314	1,274
38X-2, 75	V	347.95	804,500	302		210				1,155	2,664
38X-5, 0–5	HS	351.73	5,792	7		1				506	827
39X-2, 75	V	357.65	809,000	457		212				736	1,770
40X-4, 0–5	HS	369.53	5,500	26						17,180	212
41X-2, 0–5	HS	376.23	8,208	8						1,223	1,026
42X-2, 0–5	HS	385.83	6,100	22						4,166	277
43X-4, 0–5	HS	398.43	4,330	24		5				1,607	180
44X-2, 0–5	HS	405.13	5,770	10						3,980	577
44X-3, 100	V	407.6	114,200	97		5					1,177
45X-2, 135–140	HS	416.08	4,228	15		6				935	282
46X-3, 0–5	HS	425.83	6,950	37		11				489	188
47X-1, 145–150	HS	433.88	9,290	35		13				533	265
48X-4, 0–5	HS	446.53	22,652	201		96	58	18	2	1,140	113
49X-3, 135–140	HS	455.98	23,361	279		124	107	25	5	3,233	84
50X-4, 0–5	HS	465.83	19,000	324		95	46	4		3,546	59
51X-1, 135–140	HS	472.28	23,473	379		83	19			3,264	62
52X-4, 0–5	HS	485.03	45,124	670		81				4,082	67
53X-1, 135–140	HS	491.48	26,270	388		79				1,109	68

Note: HS = headspace, and V = vacutainer.

>1000 and for thermogenic CH_4 as <100 (Bernard et al., 1976). The gas composition below 440 mbsf reflects the result of a short-lived pulse of high-temperature alteration and fluid flow through the basalt unit after emplacement (see "Igneous Petrology and Geochemistry" section, this chapter). The current measured temperatures in Hole 1037B are relatively linear vs. depth, and the extrapolated temperature at 440 mbsf is ~75°C (see "Downhole Measurements" section, this chapter). This is also consistent with the low heat-flow measurements reported for the area away from the vent field and the predicted temperature of ~80°C for the sediment/basalt interface (Davis and Becker, 1994). Carbon dioxide occurs at high concentrations from 150 to 370 mbsf (Fig. 12D), and H_2S was not detectable.

Bitumen Fluorescence

Extracts from the near surface sediments at Site 1037 fluoresced yellow and became colorless in deeper sections. The extract yields were high in the shallow depths and low below 100 mbsf. These extracts had no fluorescence except the four deepest samples fluoresced faint yellow-white. The low extract yields and essential absence of fluorescence in the upper section of the hole indicate normal in situ maturation without product migration. The yellow-white fluorescence at depth is a diagnostic indicator of low thermal maturity, which is interpreted in this hole also as in situ maturation, but at greater temperatures than the shallower zones. It is estimated that this organic matter conversion occurred over a temperature range of 150°–250°C during an unknown but brief period of time. These extracts were analyzed by high-resolution GC for further interpretation.

Black Soot

Black soot (carbonaceous/mineral particulate matter) occurs in the deeper intervals of this hole, as was reported earlier for the hydrothermally altered sites in Middle Valley. Black soot was present in the lithified sediments at depth from 400 mbsf down to the deepest sediments in this hole and was especially prevalent in Section 169-

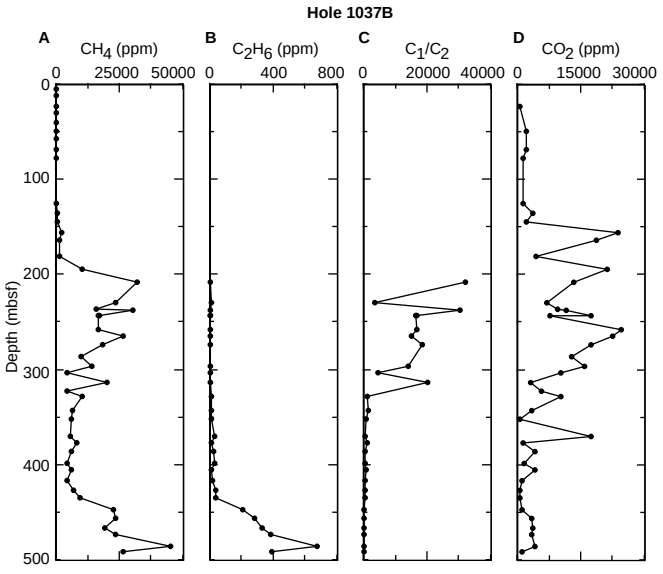

Figure 12. (**A**) Methane, (**B**) ethane, (**C**) C_1/C_2 ratio vs. depth, and (**D**) CO_2 concentrations for Hole 1037B.

1037B-56R-1. The black soot is interpreted in this case to represent the kerogen carbon residue after in situ generation of the bitumen.

Bitumen Analyses

The supernatant (hexane) layers from the hexane/methanol extracts of the sediment samples prepared for fluorescence evaluation or extracts of subsamples of freeze-dried sediments were concentrated under a stream of nitrogen to ~10-100 µL. These concentrates were analyzed by high-resolution GC, and typical traces are shown in Figure 13. The bitumen parameters for maturation and organic matter sources are listed in Table 9. Pristane (Pr) to *n*-C_{17} and phytane (Ph) to *n*-C_{18} ratios are not given because of the low concentrations of these compounds in many samples, although Pr/Ph is reported. Also the U^k_{37}' index (Shipboard Scientific Party, 1992; Simoneit et al., 1994) could not be determined for these samples, because the C_{37} alkenones also had low concentrations, and coeluting compounds interfered in the GC analyses.

Most of the sediments from Site 1037 are relatively unaltered and immature to ~450 mbsf. The *n*-alkanes >C_{24} have a strong predominance of odd carbon numbered homologs (carbon preference index [CPI] >1.0) and carbon number maximum (C_{max}) mainly at C_{29} or C_{31} (e.g., Fig. 13B or D). The CPI calculation range and odd carbon number preference are indicated in Figure 13B by the sawtooth connection drawn from C_{24} to C_{33}. This distribution is typical for immature hydrocarbons with an origin from terrestrial higher plants (mainly from epicuticular plant waxes; Simoneit, 1977, 1978). Immature microbial lipid residues from marine, autochthonous sources as reported earlier, for example, for some sediments from Middle Valley (Shipboard Scientific Party, 1992) are not found. The bitumens in some sediments of the upper intervals of Holes 1037A and 1037B have alkane distributions and relative amounts of the envelopes of the unresolved complex mixture of branched and cyclic hydrocarbons as is typical for mature bitumens (e.g., Fig. 13A, C). These appear to have been redeposited from eroded older formations by rapid turbidite sedimentation (Kvenvolden et al., 1994). The bitumens in the sediments below 400 mbsf have undergone accelerated in situ maturation because of higher than normal heat flow, probably from the brief thermal pulse as discussed earlier for the gases and not by contact with hydrothermal fluids. The maturity of these bitumens increases progressively with depth (e.g., Fig. 13D–F). They have not migrated, but reside in situ at an essentially uniform and low concentration in the deepest section of the hole, as was also observed for Site 1035.

The carbon number distributions and other geochemical parameters of these bitumens can be utilized to infer the source of the organic matter (Hunt, 1996). Hydrothermal petroleums, as reported earlier for the Middle Valley area (Shipboard Scientific Party, 1992; Simoneit, 1994; Simoneit et al., 1992) and found at Site 1036, are not present in these sediments.

The *n*-alkane predominances (C_{max}) at C_{27}, C_{29}, or C_{31} in the bitumen with the abundant plant fragments and pollen (observed by microscopic examination of a particle concentrate) indicate a significant terrigenous component. Accelerated maturation is evident from the CPI (range C_{24}–C_{33}) values that are near 1 below 450 mbsf in Hole 1037B (Fig. 14). This indicates full maturity and is caused by the higher than normal thermal gradient that generates additional alkanes from the kerogen (bulk organic carbon). The CPI <1 in some intervals with the strong even carbon number predominance from *n*-C_{16} to *n*-C_{34} should be pointed out. This was reported earlier for sediments from Escanaba Trough (Kvenvolden et al., 1994), Middle Valley (Shipboard Scientific Party, 1992; Simoneit, 1994), and for other geographic areas (e.g., Simoneit, 1977; Grimalt and Albaiges, 1987). It seems to be a characteristic of the source organic matter and also occurs in the deeper sediments recovered by drilling from the Escanaba Trough area. The thermal maturation of petroleums generally does not produce CPI values of <1, so the low CPI for this hole is partially source related. The variability of the CPI values for bitumen in the shallower intervals reflects the different maturities of the source inputs and the admixture of terrigenous with minor marine organic matter.

The isoprenoid alkane (Pr/Ph) ratios show considerable variation vs. depth for this hole (Fig. 14). This ratio is generally influenced by both source (e.g., Didyk et al., 1978) and maturation (e.g., Simoneit et al., 1981). The Pr/Ph approaches low values at intermittent intervals in shallower horizons of this hole as well as at depth. This may be a reflection of primary organic matter sources in the shallower horizons and full maturation at depth.

Elemental Analyses

The results of the total C, N, and S measurements for sediments from Hole 1037B are given in Table 10, and depth profiles are shown in Figure 15. Total carbon and carbonate carbon range from 0.5% to 1.8% and 0% to 1.1%, respectively, throughout the section drilled. The organic carbon determined by difference is not as reliable because of the significant analytical error at low values between the two methods. It is low and ranges from 0% to 1.1%, with no major trends except for a sharp decrease from the seabed interval. The nitrogen content varies from 0% to 0.14%, also showing a sharp drop from the maximum in the seabed interval. Sulfur shows two maxima, one of 0.15% near the seabed and a second with a wider range to 0.2% below 260 mbsf. The samples from the interval from near the seafloor to 260 mbsf are reported as having no detectable S, yet diagenetic sulfides were commonly reported in some cores from this interval. Time constraints precluded repeat analysis of these samples, so the possibility of an undetected analytical problem cannot be eliminated.

Conclusion

The organic matter in the sediments of the Reference Site is generally immature from the top to ~450 mbsf. This is based on the gas and bitumen compositions. Biogenic methane is present at high concentrations from ~200 to 430 mbsf, and CO_2 is elevated from ~150 to 400 mbsf. Most of the bitumens reflect the immature *n*-alkane signature typical of terrestrial higher plants (C_{max} at C_{29} or C_{31} and CPI >2.5) to 450 mbsf. There are a few horizons with more mature bitu-

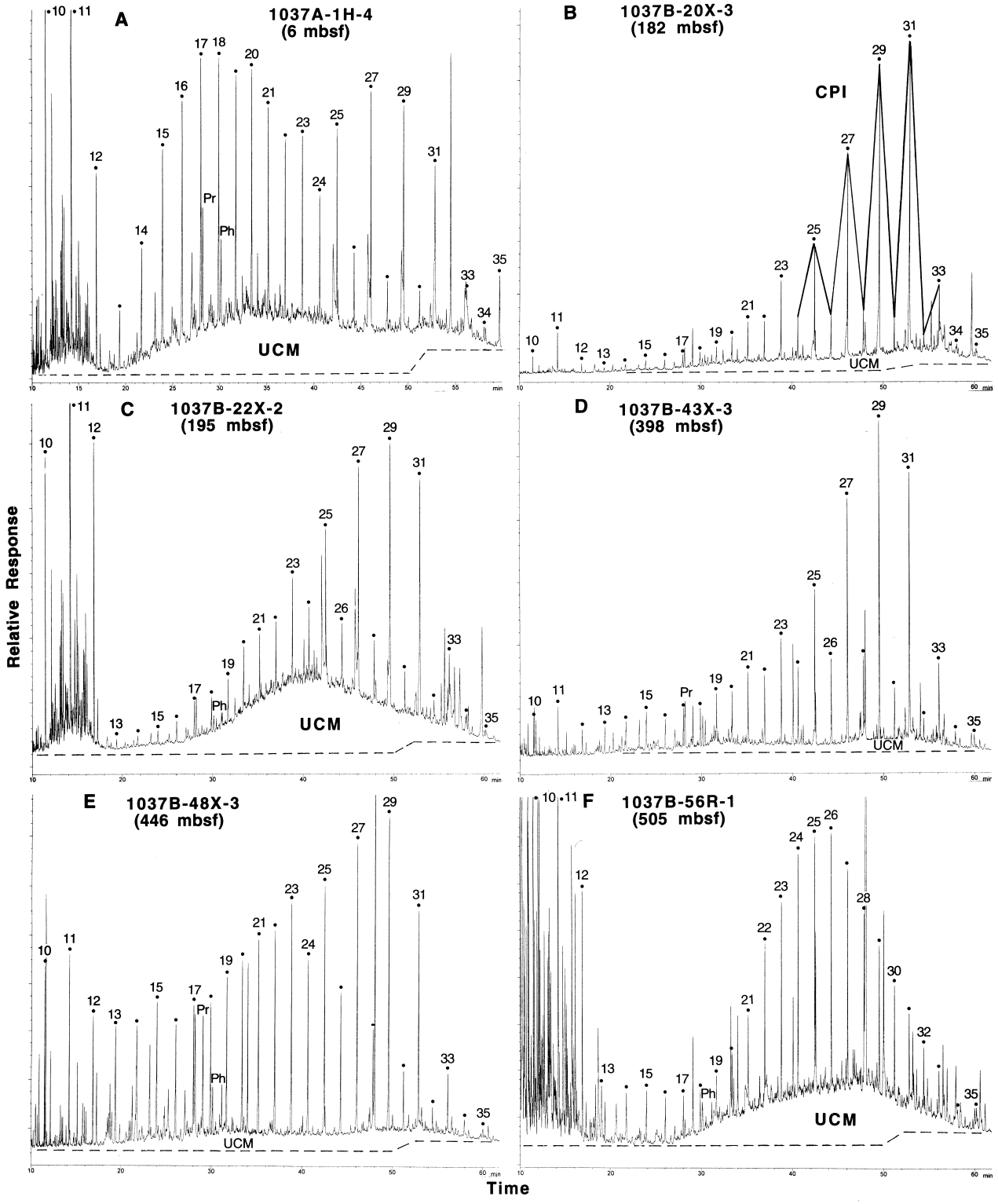

Figure 13. Typical gas chromatograms for total bitumen extracts from sediments of Site 1037. **A.** Section 169-1037A-1H-4 (6 mbsf). **B.** Section 169-1037B-20X-3 (182 mbsf), which shows a high precursor CPI because of an origin from terrigenous plant wax. **C.** Section 169-1037B-22X-2 (195 mbsf). **D.** Section 169-1037B-43X-3 (398 mbsf). **E.** Section 169-1037B-48X-3 (446 mbsf). **F.** Section 169-1037B-56R-1 (505 mbsf). Dots and numbers refer to the carbon chain length of the homologous *n*-alkanes. Pr = pristane, Ph = phytane, and UCM = unresolved complex mixture.

Table 9. Various parameters for the solvent soluble organic matter in sediments from Hole 1037B.

Core, section, interval (cm)	Depth (mbsf)	C_{max}*	C_n range	CPI**	Pr/Ph*
169-1037A-					
1H-4, 140–150	5.95	11, 18, 27	10–35	2.85	1.4
169-1037B-					
1H-5, 15–16	6.15	29	15–35	4.04	2.2
2H-2, 40–41	8.50	29, 27	10–35	4.16	1.8
2H-6, 63–64	14.74	29, 27	10–35	3.66	1.7
3H-4, 140–150	22.05	31	10–35	3.14	2
6H-3, 140–150	49.05	29	10–35	3.93	1.7
7H-3, 120–125	58.33	29	10–35	3.98	2.4
7H-3, 120–125	58.33	31	10–35	2.74	2.3
9H-3, 140–150	77.55	29	10–35	2.76	1.9
13H-2, 140–150	114.05	29, 12	10–35	2.83	1.5
14H-4, 140–150	126.55	29, 31	10–35	3.97	1.8
17X-3, 140–150	153.55	29	10–35	4.52	1.9
20X-3, 140–150	182.05	31, 29	10–35	5.62	2.5
22X-2, 140–150	195.15	11, 29	10–35	3.68	2.4
25X-5, 140–150	228.45	31	10–35	5.08	2.7
30X-3, 140–150	273.45	29	15–35	4.52	2
33X-3, 140–150	302.15	31, 29	10–35	4.53	1.2
35X-3, 140–150	321.35	31	10–35	4.38	1.6
36X-1, 140–150	327.95	31	10–35	4.6	1.8
37X-4, 140–150	342.05	29	10–35	3.5	1.7
40X-3, 140–150	369.45	29	10–35	3.49	1.7
43X-3, 140–150	398.35	29	10–35	3.41	1.5
45X-3, 140–150	417.65	29	10–35	4.57	2
48X-3, 140–150	446.45	29, 11	<10–35	2.25	2.5
50X-3, 140–150	465.75	10, 25	<10–35	0.93	1.1
53X-1, 140–150	491.60	11, 27	<10–35	1.23	1.3
55X-CC, 15–20	501.15	11, 25	<10–35	1.51	1.1
56R-1, 30–37	505.00	11, 26	<10–35	0.89	0.6

Notes: * = major homologs are listed in decreasing order of concentration (C_{max}). ** = carbon preference index calculated from *n*-C_{24} to *n*-C_{33}. Pr = pristane, and Ph = phytane.

men that is interpreted to be derived from recycled older sedimentary detritus carried in by turbidites. The low extract yields throughout the hole indicate that there are no petroleum zones. The elemental compositions of C, N, and S are low and vary from 0.5% to 1.8% for total C, 0% to 1.1% for both total inorganic and organic C, 0% to 0.14% for N, and up to 0.2% for S.

Below 450 mbsf, the organic matter is thermally altered. The gas composition changes in that ethane and higher hydrocarbons appear, with the C_1/C_2 ratio decreasing to <100, thus indicating a thermogenic origin. The low concentrations of bitumens reflect in situ maturation, however, without migration/expulsion. These parameters support the interpretation that the basalt flow encountered at the bottom of the hole shows evidence for a short-lived pulse of high-temperature alteration and fluid flow (see "Igneous Petrology and Geochemistry" section, this chapter) that caused relatively limited thermal alteration of the organic matter in the overlying sediments up to 450 mbsf.

MICROBIOLOGY

Site 1037 in the Escanaba Trough was named the "Reference Site," as it was drilled in an area believed to be removed from hydrothermal influence. Together with the Dead Dog and Bent Hill sites (Sites 1036 and 1035, respectively), Site 1037 completes a small spectrum of varied thermophilic habitats in sediments, both near and far removed from the influence of hydrothermal discharge sites. Basement temperatures at Site 1037 have been estimated at ~80°C (Davis and Becker, 1994), and therefore any microbial communities in the lower sediments must be heat-adapted. A comparison of the microbial abundances and community composition in warm sediments between these three sites will provide important constraints on the controlling factors that influence bacterial abundance in deep ocean sediments.

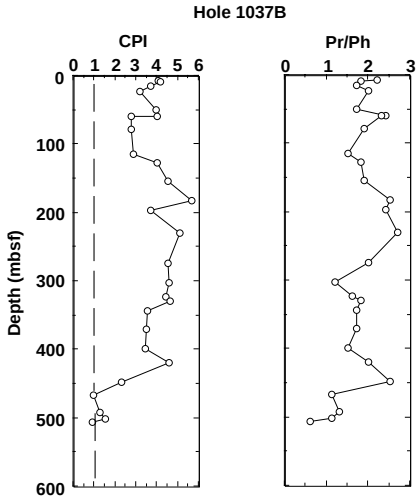

Figure 14. CPI and Pr/Ph depth profiles for sediments from Hole 1037B.

Samples for shore-based epifluorescent microbial counts were taken downhole until the sediment became too lithified to effectively subcore (~400 mbsf). Some samples were taken past this depth by removing whole pieces of lithified sediment, breaking them open, and scraping out the insides using a sterile procedure. Some cores taken with the XCB were heavily biscuited, and care was taken to remove samples from the intact biscuits of sediment and not the surrounding homogenized "muck." No samples were counted from this site during the leg.

Culture work concentrated on the potential for thermophilic and hyperthermophilic microorganisms deep within the section. Four temperature measurements were taken in the upper 83 m of the hole, but as the stability of the hole became precarious, temperature measurements ceased. Based on a constant geothermal gradient estimated from Adara tool measurements, temperatures were estimated at 50°C near 300 mbsf (see "Downhole Measurements" section, this chapter), and enrichment cultures for thermophilic microorganisms were inoculated with seven samples between 321.4 and 472.4 mbsf. As sulfate was fully removed from the pore fluids by 100 mbsf (see "Inorganic Geochemistry" section, this chapter), methanogens were targeted as the most active microbial group. This choice was supported by the methane profile downhole that shows a maximum in biogenic methane between 200 and 350 mbsf (see "Organic Geochemistry" section, this chapter). A rod-shaped organism was cultured from 320 mbsf, and the headspace in the culture tube contained 18 ppm methane; the methane may have been produced by the organism or degassed from the inoculum of sediment. DNA samples were also preserved from three samples from 263, 339, and 435 mbsf to provide a more robust measure of the microbial community diversity in deep-heated sediments.

PHYSICAL PROPERTIES

Physical properties measurements at Site 1037 included index properties, thermal conductivity, and MST logs of magnetic susceptibility, gamma density, *P*-wave velocity, and natural gamma. Multisensor Split Core Logger (MSSCL) measurements of *P*-wave velocity and magnetic susceptibility were also made on selected cores. Index properties measurements are listed in Table 11 and thermal conductivities in Table 12. Figure 16 presents these data together with the major lithologic units (see "Lithostratigraphy and Sedimentology" section, this chapter) for reference. Some variations and trends in porosity appear to correlate with the lithologic units, partic-

Table 10. Weight percentages for Hole 1037B.

Core, section, interval (cm)	Depth (mbsf)	TC (%)	TN (%)	TS (%)	C/N*	C/S*	TIC (%)	TOC (%)
169-1037B-								
1H-1, 52–53	0.52	1.38	0.14	0.16	9.9	8.6	0.24	1.14
1H-5, 15–16	6.15	0.88	0.04	0.06	22	14.7	0.43	0.45
2H-2, 40–41	8.5	0.76	0.02	0	38	—	0.46	0.3
2H-6, 63–64	14.74	0.92	0.04	0	23	—	0.49	0.43
3H-2, 2–3	17.62	0.9	0.03	0	30	—	0.5	0.4
3H-4, 3–4	20.64	0.45	0.01	0	45	—	0.39	0.06
3H-5, 3–4	22.14	0.88	0.05	0	17.6	—	0.35	0.53
4H-3, 63–65	29.24	0.93	0.06	0	15.5	—	0.4	0.53
5H-5, 75–76	41.85	1.08	0.06	0	18	—	0.45	0.63
6H-1, 38–39	44.98	1	0.06	0	16.7	—	0.43	0.57
6H-4, 133–134	50.44	0.49	0.02	0	24.5	—	0.38	0.11
7H-4, 43–44	59.04	0.59	0.02	0	29.5	—	0.42	0.17
8H-4, 63–64	68.74	1.05	0.05	0	21	—	0.52	0.53
9H-3, 42–43	76.52	0.74	0.02	0	37	—	0.46	0.28
10H-2, 92–93	85.02	0.51	0.02	0	25.5	—	0.41	0.1
11H-1, 59–69	92.74	0.37	0.01	0	37	—	0.43	–0.06
12H-4, 70–71	106.8	0.33	0.01	0	33	—	0.27	0.06
13H-2, 40–41	113	0.33	0	0	—	—	0.39	–0.06
14H-3, 60–61	124.2	0.97	0.03	0	32.3	—	0.59	0.38
15H-4, 60–61	135.2	1.04	0.05	0	20.8	—	0.69	0.35
16H-1, 56–57	140.16	0.99	0.07	0	14.1	—	0.38	0.61
16H-1, 67–68	140.25	1.22	0.04	0	30.5	—	0.83	0.39
17H-2, 61–62	151.22	1.12	0.02	0	56	—	0.97	0.15
18H-1, 66–67	159.26	1.39	0.04	0	34.8	—	1.03	0.37
19H-1, 68–69	168.78	0.68	0.01	0	68	—	0.63	0.05
20X-2, 52–53	179.62	1.4	0.05	0	28	—	0.98	0.42
21X-CC, 18–19	192	1.75	0.05	0	35	—	0.87	0.88
22X-1, 93–94	193.14	1.05	0.03	0	35	—	0.88	0.17
23X-3, 100–101	205.8	1.6	0.06	0	26.7	—	1.14	0.46
25X-3, 100–100	225	1.3	0.06	0	21.7	—	0.9	0.4
26X-4, 118–119	236.29	1.33	0.05	0	26.6	—	0.96	0.37
27X-3, 70–71	243.9	1.36	0.06	0	22.7	—	0.95	0.41
28X-2, 41–42	251.72	1.3	0.06	0	21.7	—	0.95	0.35
29X-3, 40–41	262.8	1.37	0.07	0	19.6	—	0.88	0.49
30X-3, 35–36	272.36	1.31	0.05	0.1	26.2	13.1	0.92	0.39
31X-5, 63–64	285.14	1.31	0.06	0.1	21.8	13.1	0.93	0.38
32X-5, 50–51	294.6	1.22	0.03	0.03	40.7	40.7	1.02	0.2
33X-2, 56–57	299.76	1.62	0.06	0	27	—	1.13	0.49
34X-5, 45–46	313.76	1.56	0.09	0.13	17.3	12	0.95	0.61
35X-3, 48–49	320.38	1.71	0.08	0.24	21.4	7.1	1.08	0.63
36X-1, 124–125	326.75	1.71	0.08	0.15	21.4	11.4	1.13	0.58
37X-4, 72–73	341.33	1.02	0.09	0.19	11.3	5.4	0.22	0.8
38X-1, 54–54	346.24	1.2	0.08	0.16	15	7.5	0.7	0.5
39X-4, 46–47	360.37	1.31	0.06	0.12	21.8	10.9	0.79	0.52
40X-5, 14–15	371.15	1.07	0.05	0.1	21.4	10.7	0.74	0.33
41X-CC, 3–4	384.26	0.68	0.02	0.05	34	13.6	0.71	–0.03
42X-2, 72–73	386.53	1.08	0.04	0.09	27	12	0.78	0.3
43X-7,14–15	403.05	1.07	0.03	0.04	35.7	26.8	0.71	0.36
44X-2, 80–81	405.91	0.72	0.02	0	36	—	0.63	0.09
45X-2, 90–92	415.61	1.07	0.04	0	53.5	—	0.81	0.26
46X-2, 56–57	424.87	1.12	0.04	0.06	28	18.7	0.87	0.25
47X-1, 116–117	433.57	1.08	0.02	0.07	54	15.4	0.9	0.18
48X-2, 112–113	444.63	1.08	0.04	0.04	27	27	0.87	0.21
49X-3, 40–42	455.01	1.25	0.05	0.06	25	20.8	0.95	0.3
50X-4, 44–45	466.25	1.11	0.05	0.04	22.2	27.8	0.91	0.2
51X-2, 23–24	472.64	0.93	0.02	0	46.5	—	0.83	0.1
52X-2, 59–60	482.6	0.98	0.04	0.04	24.5	24.5	0.78	0.2
53X-1, 25–26	490.36	0.79	0.05	0.06	15.8	13.2	0.63	0.16
54X-CC, 16–17	499.5	0.87	0.04	0.1	21.8	8.7	0.54	0.33
55X-CC, 3–4	501	1.21	0.06	0.1	20.2	12.1	0.82	0.39
55X-CC, 15–20	501	1.72	0.04	0	43	—	1.3	0.42
56R-1, 20–21	501.4	0.26	0.03	0	8.7	—	0.06	0.2
57R-1, 10–12	507.92	0.05	0.01	0	5	—	0.04	0.01

Notes: * = calculated as percentage ratios. TC = total carbon, TN = total nitrogen, TS = total sulfur, TIC = total inorganic carbon, and TOC = total organic carbon.

ularly the high variability in the Holocene turbidites of Unit II that is associated with multiple graded beds. The increase in porosity with decreasing depth in the Holocene sands of Unit III correlates with a major fining-upward sequence. Overall, there is a general decrease in porosity with depth, from over 70% near the seafloor to ~40% at the base of the late Pleistocene graded siltstones and sandstones of Subunit VIIIB. Porosity decreases abruptly to <10% in the basalts and associated altered sediments below 500 mbsf. Grain density is quite uniform, ~2.8 g/cm^3, throughout the sedimentary section with the exception of Subunit VIIIB, which shows a slight increase and considerable scatter. Grain density of three basalt samples is ~3 g/cm^3.

Wet bulk density follows an opposite trend to that observed for porosity, increasing with depth from ~1.5 g/cm^3 near the seafloor to over 2 g/cm^3 at the base of the sedimentary section and then increasing to ~3 g/cm^3 in the basalt. The excellent agreement between the wet bulk density and the MST confirms the accuracy of the "water calibration" initiated in this hole (Fig. 16). Before sampling, the calibration protocol for the gamma density was changed from the normal aluminum and air standard to an aluminum and water standard. Consequently, there is no need to apply the "water correction" to the data, and the correlation between the gamma density and the measured density is much better.

The thermal conductivity profile shown on Figure 16 is characterized by considerable scatter in the sedimentary units, with values ranging from ~0.9 to 1.6 W/(m·K) and increases to ~2 W/(m·K) in the igneous section.

The MST logs for this reference hole proved particularly useful in facilitating the identification and classification of sedimentary units

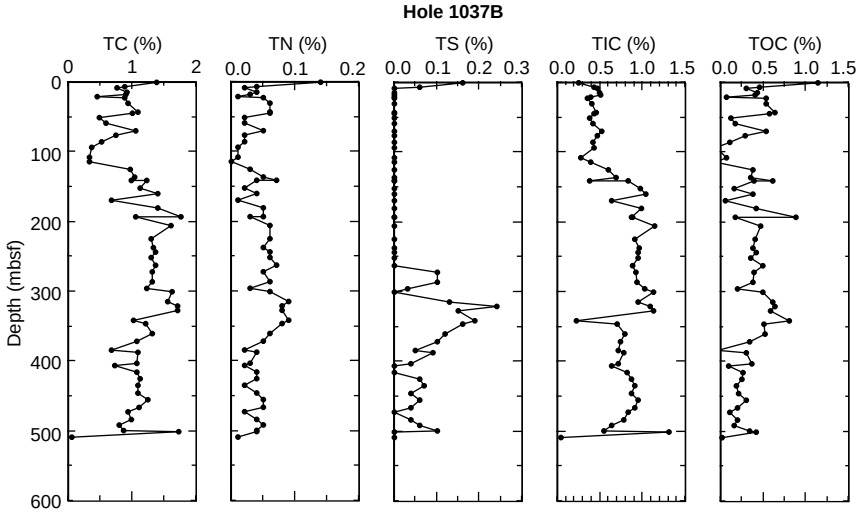

Figure 15. Percentages of TC, TN, TS, TIC, and TOC vs. depth for sediments from Hole 1037B.

(see also "Lithostratigraphy and Sedimentology" section, this chapter). Figure 17 illustrates the strong correlation among all four MST logs in the upper ~180 mbsf of Hole 1037B (note that the sampling frequency for the natural gamma sensor was decreased at 120 mbsf; this accounts for the relative sparseness of natural gamma data in the lower portion of the profile). Dashed lines indicate changes in log signatures, all of which correspond to boundaries of turbidites or hemipelagic units identified on the basis of grain-size distributions.

Below 180 mbsf, *P*-wave velocities were no longer measured with the MST, because of the presence of free gas, but the combination of magnetic susceptibility, gamma density, and natural gamma data continued to provide an excellent tool for stratigraphic analysis. Figure 18 shows these three profiles for the entire cored interval of Hole 1037B, along with dashed lines to indicate boundaries between major sedimentary packages and between the sediment and underlying basalt. At this scale, sedimentary Unit IV and Subunit VIIIB, both consisting of graded beds of silt to fine sand texture, are distinct in their relatively low average magnetic susceptibilities and their relatively high natural gamma counts. The Holocene turbidites of Unit II and the late Pleistocene graded siltstones and sandstones of Subunit VIIIA have distinctive oscillations in both the magnetic susceptibility and gamma density profiles. Similar, but less abundant, oscillations are generated by the thicker, finer grained graded siltstone beds in Unit VI.

P-wave velocity measurements were obtained using the MSSCL below 480 mbsf in the deepest sedimentary Subunit VIIIB, and in the basalts (Fig. 19). Velocities in the sediments have magnitudes of ~2200 m/s, whereas those of the basalts are in the range of 4000 to 5200 m/s.

The magnetic susceptibility records from Unit IV are worth mentioning here because of the difference in character as measured by the point sensor on the MSSCL compared with the loop sensor on the MST. Figure 20 compares magnetic susceptibility records using the two different sensors between 121 and 137 mbsf. This illustrates that some very high magnetic susceptibility peaks (up to ten times higher than the background level) obtained when using the point sensor are barely detected by the loop sensor. Correlation of the peaks to the sediment cores provisionally identifies the peaks as resulting from disseminated, black, acid-volatile iron monosulfide (possibly greigite), which can form authigenically during microbial sulfate reduction. This is an excellent example of how the point sensor responds to disseminated minerals whereas the loop sensor, with its large volume averaging effect, fails to clearly reveal the spatial detail of the magnetic signature.

DOWNHOLE MEASUREMENTS

Operations

The initial logging plan for Hole 1037B included two runs with the Triple Combo tool string and the FMS/sonic combination to characterize the stratigraphic sequence drilled at the Escanaba Trough Reference Site. A wiper trip was done on 1 October after coring operations were completed to clear any potential ledges and to clean 35

Table 11. Index properties, Escanaba Trough Reference Site, Hole 1037B.

Core, section, interval (cm)	Depth (mbsf)	Porosity (%)	Wet bulk density (g/cm^3)	Grain density (g/cm^3)	Wet water content (%)	Void ratio
169-1037B-						
1H-1, 75–77	0.75	83	1.40	2.75	39	4.2
1H-3, 75–77	3.75	73	1.58	2.83	31	2.5
2H-2, 60–62	8.7	52	1.95	2.82	20	1.0
2H-5, 75–77	13.35	67	1.69	2.81	28	1.9
3H-2, 75–77	18.35	50	1.96	2.81	19	1.0
3H-5, 60–62	22.7	63	1.73	2.79	26	1.6
4H-2, 82–84	27.92	63	1.73	2.80	27	1.6
4H-6, 88–90	33.98	47	2.05	2.78	17	0.8
5H-2, 80–82	37.4	60	1.76	2.82	25	1.5
5H-3, 100–102	39.1	56	1.86	2.81	23	1.2
6H-4, 75–77	49.85	50	1.96	2.77	19	1.0
6H-6, 100–102	53.1	63	1.78	2.74	25	1.5
7H-2, 60–62	56.2	52	1.88	2.61	21	1.0

Only part of this table is produced here. The entire table appears on CD-ROM.

Table 12. Thermal conductivity measurements, Escanaba Trough Reference Site, Hole 1037B.

Core	Type	Section	Position (cm)	Depth (mbsf)	Thermal conductivity (W/[m·K])
1	H	2	75	2.25	0.86
1	H	3	75	3.75	0.97
2	H	2	75	8.85	1.30
2	H	5	75	13.35	1.12
3	H	2	75	18.35	0.97
3	H	3	75	19.85	1.24
3	H	4	75	21.35	1.13
3	H	5	60	22.70	1.06
3	H	6	75	24.35	0.98
4	H	2	82	27.92	0.85
4	H	3	80	29.40	1.02
4	H	5	80	32.40	1.01
4	H	6	90	34.00	1.69

Only part of this table is produced here. The entire table appears on CD-ROM.

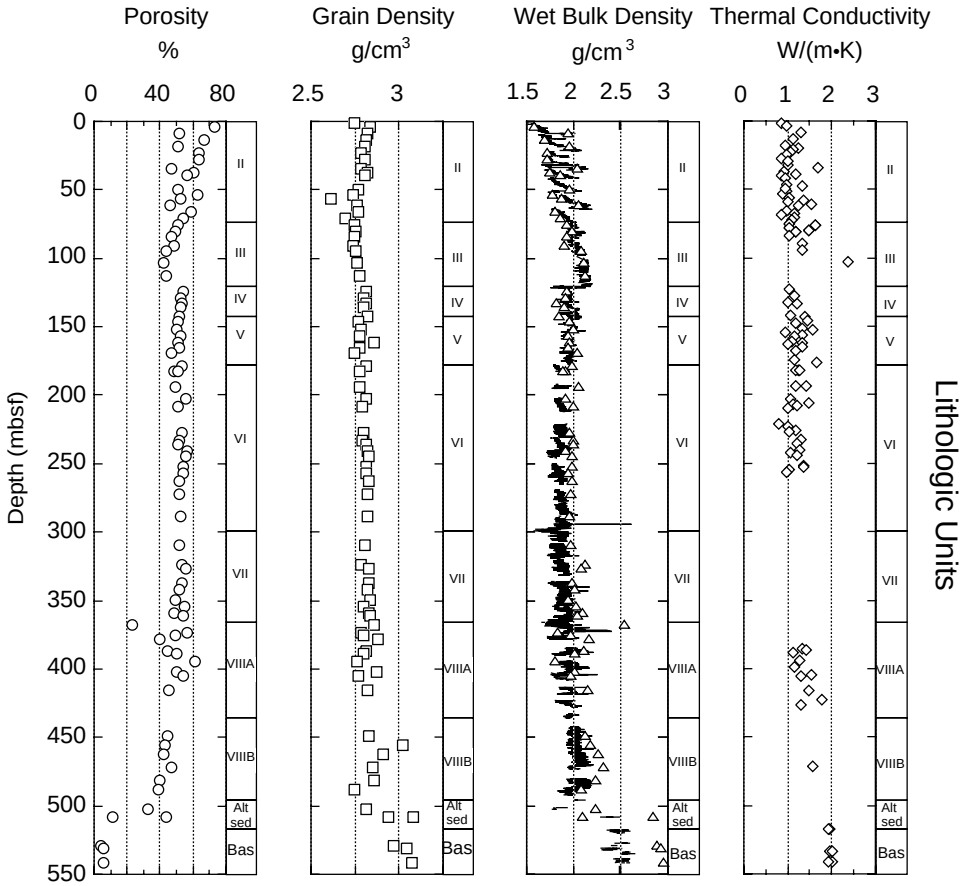

Figure 16. Profiles of index properties and thermal conductivity for Hole 1037B. Circles = porosity values, squares = grain density, triangles = wet bulk density, and diamonds = thermal conductivity. Gamma density measurements obtained from the MST are plotted on the wet bulk density as solid lines. Lithologic unit numbers are shown next to each profile for reference.

m of fill from the bottom of the hole at 546 mbsf. At the conclusion of the hole conditioning process, the RCB bit was dropped at the bottom of the hole, the pipe was set at 100 mbsf, and the Triple Combo was deployed. The relatively deep pipe depth was chosen to prevent any potential problems with presumably unstable shallow sandy units.

The Triple Combo, composed of TLT, DIT, HLDS, APS, and HNGS probes, encountered several difficulties during the run. The DIT failed to transmit any signal shortly after entering the open hole, and several attempts to reestablish communications were not successful. The run was continued to the bottom of the hole without resistivity measurements to collect the other data and eventually determine hole conditions with the caliper from the HLDS. The caliper showed that the hole diameter was larger than the maximum aperture of the FMS (15 in) for most of the hole, and we decided to replace the FMS with a spare DIT for the second run. This decision was based on the fact that the caliper arms of the FMS have a maximum aperture of 15 in, and under these conditions the resistivity data would be more meaningful. A repeat section with the Triple Combo was aborted when the caliper arm apparently failed to close when entering the pipe at 100 mbsf. The second run, composed of SDT, DIT, and gamma-ray (NGT) probes, reached the bottom of the hole at 535 mbsf without any problems.

The quality of the data recorded in this hole varies because of poor hole conditions. The gamma ray and resistivity curves seem to be of good quality because of their deep focus of investigation. The density, porosity, and velocity logs are strongly affected by borehole wall irregularities as shown by the extremely low density and velocity values as well as high porosities throughout most of the hole.

Results

The high recovery in Hole 1037B provided the opportunity to perform accurate core to log correlations and precisely delineate numerous sedimentary sequences identified from core observations. Because of large variations in borehole diameter, the gamma ray and resistivity curves proved most useful in identifying seven main logging units within the Pleistocene stratigraphic sequence (Fig. 21). The main lithologic units (see “Lithostratigraphy and Sedimentology” section, this chapter) are recognizable on both the gamma-ray and resistivity curves, but stratigraphic boundaries do not precisely coincide with all the logging unit boundaries. Descriptions of logging units and correlations with lithostratigraphy are discussed below.

Logging Unit 1 (102–121.90 mbsf)

Only the lowermost 20 m in lithologic Unit III were logged because of the position of the pipe near the bottom of the unit (Fig. 21A). Low gamma-ray counts and higher resistivities clearly reflect the sandy nature of the base of this unit. The contact between logging Units 1 and 2 correlates well with the boundary between lithologic units III and IV and can be clearly identified by an increase in gamma-ray counts and a decrease in resistivity, indicating a sharp transition into a more clay-rich formation.

Logging Unit 2 (121.90 –153.90 mbsf)

The second logging unit is more complex, and its base (153.90 mbsf) does not coincide with the bottom of lithologic Unit IV (142.85

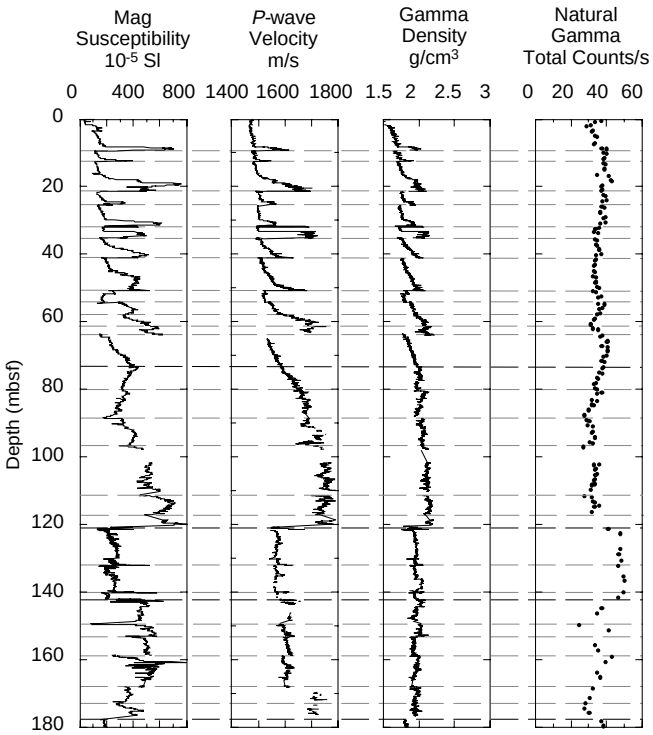

Figure 17. Profiles of MST measurements of magnetic susceptibility, *P*-wave velocity, gamma density, and natural gamma for the upper 180 mbsf of Hole 1037B. Dashed lines indicate depths of significant changes in log signatures. Heavier dashed lines correspond to boundaries of lithologic units described in the "Lithostratigraphy and Sedimentology" section (this chapter).

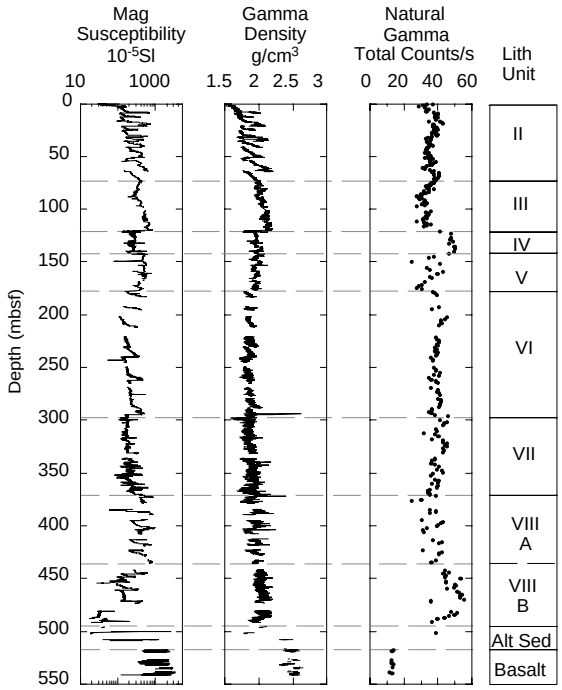

Figure 18. Profiles of MST measurements of magnetic susceptibility, gamma density, and natural gamma for the entire cored interval of Hole 1037B. Lithologic units are shown for reference, with dashed lines through the profiles corresponding to the boundaries between these units.

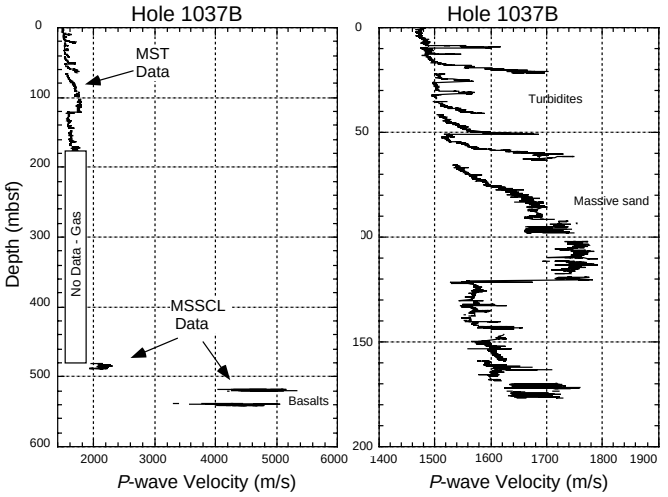

Figure 19. *P*-wave velocity data for Hole 1037B obtained from both the MST and MSSCL. The presence of free gas in the recovered cores prevented data from being obtained from much of the hole. The plot on the right, an expanded section of the data from 0 to 200 mbsf, shows the velocity variations within the turbidite sequences and the higher velocities of the massive sand units.

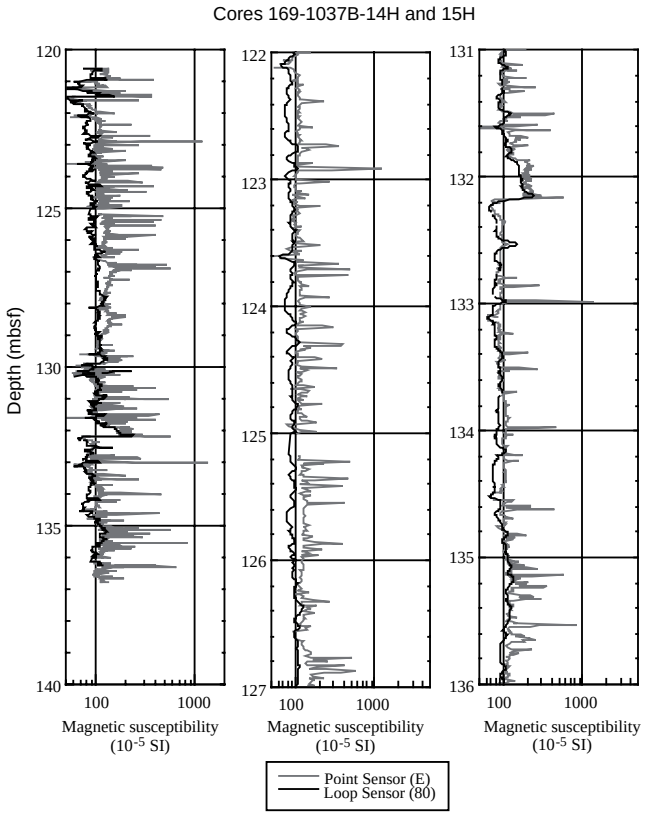

Figure 20. Magnetic susceptibility profiles for Hole 1037B. Cores 169-1037B-14H and 15H, show how the point sensor reveals disseminated minerals that are barely detected by the loop sensor.

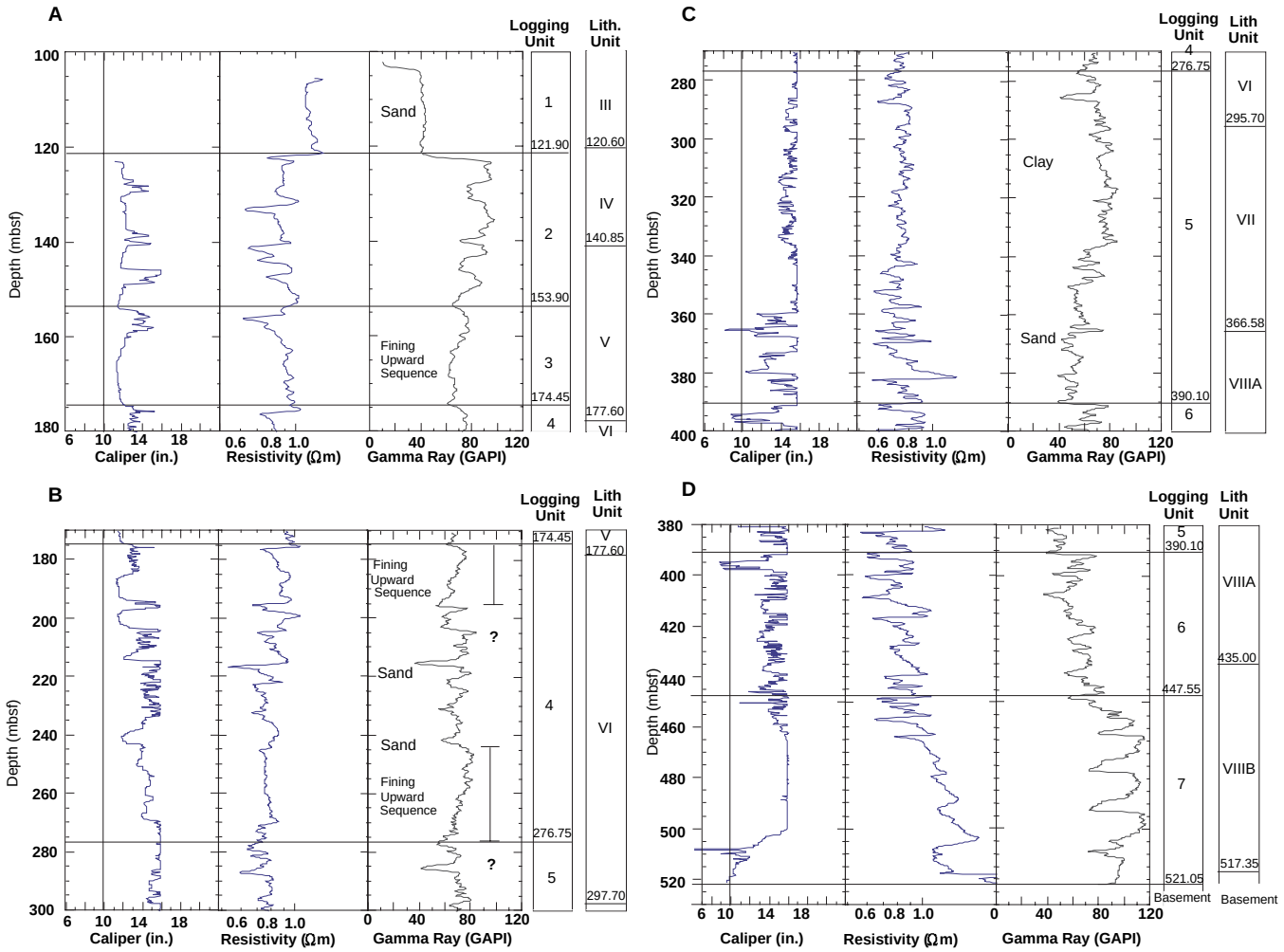

Figure 21. Caliper, resistivity, and gamma-ray downhole measurements recorded in sections of Hole 1037B from (**A**) 100 to 180 mbsf, (**B**) 170 to 300 mbsf, (**C**) 270 to 400 mbsf, and (**D**) 380 to 530 mbsf. Logging units and their respective depths as well as stratigraphic units and features identified from logs and recovered cores are also shown. Dashed line in the caliper plot represents 9.875-in bit size used during coring operations. Question marks represent discrepancies between core and log observations owing to poor recovery and hole conditions.

mbsf). The logging unit is characterized by gamma-ray and resistivity curves suggesting a series of alternating clay and muddy sand beds (Fig. 21A). Four intervals interpreted as muddy sands range in thickness from ~2 to 5 m, whereas the thickness of the clay-rich units ranges from 2 to 6 m.

Logging Unit 3 (153.90 –174.45 mbsf)

This unit is defined by a ~20-m-thick fining-upward sequence. A reduction in gamma ray and an increase in resistivity is consistent with an increase in sand content down to the contact with logging Unit 4, which coincides with the top of lithologic Unit VI (Fig. 21B).

Logging Unit 4 (174.45 –276.75 mbsf)

The top and bottom of this logging unit are defined by log responses indicative of fining-upward sequences (Fig. 21B), with the base ~20 m shallower than the base of lithologic Unit VI (297.70 mbsf). Most of this logging unit is interpreted to be clay-rich beds with some minor but distinctive low gamma-ray layers that correlate well with sandy units recovered from the main section of lithologic Unit VI. An exception is the log section denoted with a question mark on Figure 21B at ~203 mbsf. The transition from what is interpreted as a sandy layer to a more clay-rich zone at this depth was not documented in core observations. Possible explanations for the uncertainty include the lack of recovery in this particular interval and the location of this logging unit within an irregularly shaped section of the borehole.

Logging Unit 5 (276.75 –390.10 mbsf)

The top of this unit is marked by the base of a fining-upward sequence ~20 m shallower than the top of lithologic Unit VII. The upper section of this logging unit corresponds to a 60-m-thick, predominantly clay-rich section, whereas the bottommost 52 m show low gamma-ray counts indicative of a sand-rich section (Fig. 21B, C). The section marked by a question mark in Figure 21B (~285 mbsf) represents a discrepancy between core observations and the logging data. Unlike in the previous logging unit, the section in question shows low gamma-ray and resistivity readings that may be caused by large variations in the borehole diameter.

Logging Unit 6 (390.10 –447.55 mbsf)

The top and bottom of this logging unit are interpreted to be comprised mostly of clay-rich beds interbedded with thinner sandy units, and the bottom correlates well with the top of lithologic Subunit VIIIA. The contact with logging Unit 5 is marked by a sharp transi-

tion shown by an increase in gamma-ray counts and a decrease in resistivity interpreted to reflect a more clay-rich zone (Fig. 21C, D).

Logging Unit 7 (447.55 –521.05 mbsf)

This logging unit is characterized by a gradual increase in resistivity and higher gamma-ray readings than the values observed for logging Unit 6. The logging unit correlates with lithologic Subunit VIIIB and suggests that this poorly recovered interval is composed of well-defined sand and clay-rich beds. The gradual increase in resistivity may indicate an increase in calcareous cementation and induration of the rocks recovered from this section (see "Lithostratigraphy and Sedimentology" section, this chapter). The bottom of this unit is marked by a high resistivity jump at 518 mbsf that correlates with the top of the igneous basement observed in the cores.

Porosity, density, and velocity logs for the most part show the effects of the large diameter of the borehole (Fig. 22). The lowest recorded porosities and the highest densities correlate well with physical properties measurements. However, it is difficult to detect any particular trends from these logs except over a 40-m section between 240 and 280 mbsf and in the bottommost section of the hole. The upper 40-m interval corresponds to a smaller diameter section of the hole within a fining-upward sequence in logging Unit 4 (Fig. 21B), whereas the lowermost 70-m interval has lower porosities (~35%) and higher densities (~2.15 g/cm^3) which may reflect increases in the degree of induration and the increase in carbonate cementation. Sonic velocity values above 2000 m/s at 400 mbsf may also indicate an increase in induration with depth (Fig. 22).

The most significant variations in potassium, uranium, and thorium values are in logging Units 2, 5, 6, and 7 (Fig. 23). Increases in all three elements in logging Unit 2 are most likely caused by the high clay content in this interval (see "Lithostratigraphy and Sedimentology" section, this chapter). The variations in logging Unit 5 can also be correlated to the clay composition of the upper part of the section and the sandier nature of the bottom of this interval. Lower density and higher porosity trends corresponding to the sandy portion of the interval covered by logging Unit 5 are observed in the noisy porosity and density logs, suggesting that this interval is less indurated. There is a gradual increase in K, U, and Th starting at the top of logging Unit 6, with the most significant increase occurring at the top of logging Unit 7. The sharp increase in all three radioactive elements correlates with increases in potassium, strontium, rubidium, and lithium contents of the pore waters (see "Inorganic Geochemistry" section, this chapter), and may indicate fluid flow from the potassium-rich basaltic basement (see "Igneous Petrology and Geochemistry" section, this chapter).

Temperature Measurements

Borehole temperatures were measured with the LDEO temperature tool (TLT) at the bottom of the Triple Combo tool string (see "Explanatory Notes" chapter, this volume). Both downgoing and upgoing borehole temperature profiles were recorded during this run (Fig. 24). A difference of 10°C between the profiles at the bottom may represent the extent of thermal rebound at this time in the operations, but could also be attributed to the removal of cold mud accumulated around the sensor on the way down. The downgoing profile also shows several sharp variations in temperature as ledges were encountered at the bottom of the hole. These variations may represent frictional heating as the probe penetrated muddy formation or the removal of mud accumulated on the way down. However, neither of these two profiles can be considered representative of the actual borehole temperature distribution because of the long-lasting effects caused by drilling disturbances. The temperature difference between the profiles at 100 mbsf is ~3°C.

The deployment of the Adara tool (see "Explanatory Notes" chapter, this volume) provided an insight into the subsurface temperature distribution within the reference site area of the Escanaba Trough. A total of four formation temperature measurements were taken with this tool at the top of the hole during coring operations (Fig. 25). Borehole instabilities, however, precluded the use of this tool beyond 85.5 mbsf. Analysis and interpretation of the temperature records included fitting the data to theoretical decay curves and produced the extrapolated formation temperatures summarized in Table 13 and Figure 26. A bottom-water value of 1.73°C was obtained from mudline equilibrium temperature measurements with the Davis-Villinger temperature probe tool in Hole 1038I and was used for calculations of a linear thermal gradient that gives a temperature of ~87°C at the bottom of the hole. This value is consistent with temperature projections for the sediment/basalt interface previously calculated from surface heat flow (Davis and Becker, 1994).

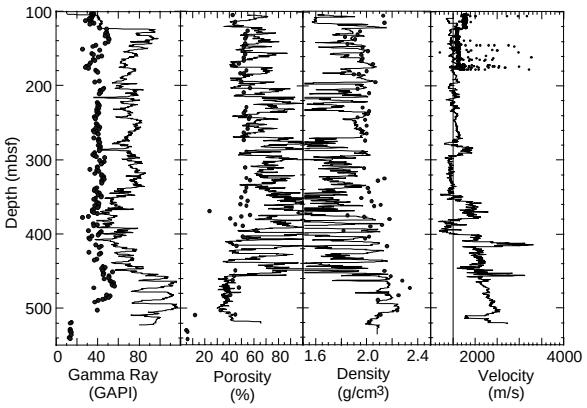

Figure 22. Comparison of downhole measurements and physical properties data (solid circles). Gamma-ray data used for correlation were obtained from the MST, the density and porosity data from index properties measurements on discrete samples, and the velocity data from the MSSCL. The line on the velocity profile denotes the approximate velocity of seawater.

PALEOMAGNETISM

Paleomagnetic measurements were made for the purpose of constructing a magnetostratigraphy at Site 1037, a lithologic reference hole drilled away from areas of known hydrothermal alteration in the Escanaba Trough. Where recovery permitted, whole sections of split core from Hole 1037B were measured and demagnetized in the pass-

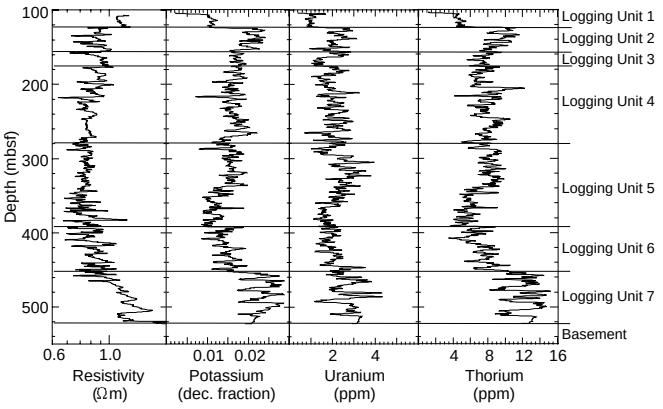

Figure 23. Downhole measurements of variations in relative abundances of radioactive elements K, U, and Th. The resistivity curve and depths of logging units are also shown for correlation purposes.

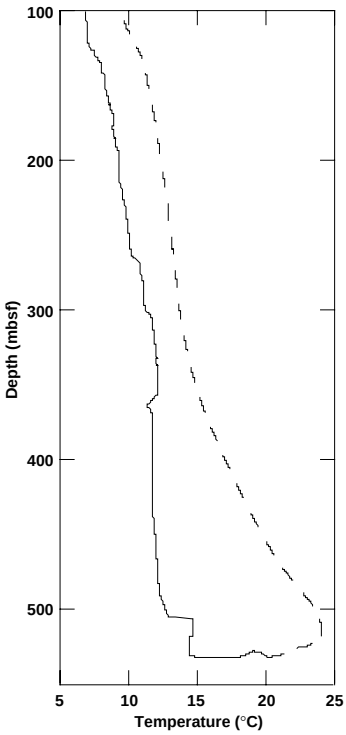

Figure 24. Borehole temperatures recorded with the TLT, ~6 hr after coring operations were completed. The solid line represents the downhole profile obtained during lowering of the tool, and the dashed line represents the profile obtained during raising of the tool.

through magnetometer over the intervals 0–85, 120–165, 175–240, and 440–460 mbsf as well as several short intervals near the bottom of the cored interval at 520–540 mbsf. Lithologic units used herein refer to those defined in the "Lithostratigraphy and Sedimentology" section (this chapter).

Hole 1037B

A magnetostratigraphy for the lithologic reference section at Site 1037 is hindered by a combination of discontinuous turbiditic sedimentation and the strong drilling-induced disturbance throughout long intervals of the profile. Polarities derived from the 20-mT demagnetization are positive throughout the sediment section and thus suggest magnetization during the Brunhes Chron (C1n). Moreover, the downhole variation of both the intensities of natural remanent magnetization (NRM) and the inclination appear to be a function of sedimentary structure and composition (Fig. 27; see "Lithostratigraphy and Sedimentology" section, this chapter). Magnetization intensities are on the order of 0.1 A/m with only minor, although abrupt and distinct, variations throughout lithologic Units I–VIII. Such changes in magnetization intensities and inclinations can be correlated to individual turbidite sequences described in the different lithologic units. The presence of a thick discontinuously sedimented Holocene interval, possibly extending to 120 mbsf and a (late?) Pleistocene interval in the remainder of the hole, which is equally characterized by turbiditic sedimentation (see "Lithostratigraphy and Sedimentology" and "Biostratigraphy" sections, this chapter), suggests potentially significant stratigraphic gaps at Site 1037. This possibly accounts for a lack of recorded short-term polarity events in cores from Hole 1037B, and, therefore, the failure to delineate polarity zones. Apart from magnetostratigraphy, the magnetic signal still provides a valuable opportunity to determine the downhole characteristics of the sediments recovered at Site 1037. The abrupt changes in both intensities and inclination match, and thus confirm, the preliminary shipboard lithologic units and support the interpretation that the unit boundaries separate intervals of distinctly different characteristics, including differences in the magnetic signal. First-order variations in magnetic susceptibility parallel those recorded for the remanence intensities (Fig. 27, see "Physical Properties" and "Lithostratigraphy and Sedimentology" sections, this chapter). This indicates that magnetic susceptibility, on this first-order scale, is largely driven by concentration variations of the remanent magnetic component of the sediment. It may well correspond to a primary detrital input of magnetic minerals that would be associated with changes of the overall mineralogy. Unusually shallow inclinations in several intervals of Unit II (e.g., 1.6–16 mbsf) and throughout lithologic Unit IV (Fig. 27) are correlative with individual turbidites and thus possibly a result of the mass deposition process. In the basalts recovered from the base of Hole 1037B, magnetization intensities reach 4 A/m. Two short meter-scale swings to negative inclination may well represent true records of the Earth's magnetic field (these swings are confirmed by a concomitant relative change in declination). Although the data are available, a match to the polarity time scale is impossible at this stage.

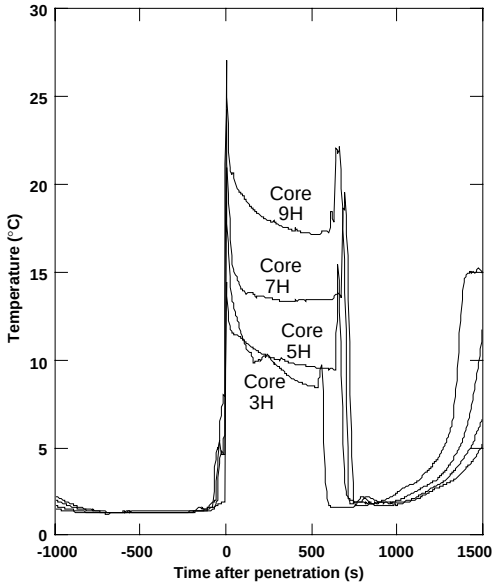

Figure 25. Formation temperature records obtained with the Adara tool in Hole 1037B of the Escanaba Trough Reference Site area. Extrapolated equilibrium temperatures (Table 13) were obtained by applying a theoretical decay curve fit to the portions of the temperature-time records corresponding to the time spent by the probes in the sediment. Temperatures of ~87°C were calculated at the bottom of the hole, assuming a linear gradient tied to a bottom water temperature of 1.73°C.

Table 13. Summary of formation temperature measurements, Hole 1037B, Escanaba Trough Reference Site area.

Depth (mbsf)	Temperature (°C)	Gradient (°C/m)
25.6	5.9	0.16
47.5	7.8	0.18
66.5	13.2	0.28
85.5	15.2	0.11

Note: The temperature measurements were made with the Adara probe in the upper 90 m of the hole.

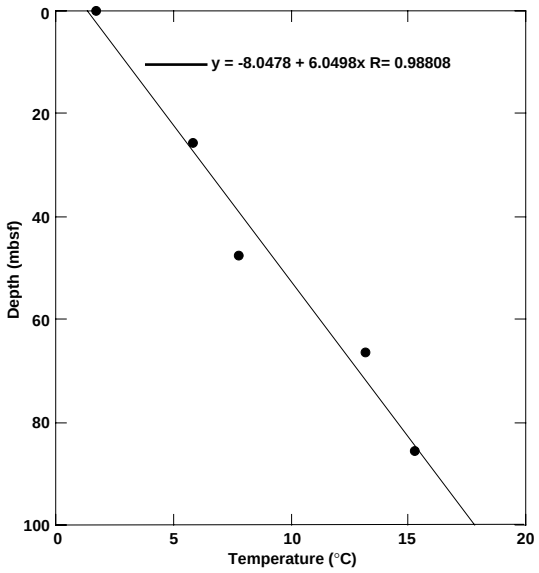

Figure 26. Temperature vs. depth profile for temperatures measured with the Adara tool. A bottom-water temperature of 1.73°C was assumed to calculate a linear fit through the data points.

Conclusions

Inclinations of the NRM suggest a magnetization during Chron C1n. A more precise dating of the sediments based on magnetic events during the Pleistocene is prohibited, because of the discontinuous sedimentation at Hole 1037A and the strong drilling disturbance of the cores recovered, thus rendering the measurement of large amounts of core less productive. A high-resolution environmental magnetic study on the upper part of Unit II (to be conducted onshore) will address a suite of sediment genetic aspects at Site 1037 and thus aid in the determination of primary detrital vs. diagenetic characteristics and in the interpretation of the sedimentary reference section.

REFERENCES

Alt, J.C., Laverne, C., Vanko, D.A., Tartarotti, P., Teagle, D.A.H., Bach, W., Zuleger, E., Erzinger, J., Honnorez, J., Pezard, P.A., Becker, K., Salisbury, M.H., and Wilkens, R.H., 1996. Hydrothermal alteration of a section of upper oceanic crust in the eastern equatorial Pacific: a synthesis of results from Site 504 (DSDP Legs 69, 70, and 83, and ODP Legs 111, 137, 140, and 148.) In Alt, J.C., Kinoshita, H., Stokking, L.B., and Michael, P.J. (Eds.), Proc. ODP, Sci. Results, 148: College Station, TX (Ocean Drilling Program), 417–434.

Bernard, B.B., Brooks, J.M., and Sackett, W.M., 1976. Natural gas seepage in the Gulf of Mexico. *Earth Planet. Sci. Lett.*, 31:48–54.

Chan, L.H., Gieskes, J.M., You, C.F. and Edmond, J.M., 1994. Lithium isotope geochemistry of sediments and hydrothermal fluids of the Guaymas Basin, Gulf of California, *Geochim. Cosmochim. Acta*, 58:4443–4454.

Davis, A.S., and Clague, D.A., 1987. Geochemistry, mineralogy, and petrogenesis of basalt from the Gorda Ridge. *J. Geophys. Res.*, 92:10,467–10,483.

Davis, A.S., Clague, D.A., and Freisen, W.B., 1994. Petrology and mineral chemistry of basalts from Escanaba Trough. *In* Morton, J.L., Zierenberg, R.A., and Reiss, C.A. (Eds.), *Geologic, Hydrothermal, and Biologic Studies at Escanaba Trough, Gorda Ridge, Offshore Northern California.* U.S. Geol. Surv. Bull., 2022:153–170.

Davis, E.E., and Becker, K., 1994. Thermal and tectonic structure of the Escanaba Trough: new heat-flow measurements and seismic-reflection profiles. *In* Moreton, J., Zierenberg, R.A., and Reiss, C.A. (Eds.), *Geologic, Hydrothermal, and Biologic Studies at Escanaba Trough, Gorda Ridge, Offshore Northern California.* U.S. Geol. Surv. Bull., 2022:45–64.

Didyk, B.M., Simoneit, B.R.T., Brassell, S.C., and Eglinton, G., 1978. Organic geochemical indicators of palaeoenvironmental conditions of sedimentation. *Nature*, 272:216–222.

Gieskes, J.M., 1975. Chemistry of interstitial waters of marine sediments. *Annu. Rev. Earth Planet. Sci.*, 3:433–453.

Gieskes, J.M., Gamo, T., and Brumsack, H., 1991. Chemical methods for interstitial water analysis aboard *JOIDES Resolution. ODP Tech. Note*, 15.

Grimalt, J., and Albaiges, J., 1987. Sources and occurrence of C_{12}-C_{22} *n*-alkane distributions with even carbon-number preference in sedimentary environments. *Geochim. Cosmochim. Acta*, 51:1379–1384.

Hunt, J.M., 1996. *Petroleum Geochemistry and Geology* (2nd. ed): New York (W.H. Freeman and Company).

Kastner, M., 1976. Diagenesis of basal sediments and basalts of Sites 322 and 323, Leg 35, Bellingshausen Abyssal Plain. *In* Hollister C.D., Craddock, C., et al., *Init. Repts. DSDP*, 35: Washington (U.S. Govt. Printing Office), 513–527.

Kastner, M., and Gieskes, J.M., 1976. Interstitial water profiles and sites of diagenetic reactions, Leg 35, DSDP, Bellingshausen Abyssal Plain. *Earth Planet. Sci. Lett.*, 33:11–20.

Kvenvolden, K.A., Rapp, J.B., and Hostettler, F.D., 1994. Hydrocarbons in sediment from Escanaba Trough. *In* Morton, J.L., Zierenberg, R.A., and Reiss, C.A. (Eds.), *Geologic, Hydrothermal, and Biologic Studies at Escanaba Trough, Gorda Ridge, Offshore Northern California*, U.S. Geol. Surv. Bull., 2022:279–292.

Kvenvolden, K.A., and Simoneit, B.R.T., 1990. Hydrothermally derived petroleum: examples from Guaymas Basin, Gulf of California and Escanaba Trough, Northeast Pacific Ocean. *AAPG Bull.*, 74:223–237.

Martin, J.B., 1994. Diagenesis and hydrology at the New Hebrides Forearc and intra-arc Aoba Basin. *In* Greene, H.G., Collot, J.-Y., Stokking, L.B., et al., *Proc. ODP, Sci. Results*, 134: College Station, TX (Ocean Drilling Program), 109–130.

Meschede, M., 1986. A method of discriminating between different types of mid-oceanic ridge basalts and continental tholeiites with the Nb-Zr-Y diagram. *Chem. Geol.*, 56:207–218.

Morton, J.L., and Fox, C.G., 1994. Structural setting and interaction of volcanism and sedimentation at Escanaba Trough: geophysical results. *In* Morton, J.L., Zierenberg, R.A., and Reiss, C.A. (Eds.), *Geologic, Hydrothermal, and Biologic Studies at Escanaba Trough, Gorda Ridge, Offshore Northern California.* U.S. Geol. Surv. Bull., 2022:21–43.

Normark, W.R., Gutmacher, C.E., Zierenberg, R.A., Wong, F.L., and Rosenbauer, R.J., 1994. Sediment fill of Escanaba Trough. *In* Morton, J.L., Zierenberg, R.A., and Reiss, C.A. (Eds.), *Geologic, Hydrothermal, and Biologic Studies at Escanaba Trough, Gorda Ridge, Offshore Northern California.* U.S. Geol. Surv. Bull., 2022:91–130.

Shipboard Scientific Party, 1992. Site 858. *In* Davis, E.E., Mottl, M.J., Fisher, A.T., et al., *Proc. ODP, Init. Repts.*, 139: College Station, TX (Ocean Drilling Program), 431–569.

Simoneit, B.R.T., 1977. Diterpenoid compounds and other lipids in deep-sea sediments and their geochemical significance. *Geochim. Cosmochim. Acta*, 41:463–476.

————, 1978. The organic chemistry of marine sediments. *In* Riley, J.P., and Chester, R. (Eds.), *Chemical Oceanography* (2nd ed.) (Vol. 7): New York (Academic Press), 233–311.

————, 1994. Lipid/bitumen maturation by hydrothermal activity in sediments of Middle Valley, Leg 139. *In* Mottl, M.J., Davis, E.E., Fisher, A.T., and Slack, J.F. (Eds.), *Proc. ODP, Sci. Results*, 139: College Station, TX (Ocean Drilling Program), 447–465.

Simoneit, B.R.T., Brenner, S., Peters, K.E., and Kaplan, I.R., 1981. Thermal alteration of Cretaceous black shale by basaltic intrusions in the eastern Atlantic. II: Effects on bitumen and kerogen. *Geochim. Cosmochim. Acta*, 45:1581–1602.

Simoneit, B.R.T., Goodfellow, W.D., and Franklin, J.M., 1992. Hydrothermal petroleum at the seafloor and organic matter alteration in sediments of Middle Valley, northern Juan de Fuca Ridge. *Appl. Geochem.*, 7:257–264.

Simoneit, B.R.T., Kawka, O.E., and Brault, M., 1988 Origin of gases and condensates in the Guaymas Basin hydrothermal system (Gulf of California). *Chem. Geol.*, 71:169–182.

Simoneit, B.R.T., Prahl, F.G., Leif, R.N., and Mao, S.-Z., 1994. Alkenones in sediments of Middle Valley, Leg 139: application as thermal sensors. *In* Mottl, M.J., Davis, E.E., Fisher, A.T., and Slack, J.F. (Eds.), *Proc. ODP, Sci. Results*, 139: College Station, TX (Ocean Drilling Program), 479–484.

Tissot, B.P., and Welte, D.H., 1984. *Petroleum Formation and Occurrence* (2nd ed.): Heidelberg (Springer-Verlag).

Vallier, T.L., 1970. The mineralogy of some turbidite sands from Sites 32 and 35. *In* McManus, D.A., Burns, R.E., et al., *Init. Repts. DSDP*, 5: Washington (U.S. Govt. Printing Office), 535–539.

Vallier, T.L., Harold, P.J., and Girdley, W.A., 1973. Provenances and dispersal patterns of turbidite sand in Escanaba Trough, northeastern Pacific Ocean. *Mar. Geol.*, 1:67–87.

Zierenberg, R.A., Morton, J.C., Koski, R.A., and Ross, S.L., 1994. Geologic setting of massive sulfide mineralization in Escanaba Trough. *In* Morton, J.L., Zierenberg, R.A., and Reiss, C.A. (Eds.), *Geologic, Hydrothermal, and Biologic Studies at Escanaba Trough, Gorda Ridge, Offshore Northern California*. U.S. Geol. Surv. Bull., 2022:171–197.

Zuffa, G.G., De Rosa, R., and Normark, W.R., in press. Shifting sources and transport paths for the Late Quaternary Escanaba Trough sediment fill (Northeast Pacific). *Gior. Geol*.

Ms 169IR-105

NOTE: For all sites drilled, core-description forms ("barrel sheets") and core photographs can be found in Section 3, beginning on page 299. Smear-slide data and thin-section data can be found on CD-ROM. See Table of Contents for material contained on CD-ROM.

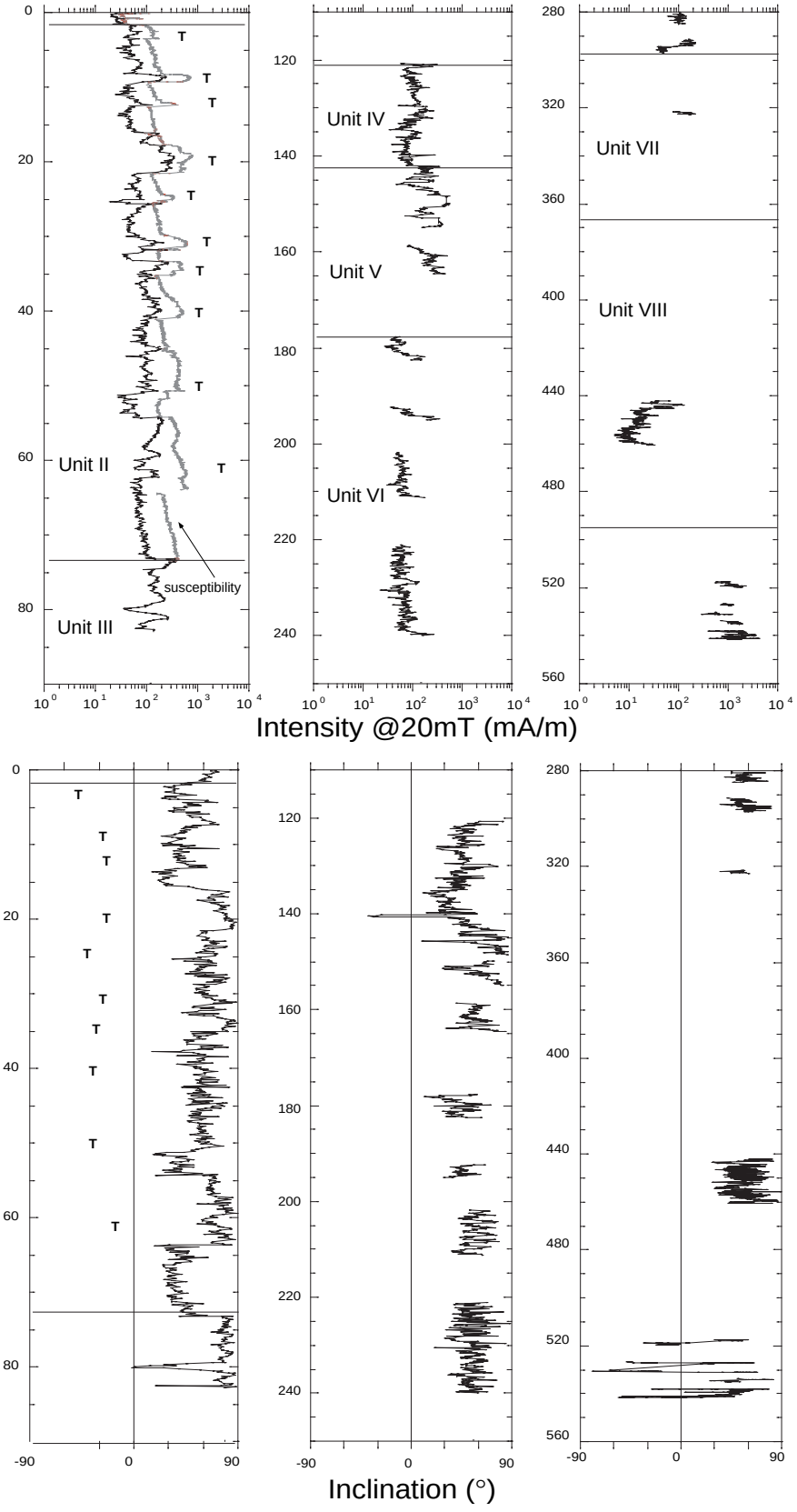

Figure 27. Intensities after demagnetization at 20 mT and inclination of the NRM in Hole 1037B. Stippled horizontal lines indicate lithologic unit (Units II–VIII) boundaries (see "Lithostratigraphy and Sedimentology" section, this chapter). Bold printed T's represent the base of individual turbidites that characterize lithologic Unit II. Gray curve plotted beside Unit II intensities represents downhole trends in raw susceptibility (cf. "Physical Properties" and "Lithostratigraphy and Sedimentology" sections, this chapter). See text for explanation. Note differences in depth scale.

SHORE-BASED LOG PROCESSING

Hole 1037B

Bottom felt: 3311.9 mbrf
Total penetration: 546.0 mbsf
Total core recovered: 426.95 m (78.2%)

Logging Runs

Logging string 1: DIT/APS/HLDS/HNGS
Logging string 2: DIT/SDT/NGT

Because of technical problems, we initially decided not to use the wireline heave compensator. However, the WHC was used intermittently during logging operations. Ship heave was very mild. Because of a communication failure, no DIT data was recorded with the DIT/APS/HLDS/HNGS tool string.

Bottom-Hole Assembly

The following bottom-hole assembly depths are as they appear on the logs after differential depth shift (see "Depth shift" section) and depth shift to the seafloor. As such, there might be a discrepancy with the original depths given by the drillers on board. Possible reasons for depth discrepancies are ship heave, use of the wireline heave compensator, and drill string and/or wireline stretch.

DIT/APS/HLDS/HNGS: Bottom-hole assembly at ~103 mbsf
DIT/SDT/NGT: Bottom-hole assembly at ~103 mbsf

Processing

Depth shift: Original logs have been interactively depth shifted with reference to NGT from DIT/APS/HLDS/HNGS run and to the seafloor (–3310 m). This value corresponds to the seafloor depth as seen on the logs and differs 4 m from the drillers' "bottom felt" depth (3314 mbrf).

Gamma-ray processing: NGT data have been processed to correct for borehole size and type of drilling fluid. HNGS data are corrected in real time during the recording.

Acoustic data processing: The array sonic tool was operated in standard depth-derived borehole compensated mode, including long-spacing (8-10-10-12 ft) and short-spacing (3-5-5-7 ft) logs. The long-spacing sonic logs have been processed to eliminate some of the noise and cycle skipping experienced during the recording.

Quality Control

Data recorded through bottom-hole assembly should be used qualitatively only because of the attenuation on the incoming signal. Invalid gamma-ray data were recorded by the NGT tool from 100 to 103 mbsf.

Hole diameter was recorded by the hydraulic caliper on the HLDS tool (LCAL). The density data were badly affected by the caliper malfunction during the recording.

Details of standard shore-based processing procedures are found in the "Explanatory Notes" chapter (this volume). For further information about the logs, please contact:

Cristina Broglia
Phone: 914-365-8343
Fax: 914-365-3182
E-mail: chris@ldeo.columbia.edu

Hole 1037B: Natural Gamma Ray-Resistivity-Sonic Logging Data

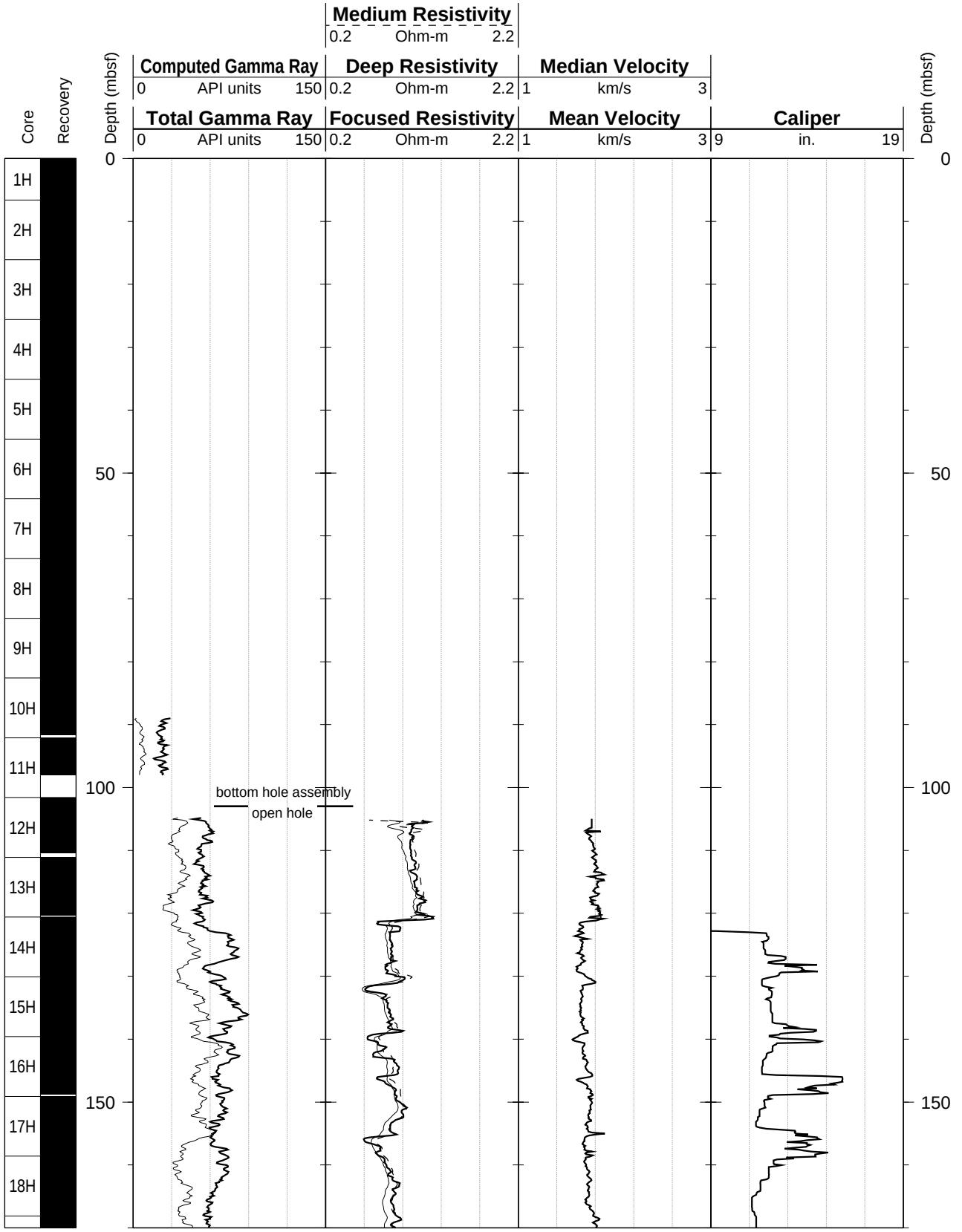

Hole 1037B: Natural Gamma Ray-Resistivity-Sonic Logging Data (cont.)

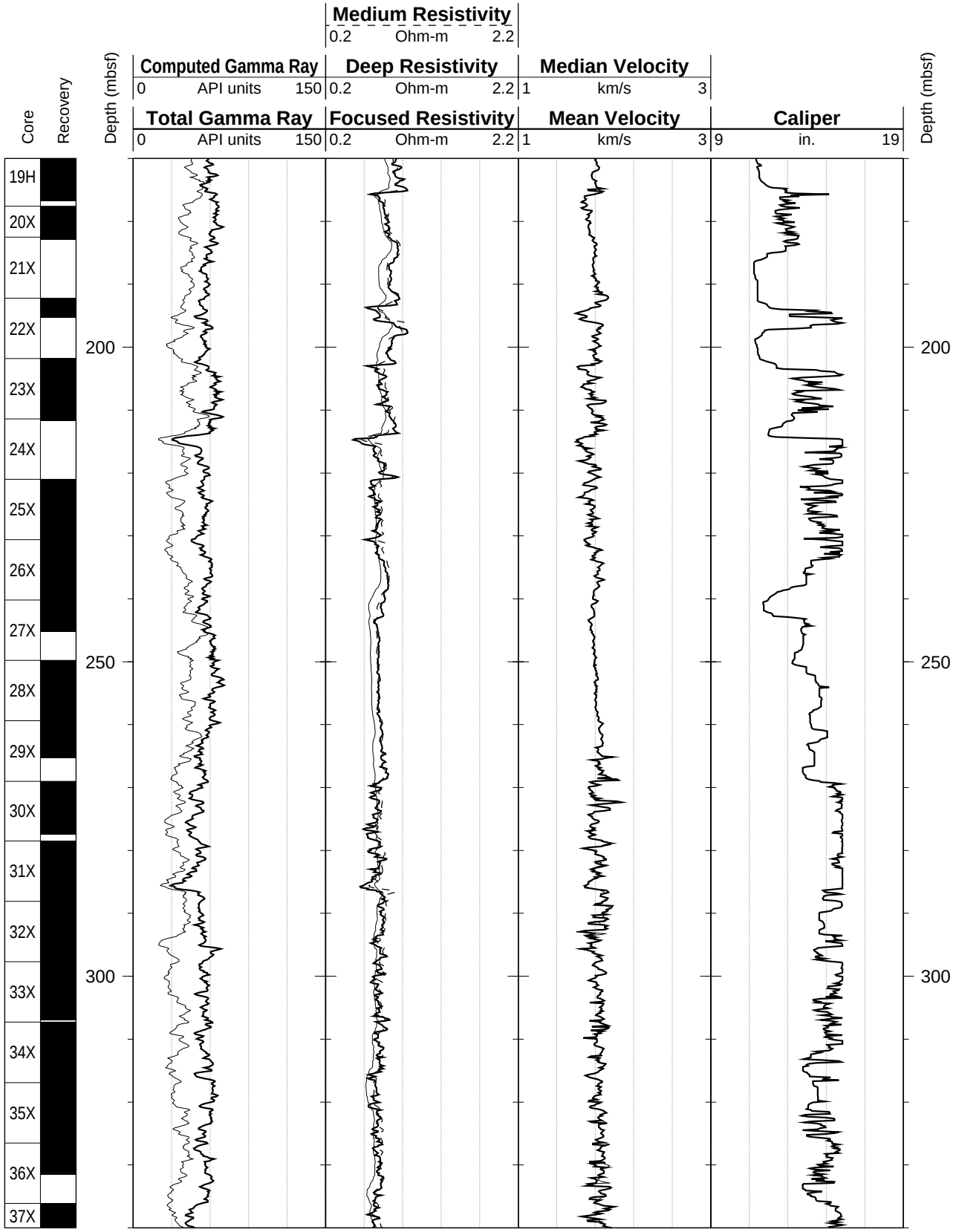

Hole 1037B: Natural Gamma Ray-Resistivity-Sonic Logging Data (cont.)

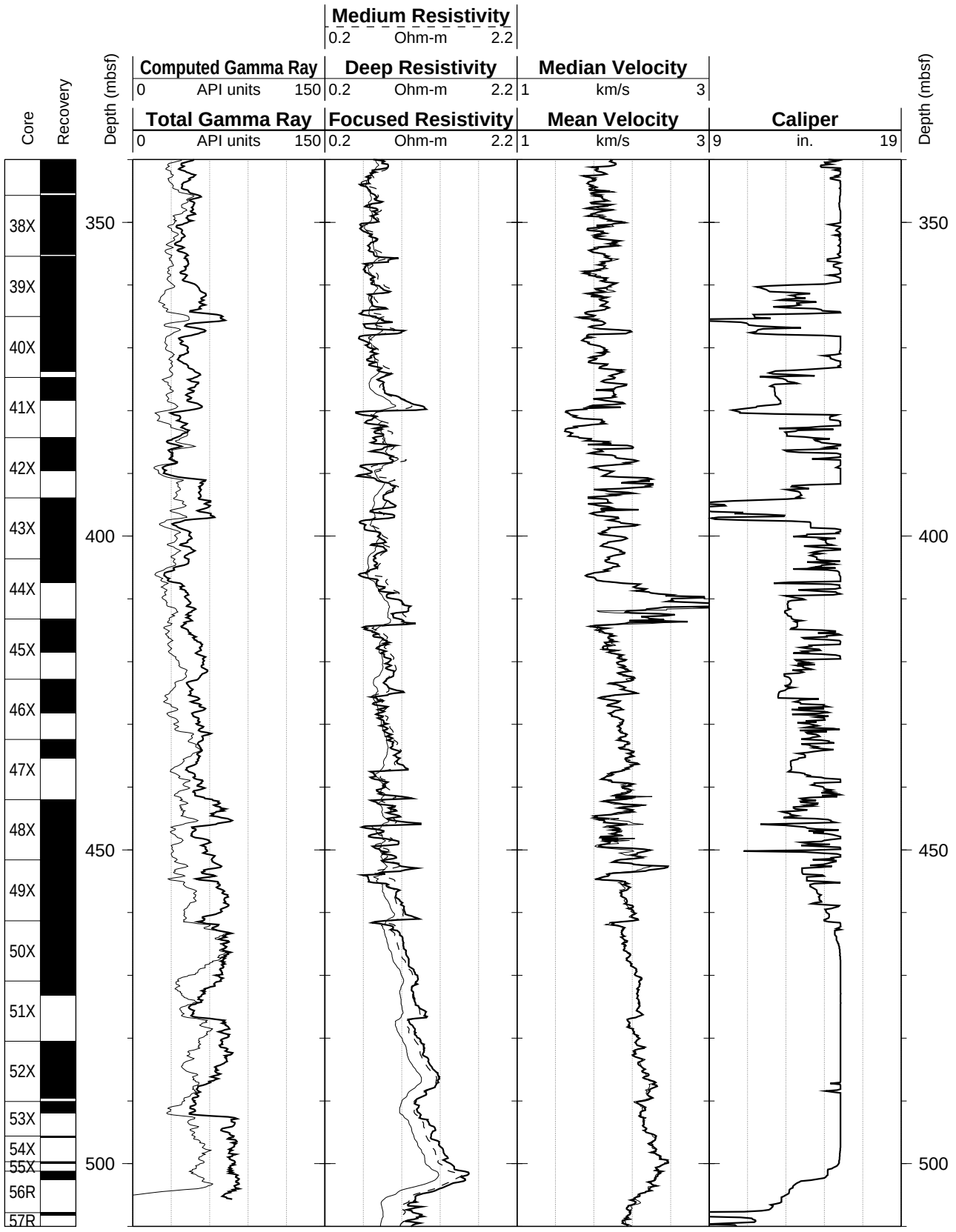

Hole 1037B: Natural Gamma Ray-Resistivity-Sonic Logging Data (cont.)

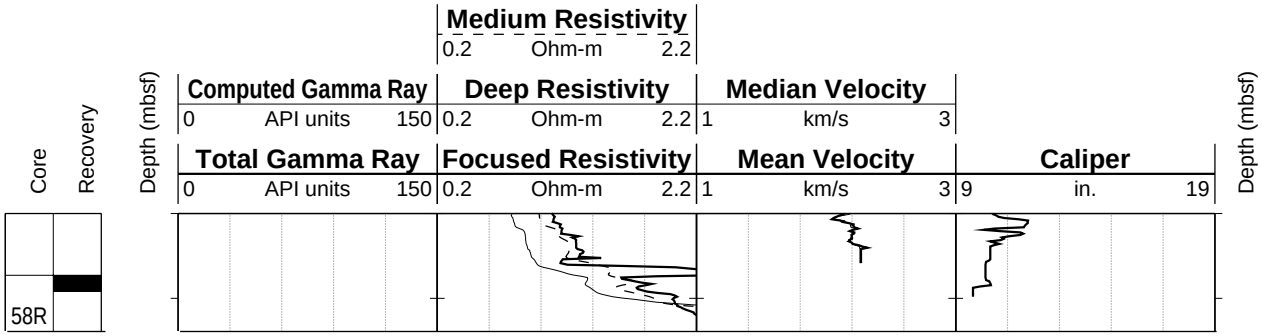

Hole 1037B: Natural Gamma Ray Logging Data

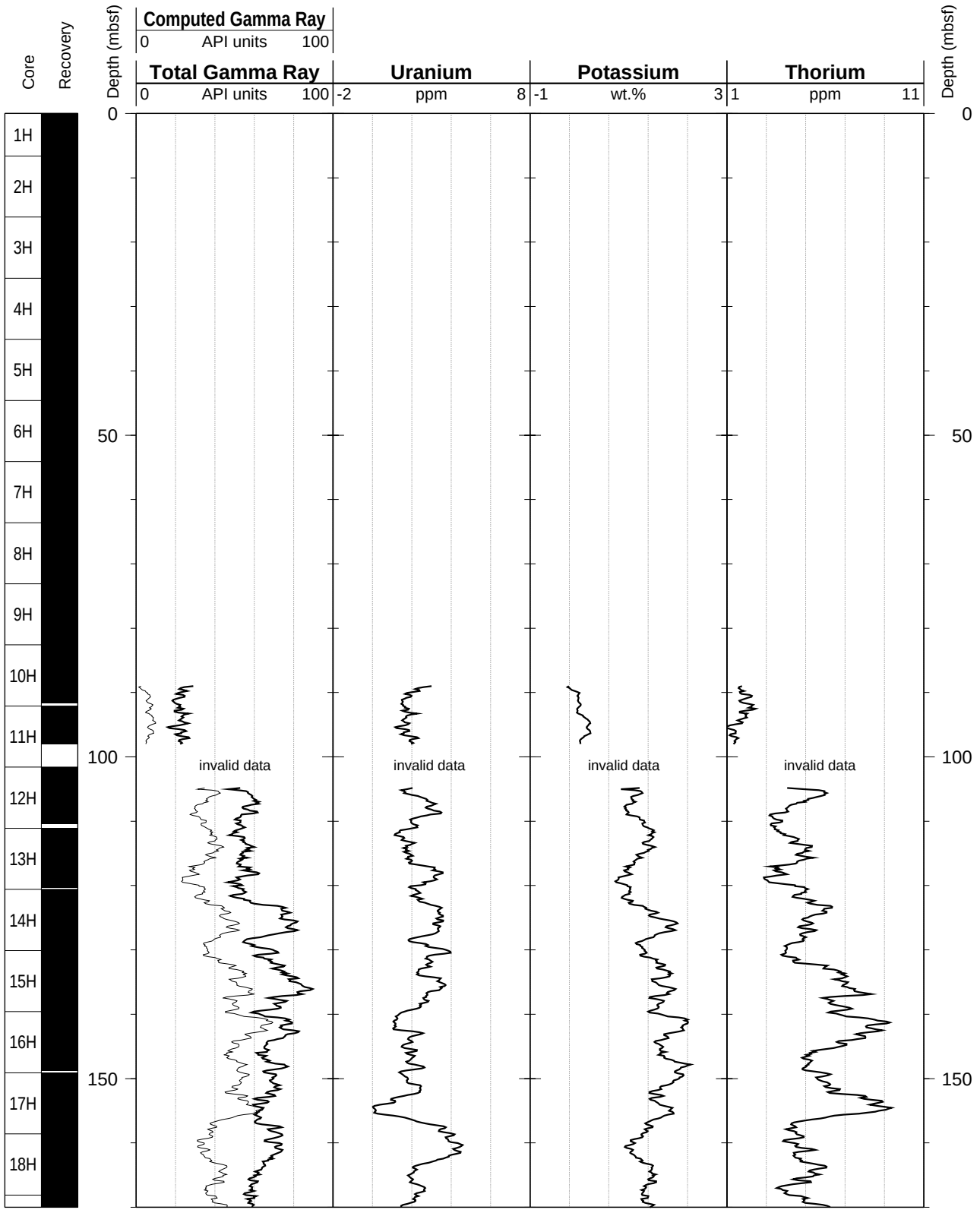

Hole 1037B: Natural Gamma Ray Logging Data (cont.)

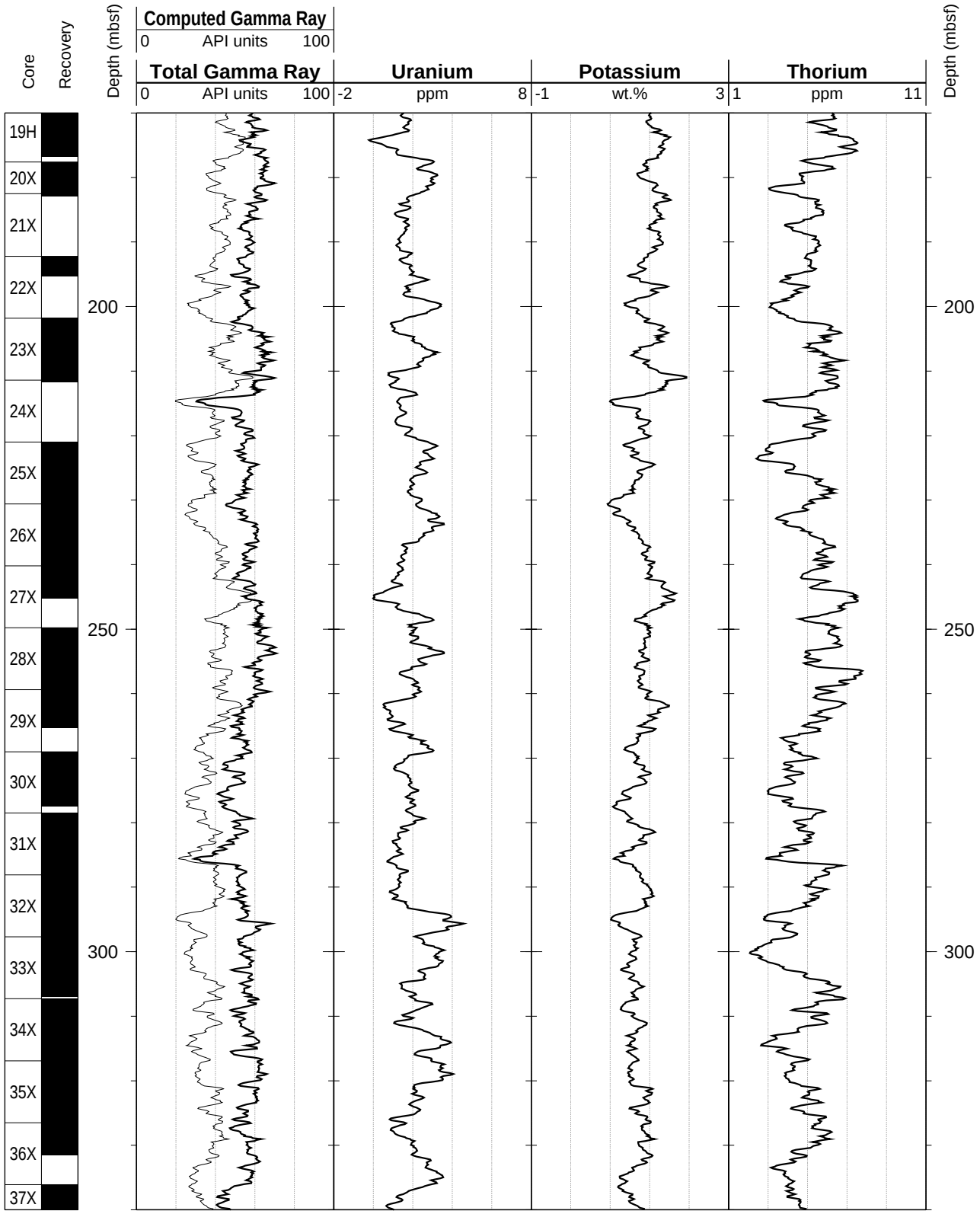

Hole 1037B: Natural Gamma Ray Logging Data (cont.)

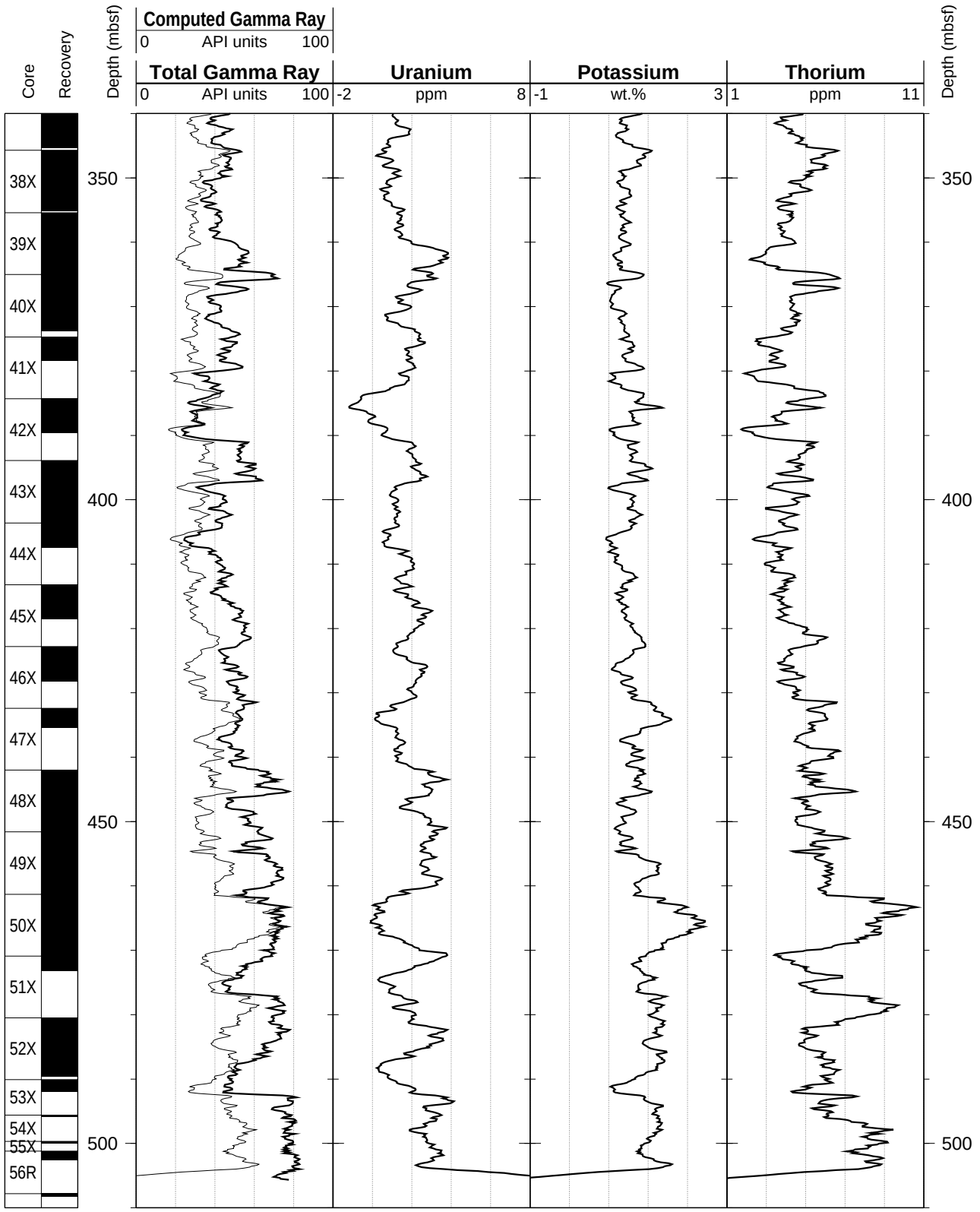

Hole 1037B: Natural Gamma Ray-Density-Porosity Logging Data

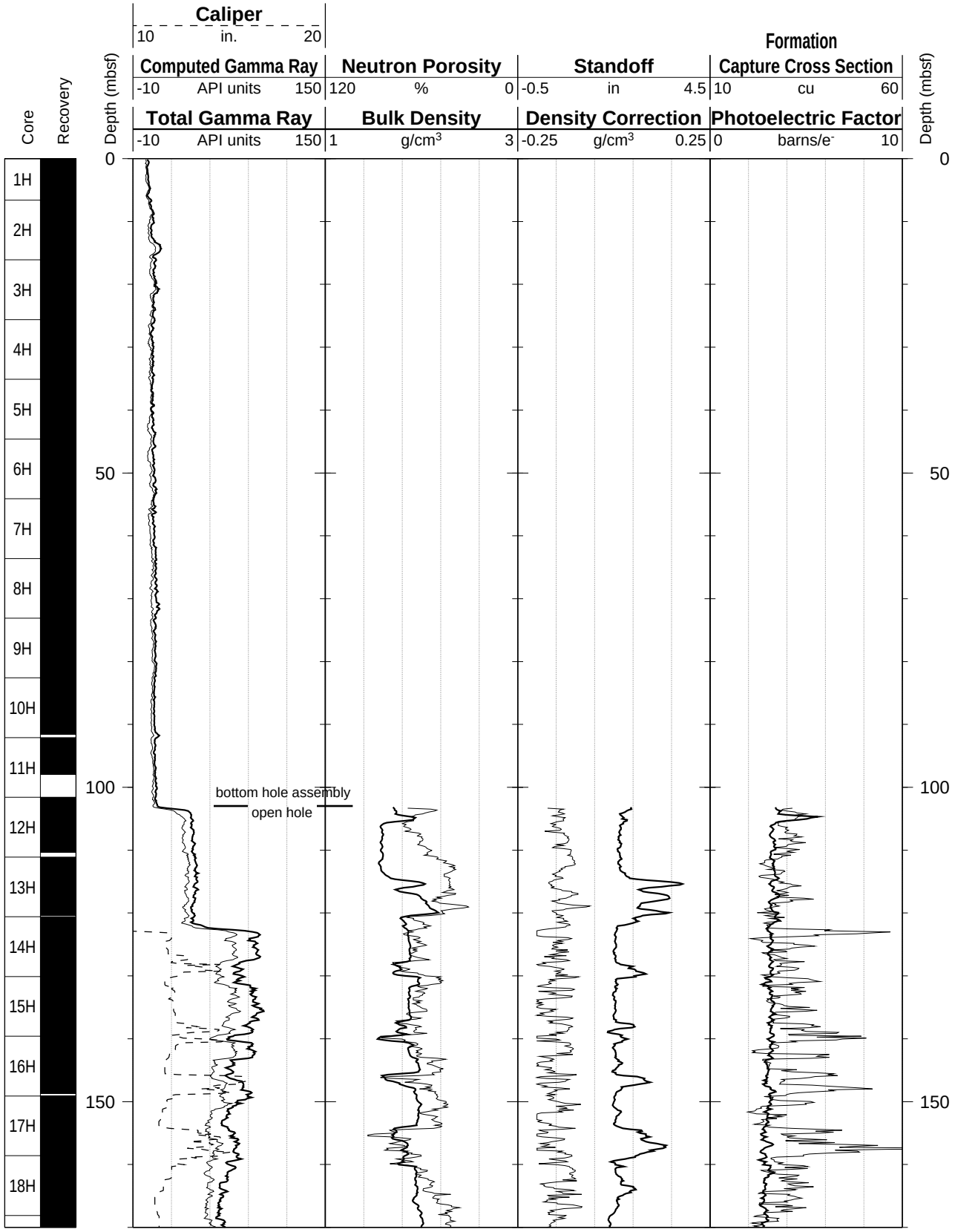

Hole 1037B: Natural Gamma Ray-Density-Porosity Logging Data (cont.)

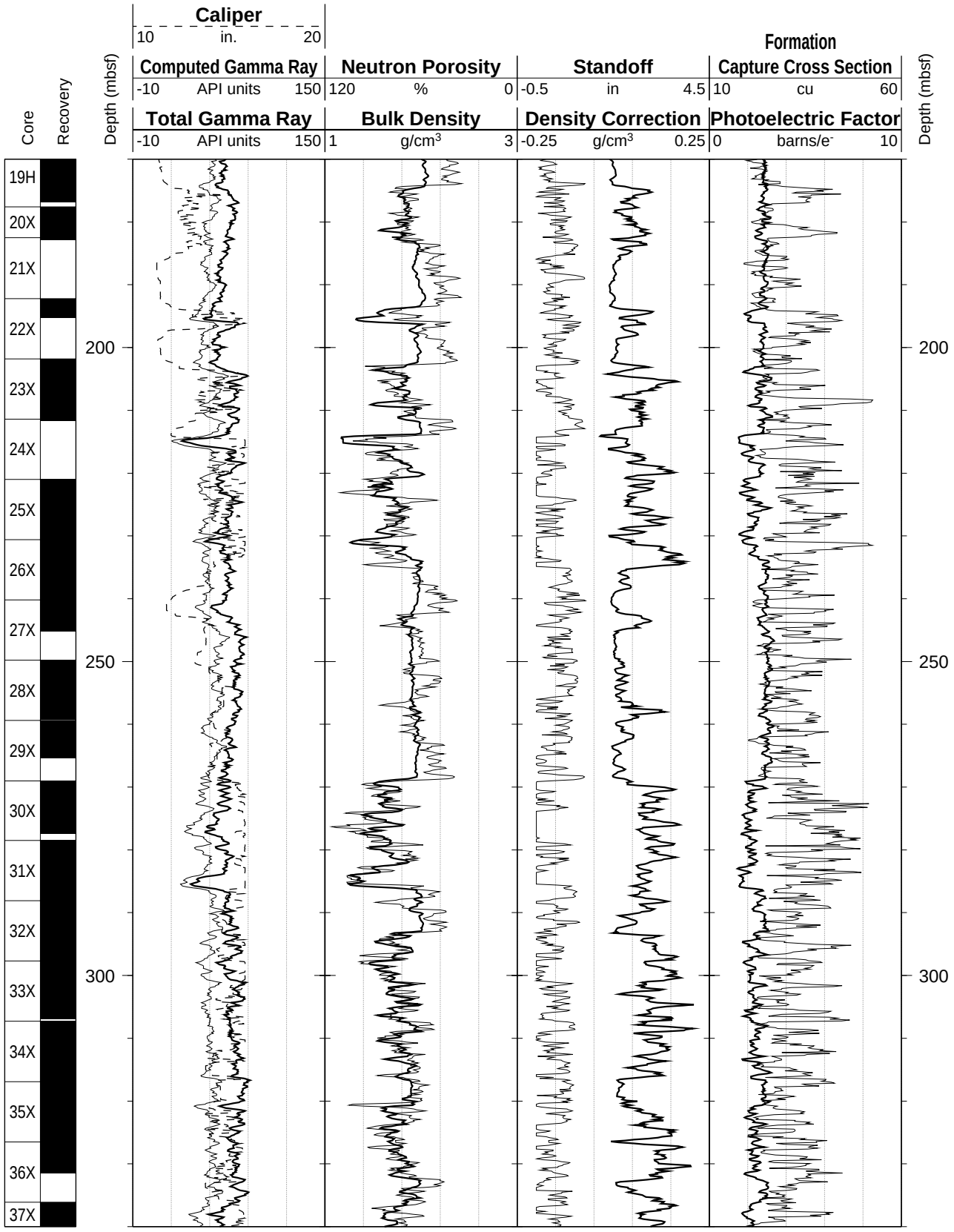

Hole 1037B: Natural Gamma Ray-Density-Porosity Logging Data (cont.)

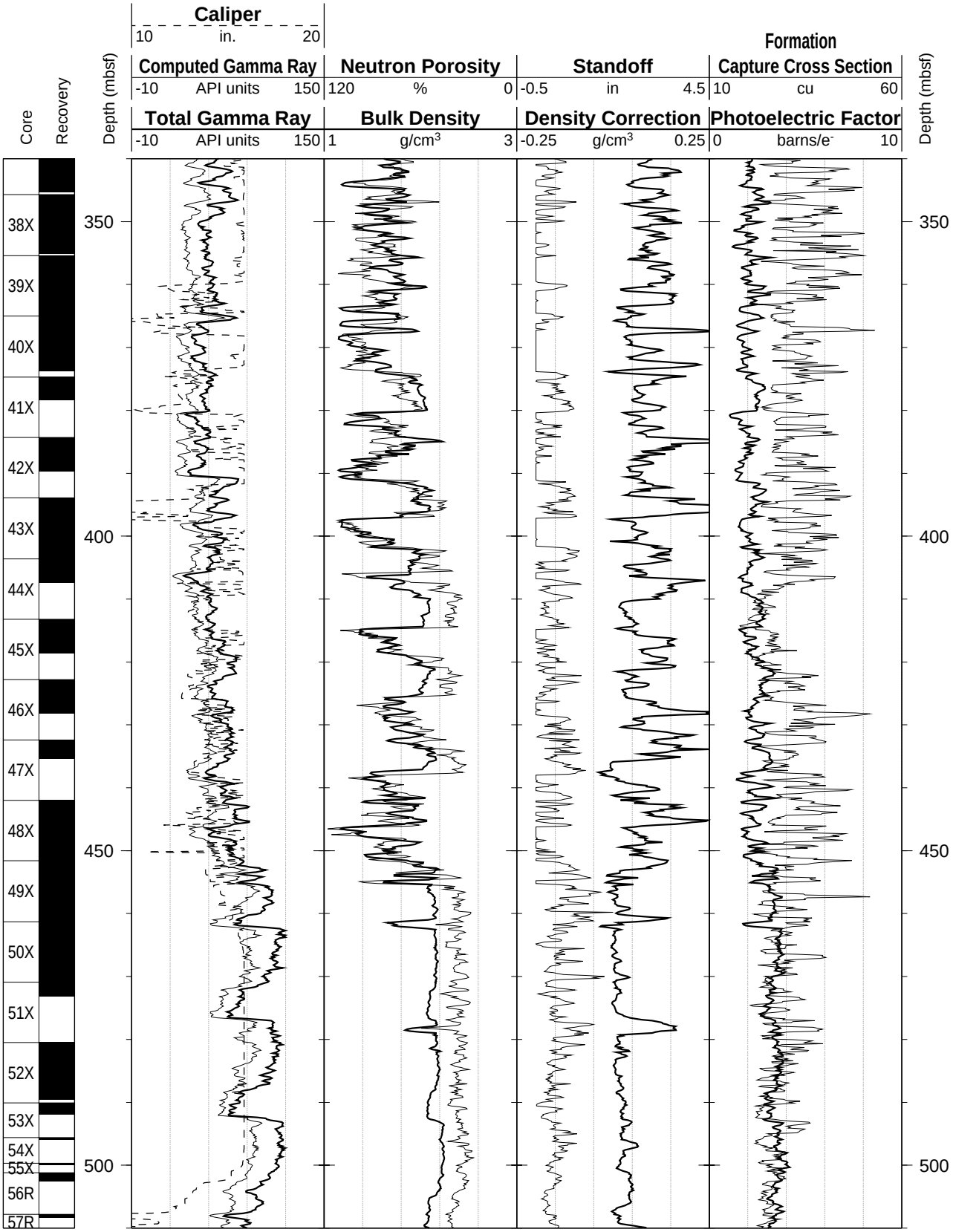

Hole 1037B: Natural Gamma Ray-Density-Porosity Logging Data (cont.)

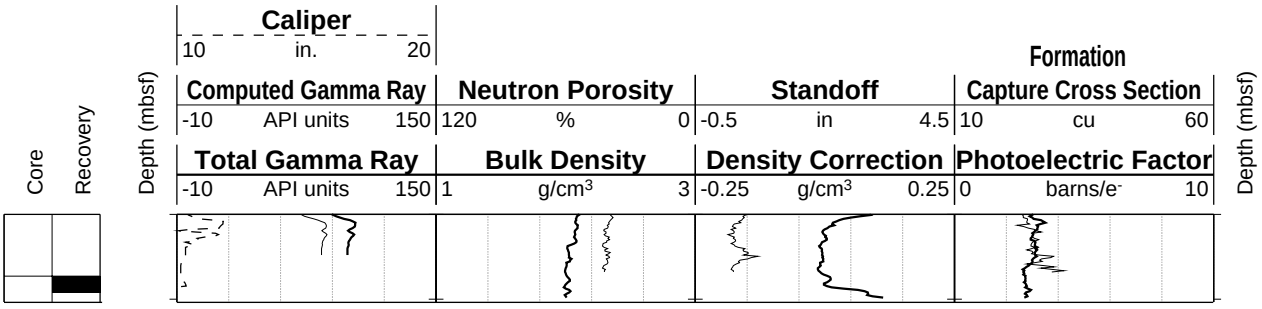

Hole 1037B: Natural Gamma Ray Logging Data

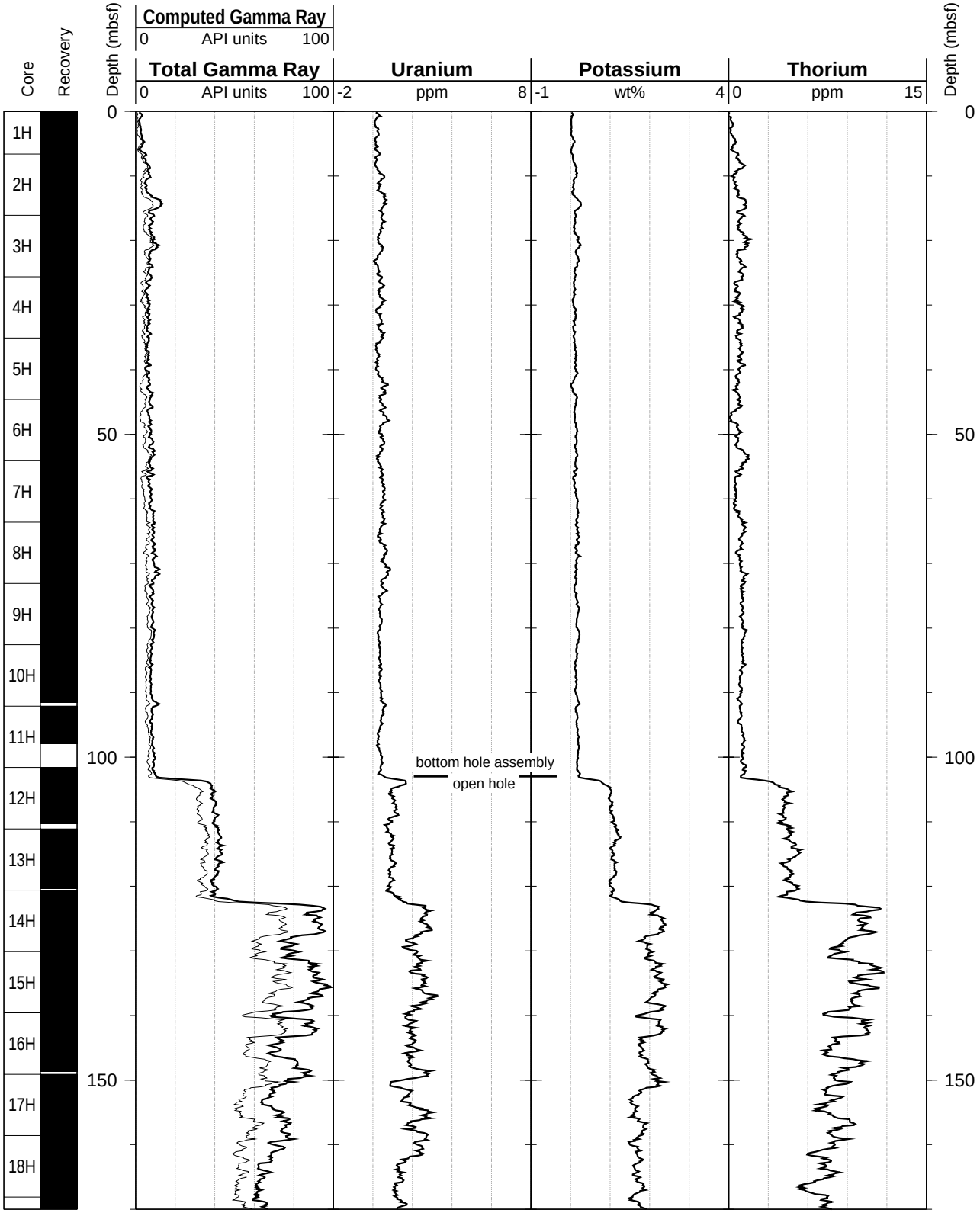

Hole 1037B: Natural Gamma Ray Logging Data (cont.)

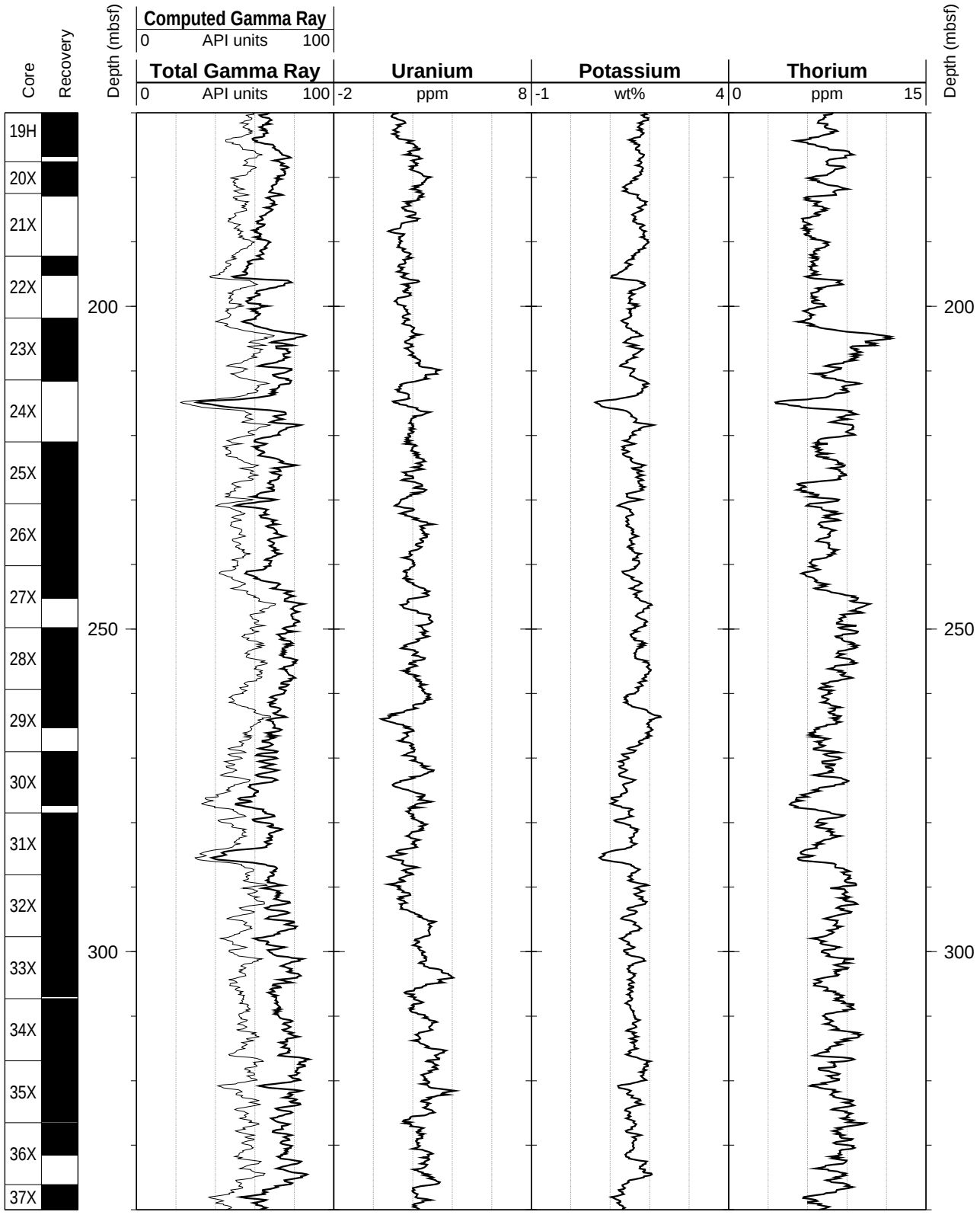

Hole 1037B: Natural Gamma Ray Logging Data (cont.)

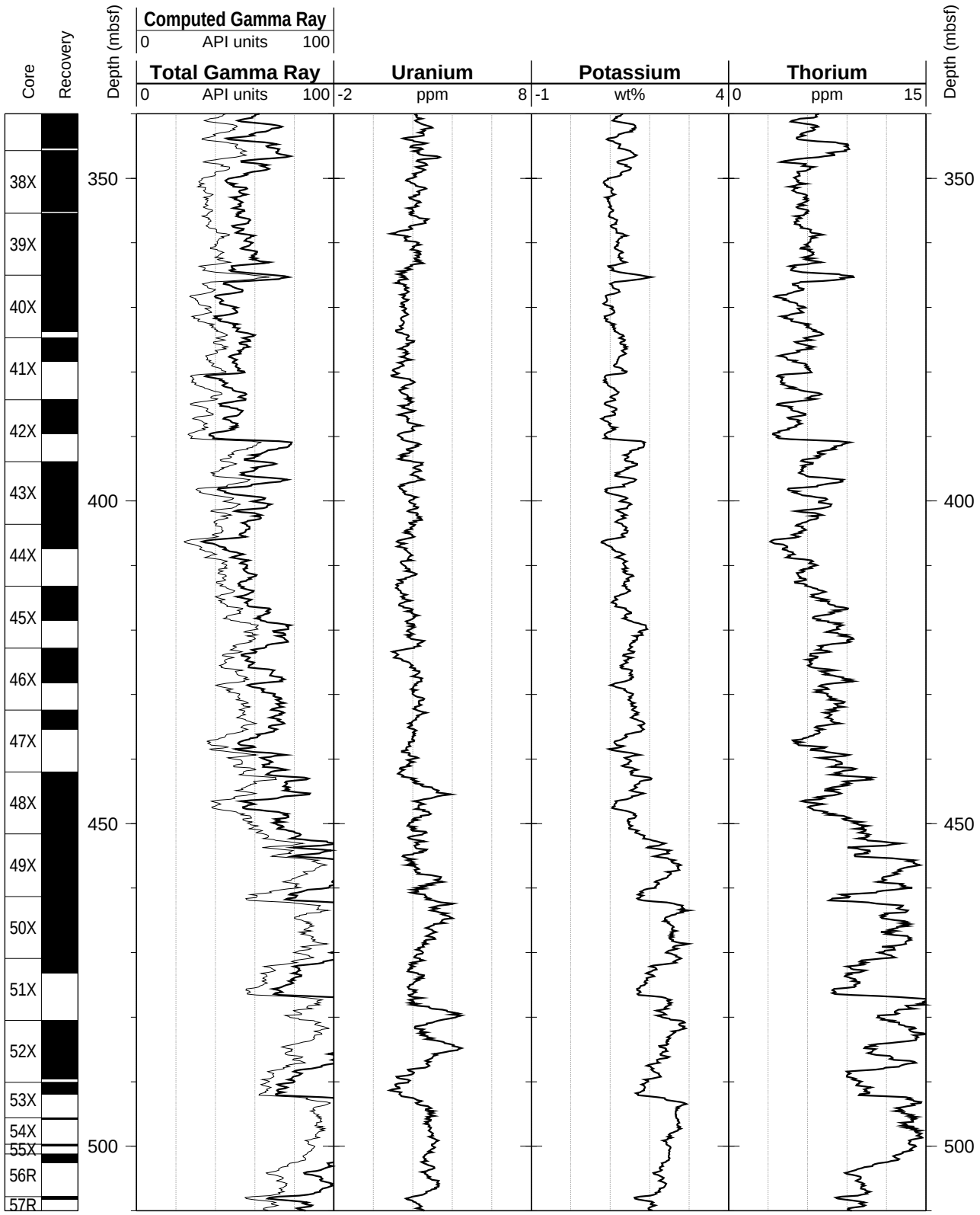

Hole 1037B: Natural Gamma Ray Logging Data (cont.)